REPORT DOCUMENTATION PAGE

Form Approved OMB NO. 0704-0188

1. REPORT DATE (DD-MM-YYYY)	2. REPORT TYPE	3. DATES COVERED (From - To)
16-08-2023	Final Report	1-May-2020 - 15-Aug-2023

4. TITLE AND SUBTITLE
Final Report: Geometry dynamics of compressible turbulence structures

5a. CONTRACT NUMBER
W911NF-20-1-0096

5b. GRANT NUMBER

5c. PROGRAM ELEMENT NUMBER
611102

6. AUTHORS

5d. PROJECT NUMBER

5e. TASK NUMBER

5f. WORK UNIT NUMBER

7. PERFORMING ORGANIZATION NAMES AND ADDRESSES
University of Southern California
University of Southern California
3720 South Flower Street
LOS ANGELES, CA 90089 -0001

8. PERFORMING ORGANIZATION REPORT NUMBER

9. SPONSORING/MONITORING AGENCY NAME(S) AND ADDRESS (ES)
U.S. Army Research Office
P.O. Box 12211
Research Triangle Park, NC 27709-2211

10. SPONSOR/MONITOR'S ACRONYM(S)
ARO

11. SPONSOR/MONITOR'S REPORT NUMBER(S)
75112-WS.4

12. DISTRIBUTION AVAILIBILITY STATEMENT
Approved for public release; distribution is unlimited.

13. SUPPLEMENTARY NOTES
The views, opinions and/or findings contained in this report are those of the author(s) and should not contrued as an official Department of the Army position, policy or decision, unless so designated by other documentation.

14. ABSTRACT

15. SUBJECT TERMS

16. SECURITY CLASSIFICATION OF:			17. LIMITATION OF ABSTRACT	15. NUMBER OF PAGES	19a. NAME OF RESPONSIBLE PERSON
a. REPORT	b. ABSTRACT	c. THIS PAGE			Ivan Bermejo-Moreno
UU	UU	UU	UU		19b. TELEPHONE NUMBER 213-740-2881

RPPR Final Report
as of 16-Aug-2023

Agency Code: 21XD

Proposal Number: 75112WS **Agreement Number: W911NF-20-1-0096**
INVESTIGATOR(S):

Name: Ivan Bermejo-Moreno
Email: bermejom@usc.edu
Phone Number: 2137402881
Principal: Y

Organization: **University of Southern California**
Address: University of Southern California, LOS ANGELES, CA 900890001
Country: USA
DUNS Number: 072933393 EIN: 951642394
Report Date: 31-Aug-2023 Date Received: 16-Aug-2023
Final Report for Period Beginning 01-May-2020 and Ending 15-Aug-2023
Title: Geometry dynamics of compressible turbulence structures
Begin Performance Period: 01-May-2020 **End Performance Period:** 15-Aug-2023
Report Term: 0-Other
Submitted By: Ivan Bermejo-Moreno Email: bermejom@usc.edu
Phone: (213) 740-2881
Distribution Statement: 1-Approved for public release; distribution is unlimited.

STEM Degrees: 1 **STEM Participants:** 3

Major Goals: This research pursues the characterization of the time-evolution of the geometry of finite-sized structures educed from turbulent flows. The objective is to provide a systematic, quantitative description of turbulence dynamics that relates the geometry of structures found at different scales, as evolved by the underlying turbulent flow, with the transported physical quantities on those structures. The analysis focuses on numerical simulation (DNS and LES) datasets of four canonical types of compressible turbulent flows: homogeneous isotropic turbulence (HIT), shear mixing layer, shearless mixing layer, and shock-turbulence interaction (STI). These flow types are chosen as they isolate several key characteristics of turbulence (convective nonlinearities, shear and acoustic-vorticity coupling, anisotropy, and rapid compression/distortion).
We introduce novel analysis methodologies applicable to time series of volumetric field datasets. These methodologies encompass: 1) multi-scale decomposition based on the curvelet transform; 2) structure identification and extraction; 3) characterization of the discrete differential geometry combined with integration of physical quantities conditioned onto area-based probability density functions; 4) unsupervised learning for clustering and classification of common geometric patterns; 5) time-tracking of collections of individual structures through constrained correspondence searches between consecutive time snapshots, 6) encoding structure evolution into graphs that represent the life of each structure and its interactions with others, and, 7) search for common dynamical patterns of ensembles of structures in suitable state spaces that combine geometry and physics. This project focuses on the study of turbulence dynamics from the viewpoint of ensembles of individual structures of finite spatial extent that are temporally evolving and being characterized in physical space. For each flow type we study structures of relevant scalar physical fields derived from the velocity gradient tensor (such as enstrophy, rate of kinetic energy dissipation, and dilatation), The developed methodologies also allow the analysis of the interplay between ensembles of structures with common geometries and dynamical patterns educed from different fields and scales. These analyses are intended to answer fundamental questions in turbulence research, such as: are vortex tubes in the inertial range generated by the roll-up of surrounding sheets of dissipation? Does the the signature cascade of kinetic energy present in Fourier space (scale) have a counterpart in physical space (turbulent eddy size), as hypothesized by Richardson? The time-evolution analysis
of collections of structures with common geometries can then elucidate the mechanisms enabling such cascade dynamics in physical space and link with established Fourier-based statistical theories to justify of models of turbulence fine scales.

The major goals of the project are associated with the following milestones, split between methods and application:

Methodology development and implementation
- Time-tracking and graph construction.

- Integrated flow physics and geometry.
- Graph query and state-space trajectory.
- Pattern mining (graph and trajectory).
- Dynamic interplay of proximal structures.

Application to datasets obtained from direct numerical simulation (DNS) and large-eddy simulation (LES):

- Homogeneous Isotropic Turbulence, HIT
- Shock Turbulence Interaction, STI
- Turbulent Shear Mixing Layer
- Turbulent Shearless Mixing Layer

Accomplishments: Please refer to the uploaded PDF document.

Training Opportunities: During this project, opportunities for training and professional development have focused on:

- one-on-one academic mentoring was provided by the project PI to the two main graduate research assistants (GRAs), Jonas Buchmeier and Naili Xu, funded by this project towards the completion of their doctoral degree. Jonas Buchmeier successfully defended his doctoral thesis in the Spring 2022 semester, graduating from USC in May 2022. Naili Xu is expected to graduate in 2024.

Dr. Jonas Buchmeier's thesis is titled:

+ Buchmeier, J. ``Tracking and evolution of compressible turbulent flow structures," Ph.D. Thesis, University of Southern California.

- in summer 2023, Johannes Reichert, a M.Sc. in the AME department at USC was hired as part-time (28h/week) a student worker for 9 weeks, and was provided with training opportunities in the analysis of CFD datasets within this project.

- high-performance computing training to the GRAs funded by this project, Jonas Buchmeier and Naili Xu, PhD students in the Aerospace and Mechanical Engineering Department at the University of Southern California, in the research group of the PI. Naili applied and was selected to attend the Argonne Training Program for Extreme Scale Computing (ATPESC) organized yearly by the Argonne Leadership Computing Facilities at Argonne National Laboratories. Naili attended the ATPESC program in the summer of 2022, along with another member of the PI's research group. In past years,
three other members of the PI's research group have been selected and attended previous editions of the prestigious training program, including former PhD student funded by this project, Dr. Jonas Buchmeier.

- After graduating from USC with a PhD, Dr. Jonas Buchmeier conducted postdoctoral research in the PI's group for six months, and then started a research position at DLR (German Aerospace Center) in Cologne, Germany.

Additional training opportunities attending and presenting at scientific meetings of the American Physical Society (Division of Fluid Mechanics) were provided to the GRAs during the course of this project, as detailed in the major activities section of the uploaded PDF document of this final report.

RPPR Final Report
as of 16-Aug-2023

Results Dissemination: In the course of this project, the following articles was published in the Physics of Fluids peer-reviewed journal:
+ J. Buchmeier, A. Bussmann, X. Gao, I. Bermejo-Moreno (2021) "Geometry and dynamics of passive scalar structures in compressible turbulent mixing" Physics of Fluids 33 (105126). https://doi.org/10.1063/5.0068010
The article was selected as an Editor's Pick by the Physics of Fluids journal. The article has as leading author the GRA funded by this project as main author, the PI as co-author, along with a recently graduated doctoral student in the PI's group, and a (formerly) M.Sc. student from Technical University Munich who spent six months in the PI's research group, becoming a collaborator in the development of the tracking methodologies.

+ A. Bussmann, J. Buchmeier, M. S. Dodd, S. Adami, Bermejo-Moreno, I. (2022) "Tracking and analysis of interfaces and flow structures in multiphase flows," Computers & Fluids, 105665. https://doi.org/10.1016/j.compfluid.2022.105665 This article includes research performed both during and prior to this project by one of the funded GRAs (Jonas Buchmeier) and a visiting scholar from Technical University Munich (Alexander Bussmann), who completed a six-month stay in the PI's lab. The research work is based on the same methodologies for turbulent structures geometric characterization and time tracking employed in the funded effort. The scope of application is in multiphase flows (drop breakup in homogeneous isotropic turbulence), departing from the compressible regime that was emphasized in the major goals of the project. However, it shows the generality of application and usability of the developed methodologies to study a wide range of flow physics in different regimes.

- Dissemination of scientific results was also accomplished through the participation in different scientific conferences, including the American Physical Society - Division of Fluid Dynamics meeting and the Southern California Flow Physics Symposium, by GRA Jonas Buchmeier and the PI:
+ Buchmeier, J., Bussmann, A., Gao, X. & \textbf{Bermejo-Moreno, I. "Temporal evolution of flow features in isotropic turbulence and shock-turbulence interaction" 73rd Annual Meeting of the APS Division of Fluid Dynamics, Chicago, Illinois, November 2020.
+ Buchmeier, J. & Bermejo-Moreno, I. "Evolution of passive scalar structures in compressible turbulent mixing" 14th Southern California Flow Physics Symposium (SoCal Fluids XIV), California Institute of Technology, Pasadena, California, April 2021 (virtual).
+ Buchmeier, J., Bussmann, A., Gao, X. & \textbf{Bermejo-Moreno, I. "Dynamics of vortical structures in compressible mixing layers through tracking and graph-based geometrical analyses," 73rd Annual Meeting of the APS Division of Fluid Dynamics, Phoenix, Arizona, November 2021.
+ Buchmeier, J. Bermejo-Moreno, I "Evolution of vortical structures in compressible mixing layers" 15th Southern California Flow Physics Symposium (SoCal Fluids XIII), University of California, Los Angeles, California, April 2022.

In addition to the conference presentation at the APS-DFD meetings given by the GRA, the PI also presented ongoing results from this project at the following invited seminars:
+ "Numerical Investigation of Shock-Induced Phenomena in Turbulent Flows." (virtual) Australasian Fluid Mechanics Seminar Series, October 2020.
+ "Shock-induced phenomena in turbulent flows through numerical simulation and diagnostics." (virtual) CTR Tea Seminar, Center for Turbulence Research, Stanford University, September 2020.
+ "Simulation and analysis of turbulent flows with shock waves over rigid and elastic walls." Computational Science Division (CPS) Seminar, Argonne Leadership Computing Facility (ALCF), Argonne National Laboratory (virtual), April 2022.
+ "Numerical simulations of oblique shocks impinging on turbulent boundary layers developed over flexible walls," San Diego State University, Department of Aerospace Engineering, September 2022.
+ "Interactions of shock waves and turbulence through numerical simulations," University of Southern California, Department of Aerospace and Mechanical Engineering, April 2023.
+ "Interactions of shock waves and turbulence through numerical simulations," GALCIT Colloquim, California Institute of Technology, Graduate Aerospace Laboratories, May 2023.

Honors and Awards: During theThe PI received the following awards:
- NSF CAREER Award (2022)
- NASA Early Career Faculty Award 2023 (selected for award)

Protocol Activity Status:

Technology Transfer: Nothing to Report

RPPR Final Report
as of 16-Aug-2023

PARTICIPANTS:

Participant Type: PD/PI
Participant: Ivan Bermejo-Moreno
Person Months Worked: 3.00 **Funding Support:**
Project Contribution:
National Academy Member: N

Participant Type: Graduate Student (research assistant)
Participant: Jonas Buchmeier
Person Months Worked: 15.00 **Funding Support:**
Project Contribution:
National Academy Member: N

Participant Type: Graduate Student (research assistant)
Participant: Naili Xu
Person Months Worked: 15.00 **Funding Support:**
Project Contribution:
National Academy Member: N

Participant Type: Graduate Student (research assistant)
Participant: Johannes Reichter
Person Months Worked: 2.00 **Funding Support:**
Project Contribution:
National Academy Member: N

ARTICLES:

RPPR Final Report
as of 16-Aug-2023

Publication Type: Journal Article Peer Reviewed: Y **Publication Status:** 1-Published
Journal: Physics of Fluids
Publication Identifier Type: DOI Publication Identifier: 10.1063/5.0068010
Volume: 33 Issue: First Page #: 105126
Date Submitted: 11/2/21 12:00AM Date Published: 10/27/21 7:00AM
Publication Location:
Article Title: Geometry and dynamics of passive scalar structures in compressible turbulent mixing
Authors: Jonas Buchmeier, Alexander Bussmann, Xiangyu Gao, Ivan Bermejo-Moreno
Keywords: compressible shock-induced turbulent mixing tracking geometry
Abstract: We present a structure-based numerical analysis of passive scalar mixing in decaying homogeneous isotropic turbulence (DHIT) and shock-turbulence interaction canonical configurations. The analysis focuses on the temporal evolution of ensembles of passive scalar structures, initialized as spheres of different sizes relative to the Taylor microscale. An algorithm is introduced to track the evolution of each individual structure and the interactions with other structures in the ensemble, relating changes in the surface geometry and the underlying physical processes (turbulent transport, scalar dissipation, and shock compression). The tracking algorithm is applied to datasets from shock-capturing direct numerical simulations of DHIT, with Taylor microscale Reynolds number Re?=40 and turbulence Mach number Mt=0.2, and STI cases in which the turbulence is processed by a shock wave at Mach numbers M?=?1.5 and 3.0. Temporal surface convolution increases for initially larger structures, resulti
Distribution Statement: 2-Distribution Limited to U.S. Government agencies only; report contains proprietary info
Acknowledged Federal Support: **Y**

Publication Type: Journal Article Peer Reviewed: Y **Publication Status:** 1-Published
Journal: Computers & Fluids
Publication Identifier Type: DOI Publication Identifier: 10.1016/j.compfluid.2022.105665
Volume: 248 Issue: First Page #: 105665
Date Submitted: 8/16/23 12:00AM Date Published: 11/1/22 7:00AM
Publication Location:
Article Title: Tracking and analysis of interfaces and flow structures in multiphase flows
Authors: A. Bußmann, J. Buchmeier, M.S. Dodd, S. Adami, I. Bermejo-Moreno
Keywords: Tracking Multiphase Droplet breakup Homogeneous isotropic turbulence
Abstract: A methodology is introduced to study the dynamics of fluid interfaces in multiphase flows, emphasizing their break-up and coalescence. The algorithm tracks surfaces, here obtained by isocontouring an interface-describing scalar field (e.g., VOF) from a time series of volumetric snapshots. Physical and geometric information of the surfaces is used to find correspondences in a higher-dimensional space. Events are derived from found correspondences to describe the interactions among isosurfaces of closed fluid structures extracted at consecutive tracking time steps. The correspondences and events are filtered based on physical realizability, accounting for geometric constraints between consecutive time instances, as well as temporal constraints on the relations between surfaces in previous tracking steps. The resulting events are used to map the time evolution of all surfaces and their interactions into a graph, which is then queried to retrieve information on the dynamics of the fluid i
Distribution Statement: 1-Approved for public release; distribution is unlimited.
Acknowledged Federal Support: **Y**

DISSERTATIONS:

Publication Type: Thesis or Dissertation
Institution: University of Southern California
Date Received: 16-Aug-2023 Completion Date: 1/23/22 6:05AM
Title: Tracking and evolution of compressible turbulent flow structures
Authors: Jonas Buchmeier
Acknowledged Federal Support: **Y**

RPPR Final Report
as of 16-Aug-2023

Partners

,

I certify that the information in the report is complete and accurate:
Signature: Ivan Bermejo-Moreno
Signature Date: 8/16/23 1:09AM

Final report for contract W911NF2010096 - Accomplishments

Ivan Bermejo-Moreno

Dates Covered: May 01, 202 to August 15, 2023

Abstract

The goal of this research is to characterize the dynamics of turbulence from a geometric standpoint by novel analyses of the time evolution of ensembles of turbulent flow structures educed from high-fidelity numerical simulations of compressible flows, linking geometry and physics mapped at the structural level, focusing on the effects of shear, anisotropy, inhomogeneity, and flow compressibility in the geometric evolution of turbulence structures. Our methodology works at the structure level in physical space, with each structure defined as an individual entity with finite spatial extent. No a priori assumptions are made on the existence and relevance of coherent and incoherent turbulence structures. The characterization of the geometry of a structure is independent of the field from which the structure was educed; this differs from existing methods that classify points as belonging to one type of geometry or another, based on assumed relations to the physical field from which the structures are educed. The developed methods are applied to canonical compressible flows such as homogeneous isotropic turbulence, shock-turbulence interaction, mixing layers.

Contents

1 Major activities and technical accomplishments

The accomplishments in the project have a direct mapping to the major goals established in the proposal, which incorporate first the development and implementation of methodologies regarding the following aspects of the temporal evolution of turbulent structures:

1. Time-tracking and graph construction (Y1).
2. Integrated flow physics and geometry (Y1).
3. Graph querying and state-space trajectory (Y2).
4. Pattern mining (graph and trajectory) (Y3).
5. Dynamic interplay of proximal structures (Y3).

Secondly, these major methodological goals are demonstrated through the application to several numerical datasets obtained by direct numerical simulation (DNS) of turbulent flows, including homogeneous isotropic turbulence (HIT), shock turbulence interaction (STI), and compressible turbulent mixing layers (CML). The first half of the project (Y1-Y2) was devoted to HIT and STI applications, whereas the last part of the project emphasized CML (Y2-Y3). Additionally, research work on the application of structural tracking methodologies to multi-phase turbulent flows conducted prior to the start of the project was finalized and published within this project, since a subset of the same methodologies developed by the PI's group are shared across all these applications.

All the numerical simulations were performed with solvers developed in-house and on our local computer clusters at USC. The methods developed in this project are applicable to any kind of flow features defined as closed surfaces embedded in a three-dimensional space. The surfaces could be derived from a numerical simulation (as in the present project), or originate from experimental data. Within this study, the surfaces (structures) are extracted by isosurfacing volumetric fields obtained from direct numerical simulations (e.g., passive scalar, Q-criterion, etc.). However, flow feature extraction methods are extrinsic to the analysis methodologies introduced in this work and are not of the subject of this report. The tracking and analyses algorithms introduced here are applicable regardless of the extraction method applied.

During the course of the project, the analysis of compressible turbulent mixing layers done in the last year and a half led to establishing an additional goal that focused on the study of hairpin vortices, found in the development of the self-similar regime. Hairpin-like vortical structures have been previously found to be predominant structural features of wall-bounded turbulent flows (in all regimes). Developing robust detection/identification methods for such structures is of importance to the field. Given the presence of these hairpin vortices in the produced numerical datasets, we emphasized their study over testing application of the tracking methodology to any additional flow type. The method of hairpin vortex identification and its application to the numerical databases obtained in this project thus represent an addition to the original project goals, and will be described later in this report (§4.2-4.5).

The methods and findings of this research have been published in peer-reviewed journal articles and presented in scientific conferences and invited seminars, as listed in the 'Dissemination' online section of this final report. An additional manuscript is currently being written and will be

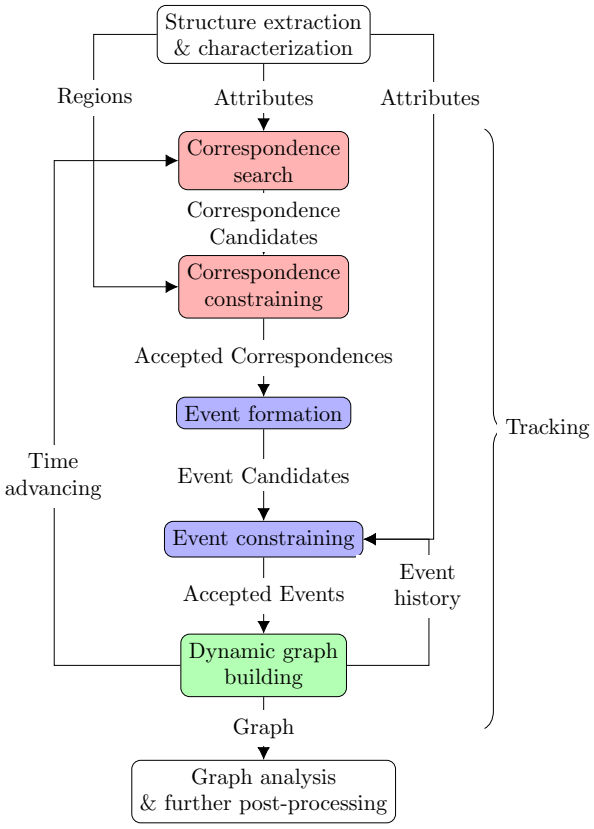

Figure 1: Tracking workflow: correspondence search & constraining (red), event formation & constraining (blue), and dynamic graph building (green).

submitted for publication of the results on compressible turbulent mixing layers obtained from the research performed in the last part of the project. The main findings of this work are also described in this report.

2 Flow feature tracking methodology

To analyze the dynamics and evolving characteristics of flow features (e.g., passive scalar isosurfaces) in physical space, we have developed and implemented a novel local, hybrid attribute- and region-based, explicit tracking methodology (fig. 1). Local methods assume a limited motion of features between consecutive frames, in contrast to global methods [1, 2, 3]. Explicit tracking requires the independent extraction of flow features from a series of time instants (frames), followed by the matching of extracted features for each pair of consecutive frames (solving the *correspondence problem*). Region-based algorithms rely on the spatial overlap of features in consecutive frames, requiring a fairly high sampling frequency for datasets that contain small, fast-moving features [4, 5, 6, 7]. Instead, attribute-based algorithms solve the correspondence problem using a set of abstract attributes to describe the features [8, 9, 10, 11]. Our proposed hybrid method does not impose any requirement of spatial overlap of corresponding structures between frames and is therefore less restrictive in terms of the sampling frequency, by combining the spatial location and non-local geometric attributes of flow features, and introducing a set of physically realizable constraints.

In the matching process, flow structures in consecutive time frames t_n and t_{n+1} will be referred to as 'source' and 'target' structures, respectively. Interactions of source and target structures within a sampling interval are described by the following types of events [8]: In a 'creation' event, a new structure appears in the target frame. In a 'continuation' event, a structure continues from one frame to the next without interacting with another structure. In a 'split' event, a source structure breaks into two or more target structures. In a 'merge' event, two or more source structures coalesce into one target structure. In a 'disappearance' event, a source structure vanishes. The complexity of events can depend on the sampling interval. For example, as the sample interval increases, a sequence of two first-order splits would eventually be detected as a single second-order split. Large sampling intervals create a need to additionally consider 'compound' events, in which multiple source structures merge and split into multiple target structures [12].

The attributes used to find correspondences include the dimensionless center of the oriented bounding box (OBB) $\{x_c, y_c, z_c\}$ of a structure, and three dimensionless geometric attributes: the global compactness parameter $\hat{\lambda}$, the feature shape index $\hat{S}$ and curvedness $\hat{C}$. The compactness is defined in terms of the structure volume V and area A by:

$$\hat{\lambda} = \sqrt[3]{36\pi}\frac{V^{2/3}}{A} \in [0,1]. \tag{1}$$

where the normalization factor is chosen such that $\hat{\lambda} = 1$ for spheres. The non-local quantities $\hat{S}$ and $\hat{C}$ are obtained from first- and second-order moments of the area-based joint probability density function of two pointwise differential geometry properties[13]: the absolute value of the shape index, S, and the dimensionless curvedness, C, defined in terms of the principal curvatures $\{\kappa_1, \kappa_2\}$ as[14]

$$S = \left| -\frac{2}{\pi} \arctan \frac{\kappa_1 + \kappa_2}{\kappa_1 - \kappa_2} \right|, \qquad C = 3\frac{V}{A}\sqrt{\frac{\kappa_1^2 + \kappa_2^2}{2}}. \tag{2}$$

Larger curvedness implies a shorter radius of curvature and, hence, a more curved surface. The shape index classifies surface points as hyperbolic $S < 0.5$, parabolic $S = 0.5$, or (concave or convex) elliptical $0.5 < S < 1$. $S = 0$ and $S = 1$ correspond to symmetrical saddle and umbilical points, respectively. $S \in [0,1]$ is undefined for a locally planar surface, for which $C = 0$ (note $C \in \mathbb{R}^+$). Regions of the space of geometric attributes $\{\hat{S}, \hat{C}, \hat{\lambda}\}$ are associated with particular surface shapes: blob-like structures concentrate near the $(\hat{S}, \hat{C}, \hat{\lambda}) = (1,1,1)$ point, tube-like structures are near the axis $(1/2, 1, \hat{\lambda})$, and sheet-like structures arise for lower values of $\hat{C}$ and $\hat{\lambda}$.

Hence, in our characterization method, each structure is represented as a point in a six-dimensional attribute space $\{x_c, y_c, z_c; \hat{S}, \hat{C}, \hat{\lambda}\}$ that combines spatial and geometric shape attributes. The spatial attributes are nondimensionalized with the domain size in each direction. All structures in a frame form a cloud of points in this attribute space. The proposed tracking method, however, is applicable to any other choice of feature attributes.

2.1 Detection of correspondence candidates

A search for correspondences between each pair of source and target point clouds is conducted utilizing first the full set of attributes and, second, only its spatial subset, $\mathbf{x} = \{x_c, y_c, z_c\}$. The search for correspondences is performed in multiple stages in which both the source and the target clouds participate as query and searched clouds. An estimate $\mathbf{x}'$ of the spatial attributes in the searched cloud is obtained by a linear projection based on the surface-averaged velocity, $\mathrm{v}_{\mathrm{avg}}$, and the tracking step Δt:

$$\mathbf{x}' = \mathbf{x} \pm \Delta t \mathbf{v}_{\mathrm{avg}}, \qquad \mathbf{v}_{\mathrm{avg}} = \frac{1}{A}\int_A \mathbf{v} \mathrm{d}A. \tag{3}$$

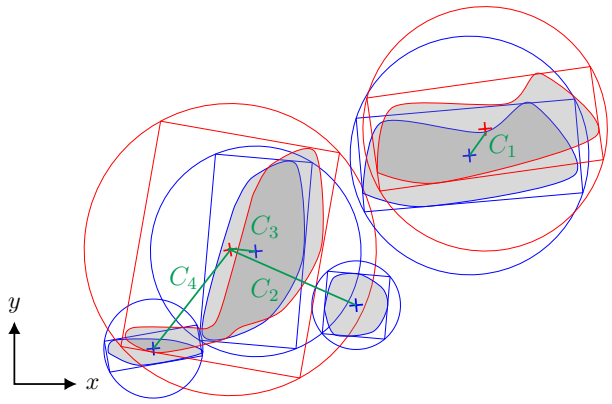

Figure 2: Illustration of a continuation, first-order merge and disappearance event of generic shapes (shown in 2D, for clarity). OBB of source (target) structures in blue (red). Search radius based on OBB half-diagonal without tolerance. Events detected by the radius search are a true continuation $\{C_1\}$ and a false second order merge $\{C_2, C_3, C_4\}$, which emphasizes the need for a constraining process based physical realizability to reject $\{C_2\}$ in this example.

The projection is performed forward $(+)$ or backward $(-)$ in time from the source and target frames, respectively.

Structures involved in continuation events do not interact with other structures and, thus, are generally characterized by small changes in geometric shape compared with splits and merges. Therefore, for a continuing source structure a corresponding target structure is expected in its neighborhood in the full attribute space and candidate targets can be detected by a nearest-neighbor (NN) search [15, 16] in this space. The NN search is conducted bidirectionally: the nearest neighbor in the target cloud is found for each source point and vice versa. The bidirectional, unrestricted NN search guarantees that all structures have at least one corresponding structure, which can lead to falsely detected correspondences for disappearing source structures or newly created target structures. These false correspondences will be rejected by the constraining process, as explained in §2.2. The NN search for each source (target) point predominantly detects targets involved in potential continuation or merge (split) events.

Since topology-changing (merge, split, compound) events affect the geometric attributes more abruptly than the spatial attributes, an additional correspondence search in the spatial subspace is conducted excluding the geometrical attributes. This search is conducted as a bidirectional range, rather than a NN search, and thus requires the definition of a search radius. An individual search radius is assigned to each query point based on the half-diagonal of its OBB, with a provided tolerance ε_R (fig. 2). Since the search radius is associated with the query structure size, splits (mergers) are more likely detected when a source (target) structure is used as a query. Hence, prior to the radius search using the source (target) points as query, the target (source) backward (forward) projection of spatial attributes is conducted.

A confidence value $c_i \in [0, 1]$ is defined for each found correspondence and search stage. For the bidirectional NN search, the confidence value is computed as

$$c_i = \omega_{NN} \left[c_{NN} + (1 - c_{NN}) \left(1 - \frac{d_i}{\bar{d} + 3\sigma} \right) \right] \tag{4}$$

where ω_{NN} is a specified weight, $c_{NN} < 1$ is a minimum NN confidence value, d_i is the Euclidean distance between query and match points in the attribute space for the i-th found correspondence,

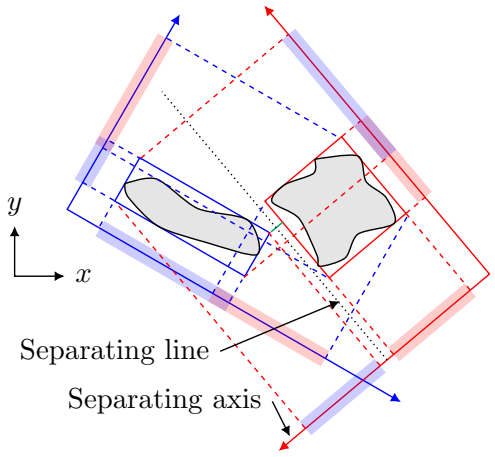

Figure 3: Illustration (in 2D, for clarity) of the separating axis theorem in two dimensions applied to OBBs of source (blue) and target (red) structures. Minimal distance (green) between OBBs as obtained from the GJK algorithm.

whereas $\bar{d}$ and σ are the mean and standard deviation of the distances of all found correspondences in this search stage. For the radius search, the confidence is defined as $c_i = \omega_R \left(1 - d_i/r_i\right)$ where ω_R is a specified weight, d_i is the center distance between the matched structures and r_i is the search radius of the query. Correspondences between the same pair of source and target structures found more than once in this multi-stage search are merged into a single correspondence with a cumulative confidence value.

2.2 Constraining of correspondence candidates

Correspondence constraints reject single correspondence candidates deemed not physically realizable, avoiding the formation of unphysical, complex events. A sequence of region-based constraints of increasing accuracy and computational cost is applied to each candidate correspondence and a confidence value is computed in each constraint.

In a first constraint, the minimal spatial distance between the OBBs of source and target structures involved in a correspondence serves as a measure for the realizability (fig. 3). The distance between the source and target OBBs (which are convex sets) is calculated using Gilbert-Johnson-Keerthi's (GJK) algorithm [17, 18], based on Minkowski's separating axis theorem (SAT)[19]. The OBB distance is compared to a measure defined as the maximum of $\hat{\mu} = 3V/A$ of the source and target structures. If the minimal distance of the OBBs is larger than this measure (up to a specified tolerance), the correspondence is rejected. A confidence value is assigned to passing correspondences as

$$c = \omega \left[1 - \frac{\|d_{\min}\|}{\varepsilon \, \max\left(\hat{\mu}_s, \hat{\mu}_t\right)}\right], \tag{5}$$

where $d_{\min}$ is the minimum distance between the OBBs and ω and ε are specified confidence weight and tolerance values, respectively. The measure of the source and target structures is indicated as $\hat{\mu}_s$ and $\hat{\mu}_t$, respectively.

Since OBBs are inaccurate representations of highly convoluted structures (fig. 4), a second constraint is applied to the remaining correspondences. This more accurate and computationally expensive constraint solves distance queries between the actual isosurfaces, rather than between their OBBs, by calculating the minimum of point-to-point distances [20] between the surfaces.

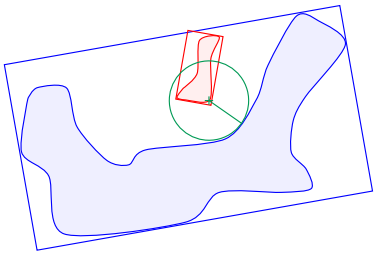

Figure 4: Illustration of the minimal proximity between two generic shapes with overlapping OBBs. The target structure (red) is enclosed in the concave region of the source structure (blue). Despite of overlapping OBBs, the structures do not intersect, but show a significant distance (green) between each other compared to their size.

Again, the distance between structures is compared to the maximum of the $\hat{\mu}$ parameter of source and target structures to determine the confidence value of passing correspondences.

2.3 Formation, constraining and optimization of events

An *event* groups correspondences with common source or target structures. By inspection of the set of correspondences a list of candidate events describing the structure interactions between source and target frames is formed. A sequence of constraints is applied to test the physical realizability of the events and to examine if an event can be simplified into subevents, defined as subsets of the correspondences of the whole event (i.e., each accepted subevent satisfies the event constraint).

To avoid false merge events resulting from small disappearing structures proximal to other structures, a first constraint is applied that removes merging source structures with a number of points of the surface triangulation below a minimum threshold. Second, a conservation constraint is applied based on an attribute assumed to be conserved in the (sub)event within a specified tolerance. The conserved attribute must differ from those utilized in the correspondence search. For the tracking of passive scalar structures, their mass (estimated as the product of the surface-averaged density and the volume enclosed by the structure) is chosen as the conserved attribute used in the event constraining process. The realizability of the (i-th sub)event based on a conserved attribute α is assessed by comparing the sum of the conserved attribute between the n source and m target structures of the (sub)event, for which a score $s_{i,\mathrm{c}}$ is defined as

$$s_{i,\mathrm{c}} = \frac{\min\left(\alpha_{i,s}, \alpha_{i,t}\right)}{\max\left(\alpha_{i,s}, \alpha_{i,t}\right)}, \quad \alpha_{i,s} = \sum_{j=0}^{n} \alpha_{i,j}^{s}, \quad \alpha_{i,t} = \sum_{j=0}^{m} \alpha_{i,j}^{t} \tag{6}$$

where $\alpha_{i,j}^{s}$ and $\alpha_{i,j}^{t}$ are the values of the conserved attribute of the event's sources and targets, respectively. A (sub)event is considered realizable if its score is above a specified threshold. A mechanism to recover from a split (or merge) for which too many targets (or sources) are present in the original event is to extract subevents by removing one or multiple targets (or sources) from the event and testing the realizability of the resulting subevents. For a split (merge) event with n targets (sources), the number of subevents to be tested is given by $c = \sum_{r=1}^{n} n!/(n-r)!r!$. Similarly, detected compound events are tested for decomposition into simpler events based on the conserved quantity.

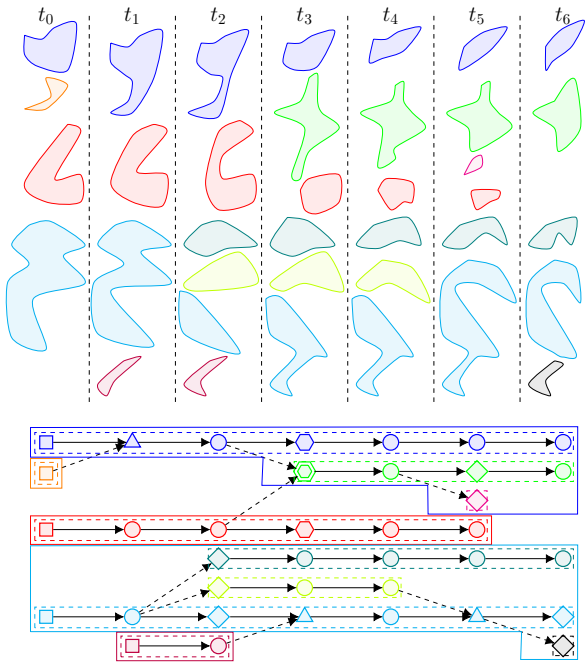

Figure 5: Illustrative representation of temporal structure evolution and interaction as a directed acyclic graph. Dominant (non-dominant) edges in events indicated as solid (dashed) arrows. Node and structure colors identify the same structure in multiple frames. Node shapes indicate the event type from which the structure results: □ creation, ○ continuation, △ split, ◇ merge, and ⬡-⬢ compound events. Trees and branches indicated as solid and dashed wrapping. Branch classified as primary (- -,- -, - -), incoming (- -, - -), outgoing (- -, - -, - -, - -) and reconnecting (- -).

2.4 Graph representation of temporal evolution of flow features

Graph data structures represent pairwise relationships between objects and are therefore ideal to organize the temporal evolution of flow features by mapping accepted events between pairs of frames. Each vertex of the graph represents a flow structure at a certain instant in time, while each edge indicates a correspondence. Since vertices are ordered in temporal sequence, the graph is directed and acyclic. An implicit vertex clustering results in a two-layer hierarchy of subgraphs, defined as *tree* and *branch* (fig. 5). Each branch represents the lifetime of one individual structure. Depending on the structure interaction, some trees in the graph may be disjoint from all other trees. The union of all trees describes the evolution of all structures over all frames of the dataset.

The source (target) vertex of a split (merge) has an out (in) degree greater than one, i.e., more than one correspondence with target (source) structures. Multiple vertices of degree higher than one exist in a compound event. The vertex clustering approach aims to continue branches in the building of these event types. Therefore, the *dominant* target (source) of each split (merger) must be selected based on a set of criteria. For a compound event, the process is applied to the sub-split and sub-merge events to select dominant sources and targets. Allowing n criteria, the total score of the i-th candidate correspondence is calculated as a weighted sum of the scores of each criterion

$$s_{\text{total},i} = \sum_{j=0}^{n} \omega_j s_{ij}, \qquad \sum_{j=0}^{n} \omega_j = 1, \qquad s_{ij} \in [0,1] \tag{7}$$

where ω_j is the specified weight for the j-th criterion and s_{ij} is the score of the i-th candidate in

the j-th criterion.

The first criterion to decide on the dominant edge(s) of an event is based on the comparison between a specified conserved property C of the candidate and the reference, such as the volume or (estimated) mass of the structure. For a (sub-)split or (sub-)merger, the reference is the splitting source or the merged target, respectively. The score of the i-th candidate in this conservation-based criterion is determined as

$$s_{i,\text{conservation}} = \frac{\min\left(C_i, C_{\text{ref}}\right)}{\max\left(C_i, C_{\text{ref}}\right)} \tag{8}$$

The second criterion considers the confidence value of each correspondence as the score, to prioritize high confidence in the selection of the dominant edge. For (sub-)merge events, a third criterion based on the lifetime of the source structure before the event is used. The lifetime-based score of the i-th source candidate is defined as

$$s_{i,\text{lifetime}} = 1 - \exp\left[-\frac{1}{2}\left(t_i - t_{i,0}\right)\right] \in [0, 1], \tag{9}$$

where $t_{i,0}$ is the time of the frame in which the i-th candidate is first present as a individual structure. Finally, the correspondence candidate that maximizes the total score, $s_{i,\text{total}}$, is selected as the dominant source or target of the (sub-)merge or (sub-)split event.

Branches are classified based on the connectivity of their start and end vertices [21]. The start vertex of a primary branch results from a creation event (with no predecessor), whereas its end vertex is a disappearing structure (with no successor). Branches that do not satisfy both criteria are considered secondary (fig. 5).

3 Application to Direct Numerical Simulation of isotropic turbulence and shock-turbulence interaction with scalar mixing

In Y1-Y2 we applied the tracking methodology to the first two cases of application that we included in our original proposal. The purpose of using these two canonical configurations is to elucidate the impact of shock waves on scalar mixing from a structural viewpoint. To that effect, we compared temporally decaying HIT and the canonical statistically stationary interaction of a nominally planar shock wave with spatially decaying isotropic turbulence (STI), at two different Mach numbers. We perform shock-capturing DNS following the simulation methodology described in our recent work (Gao et al. [22]).

The STI simulations are conducted with $Re_\lambda = 40$, $M_t = 0.2$ and $M = \{1.5, 3.0\}$, where Re_λ and M_t values are taken just upstream of the shock location. The initial values of Re_λ and M_t in the corresponding DHIT configuration are chosen as $(Re_\lambda, M_t) = (46, 0.23)$ for the STI with $M = 1.5$ (denoted STI-M1.5) and $(Re_\lambda, M_t) = (42, 0.21)$ for the STI with $M = 3.0$ (denoted STI-M3), to account for the decay of Re_λ and M_t from the inlet to the shock location in the STI. The Schmidt number, defined as the ratio of the kinematic viscosity $\nu = \mu/\rho$ of the fluid and the diffusivity D_m of the m-th passive scalar, is chosen to be $Sc = 1$ in all DHIT and STI simulations, characteristic of supersonic mixing of gases. For the STI flow configuration, a resolution of $1280 \times 384 \times 384$ for the domain of size $4\pi \times 2\pi \times 2\pi$ was found to be grid converged for the range of flow parameters here considered [see 22]. The DHIT has a cubic domain of edge length 2π and the grid resolution in each coordinate direction of the DHIT configuration matches the transverse resolution of the STI simulation.

Three passive scalar fields, denoted as ϕ_λ, $\phi_{2\lambda}$, and $\phi_{4\lambda}$, are initialized as collections of uniformly spaced spheres of uniform radius equal to one, two, and four times, respectively, the initial Taylor microscale, λ, of the underlying decaying turbulence.

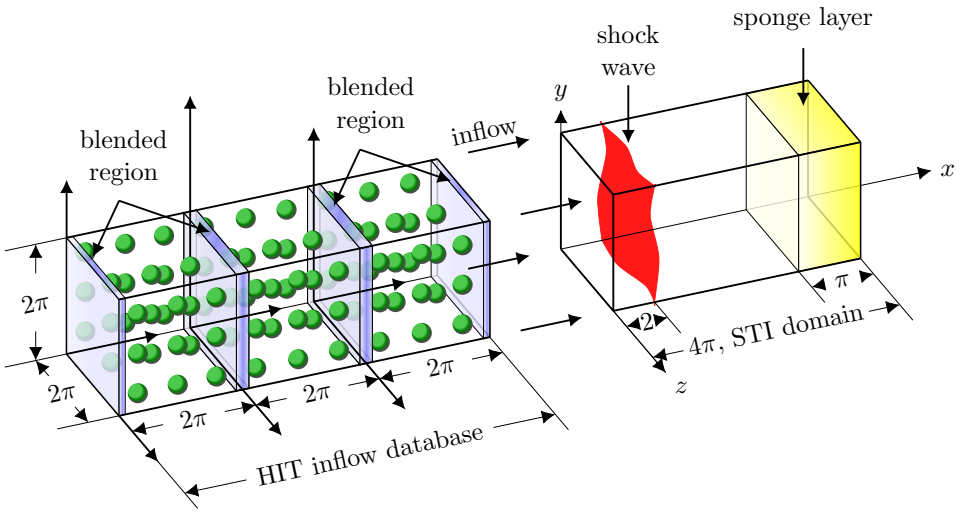

Figure 6: Problem setup for STI configuration and blended HIT precursor simulations to form the inflow database with passive scalar structures of spherical initial shape. Length of inflow database reduced in figure. Adapted from Gao et al.[22].

Symbol	Radius	Transition	Spacing	Number
ϕ_λ	λ	5η	3λ	12^3
$\phi_{2\lambda}$	2λ	10η	6λ	6^3
$\phi_{4\lambda}$	4λ	20η	12λ	3^3

Table 1: Initial configuration of passive scalar structures used in the DHIT and STI configuration. Initialized number of structures per DHIT domain block. Radial transition length from $\phi_{\min}$ to $\phi_{\max}$, expressed in terms of the initial Kolmogorov lengthscale, η.

The three initial configurations of passive scalar structures we have studied are summarized in table 1. The same sampling interval length of $\Delta t = \tau_0/12.7$ is used for the tracking for all structures in the STI with $M = 1.5$ and corresponding DHIT, where $\tau_0 = \lambda/u_{\text{rms}}$ is the initial large-eddy turnover time of the DHIT configuration. To account for the higher upstream velocity, the sampling frequency is doubled in the STI with $M = 3.0$ and in the corresponding DHIT.

3.1 Geometric analysis and evolution of passive scalar structures in DHIT and STI

We have applied the tracking algorithm introduced in §2 to analyze the temporal evolution of passive scalar structures extracted from the DHIT and STI numerical datasets discussed in §3.

3.2 Temporal and streamwise distribution of events

To compare the structure evolution in DHIT and STI, the time coordinate of the DHIT simulations is translated into an equivalent streamwise coordinate of the STI as

$$x_{\text{dhit}} = \begin{cases} u_{\text{u}} t & \text{for } t < x_{\text{s}}/u_{\text{u}} \\ x_{\text{s}} + u_{\text{d}}(t - x_{\text{s}}/u_{\text{u}}) & \text{else} \end{cases} \tag{10}$$

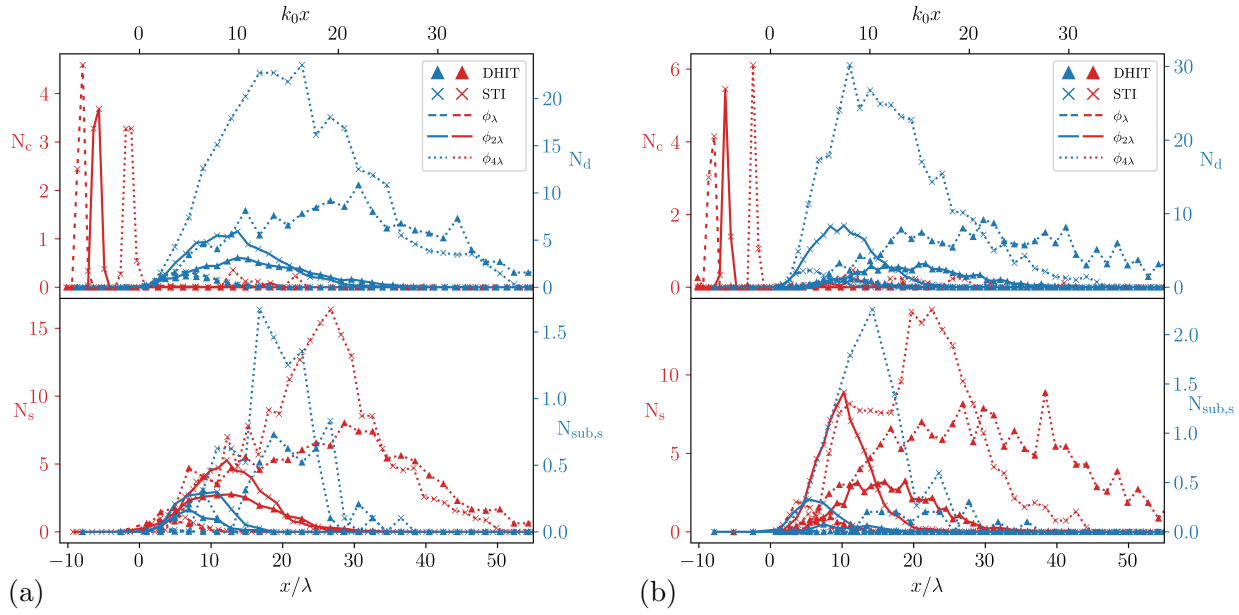

Figure 7: Streamwise distribution of different event types for the ϕ_λ, $\phi_{2\lambda}$ and $\phi_{4\lambda}$ passive scalar structures in DHIT and STI configurations for $M = 1.5$ (a) and $M = 3.0$ (b). Relative histogram counts are normalized by the bin size and the number of initial (DHIT) or incoming (STI) structures. N_c, number of creations. N_d, number of disappearances. N_s, number of splits. $N_{\mathrm{sub},s}$, number of sub-splits of compound events. Shock location at $x/\lambda = 0$.

where x_s is the shock location and u_u and u_d are the mean streamwise flow velocities upstream and downstream of the shock.

The equivalent-streamwise distribution of different event types in STI and DHIT configurations is presented in fig. 7, where the streamwise coordinate is normalized by the k_0 wavenumber and the initial Taylor micro-scale, λ, of the DHIT configurations. Expected creations correspond to structures entering the STI domain and to the initial structures in the DHIT. Scalar dissipation eventually reduces the scalar value below the isosurfacing threshold, resulting in the disappearance of the structures. The peak location of creations is shifted downstream as the structures increase in initial size from ϕ_λ to $\phi_{4\lambda}$ and become closed surfaces (triggering the creation) at a farther downstream location (fig 7).

The distribution of disappearances is linked to that of splits, as most (early) splits have one dominant structure similar in size to the parent structure and a number of smaller targets that disappear in close proximity to the split event. The normalized number of splits and disappearances is larger in the STI than in the DHIT configuration, indicative of shock-induced mixing enhancement, and further increases with the shock Mach number and the initial size of the structures. For all initial sizes, a higher shock Mach number induces more splits in closer proximity to the shock. While disappearances and splits peak approximately at the same streamwise location for ϕ_λ and $\phi_{2\lambda}$ in STI and DHIT, they peak closer to the shock for the $\phi_{4\lambda}$ structures, which indicates increased benefit of mixing of those larger structures by the shock interaction. Disappearance events extend farther downstream than split events, corresponding to scalar diffusion leading to continuation and disappearance without further splitting.

The number of compound events is larger in STI than in DHIT, increasing with Mach number, and peaks closely after the shock. The sub-splits hidden in compound events contribute to the

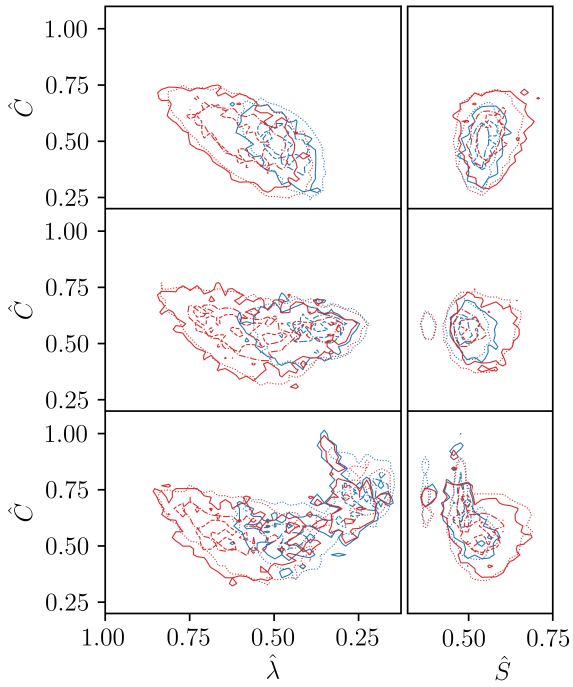

Figure 8: Joint histograms of geometrical attributes of source (blue) and target (red) structures of split events in DHIT and STI-M1.5. Top: ϕ_λ, Center: $\phi_{2\lambda}$, Bottom: $\phi_{4\lambda}$. Contour lines for 0.2 isovalue for DHIT (solid) and STI (dotted); 0.8 isovalue for DHIT (dashed) and STI (dash-dotted).

number of disappearing structures in fig. 7 closely behind the shock, especially for the $\phi_{4\lambda}$ structures, as the number of compounds per incoming structure is larger for increasing initial size of the structure (fig. 7). The normalized number of mergers is small compared to the number of splits. Similar to sub-splits, there is a considerable number of sub-merge events hidden in compounds. While the number of pure splits is clearly larger than the number of compounds, the latter is comparable or even larger than the number of pure mergers, especially in the STI configuration, where more compounds, and hence more sub-mergers, occur. While there is typically one sub-merge per compound event, multiple sub-splits of potentially higher order occur per compound. Compounds are of importance to capture all cases of structure interactions in the scalar mixing process. Therefore, it is essential for the tracking to account for compound events rather than neglecting them as in most previous methods.

3.3 Split and merge events in geometrical feature space

The geometric signature $\{\hat{S}, \hat{C}, \hat{\lambda}\}$ of source and target structures of split and merge events is investigated, focusing on the effects of the initial structure size and the shock with Mach number $M = 1.5$ (similar conclusions were found for the higher Mach number $M = 3.0$). The joint histograms $(\hat{\lambda}, \hat{C})$ and $(\hat{S}, \hat{C})$ of the geometrical attributes of source and target structures of split events in DHIT and STI, shown in fig. 8, indicate that splitting source structures are characterized by lower values of the compactness, $\hat{\lambda}$, and the shape index, $\hat{S}$, than the resulting target structures, while the curvedness, $\hat{C}$, is comparable between sources and targets. Structures characterized by low compactness, $\hat{\lambda}$, are more stretched and likely to contain a ligament-like portion that increases the probability of these structures becoming the source of a split.

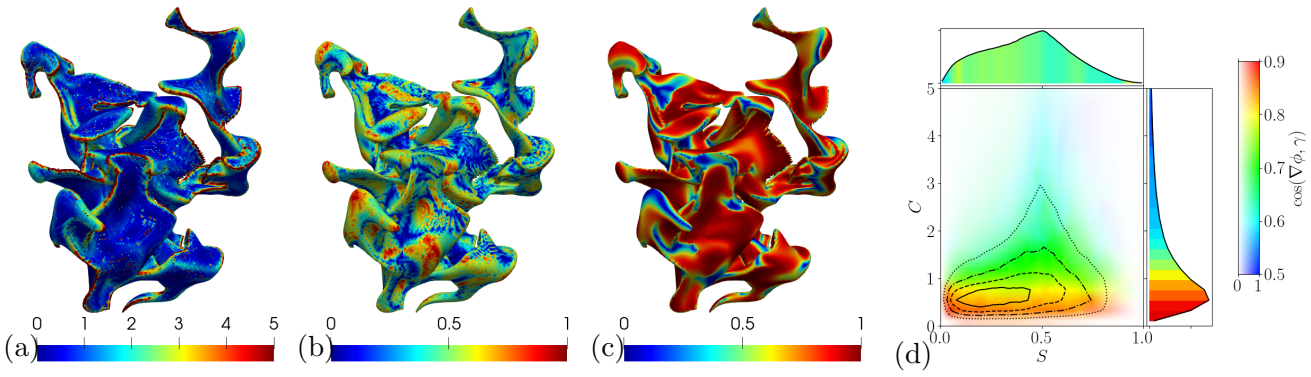

Figure 9: Local values of curvedness (a), shape index (b) and the alignment between the most compressive eigenvector $\boldsymbol{\gamma}$ of the strain-rate tensor and the scalar gradient $\nabla\phi_{4\lambda}$ (c) mapped on an isosurface of the $\phi_{4\lambda}$ field at $t/\tau_0 = 4.3$. (d) Average alignment of scalar gradient and $\boldsymbol{\gamma}$ conditioned on S and C (hue) accounting for the area-based joint PDF (saturation, from white for zero area coverage to the full color for the maximum area coverage), with area-based marginal PDFs of S and C colored by the average alignment conditioned on each variable. Equispaced contour lines for 0.2 (dotted), 0.4 (dash-dotted), 0.6 (dashed), and 0.8 (solid) of the peak joint PDF value.

The compactness $\hat{\lambda}$ of splitting sources in DHIT (fig. 8) decreases with larger initial size of the structures from ϕ_λ to $\phi_{4\lambda}$, as the structures become more convoluted and stretched before they split. The higher convolution of the source structures for bigger initial size also translates into a higher curvedness, $\hat{C}$, and an increased amount of hyperbolic surface points, which lowers the shape index ($\hat{S} < 0.5$). In contrast, elliptical points ($\hat{S} > 0.5$) are dominant in splitting ϕ_λ structures.

For $\phi_{2\lambda}$ and $\phi_{4\lambda}$ structures, the ($\hat{S}$,$\hat{C}$) joint PDF of source structures is essentially enclosed by that of the target structures (fig. 8). Hence, this target is located in close proximity to the splitting source in the geometrical feature space. Compared to the DHIT, the compression of the passive scalar structures by the shock in the STI decreases the compactness, $\hat{\lambda}$, and shape index, $\hat{S}$, of splitting source structures (fig. 8).

The $(\hat{\lambda}, \hat{C})$ and $(\hat{S}, \hat{C})$ joint PDFs of the geometrical attributes of source and target structures of merge events in DHIT and STI (not shown) present opposite conclusions than for splits. Merged target structures are characterized by a lower compactness. The difference between merging sources and merged targets in terms of the shape index is less pronounced than for split events. The dependence of the geometric signature on the initial structure size observed for splitting source structures also applies to merged target structures.

3.4 Surface correlations between local geometry and physical quantities (Integration of flow physics and geometry)

The local geometry of a surface can be characterized by the pointwise values of curvedness C and the shape index S on the surface (fig. 9a,b). Additionally, pointwise physical quantities can be mapped on the surface, such as the alignment between the scalar gradient, $\nabla\phi$, and the most compressive eigenvector $\boldsymbol{\gamma}$ of the strain-rate tensor (fig. 9c). To elucidate correlations of local physical quantities on a passive scalar isosurface with its local geometry, the average alignment of $\nabla\phi$ and $\boldsymbol{\gamma}$ conditioned on S and C accounting for the area-based joint PDF is obtained (fig. 9d). For the sample structure shown in fig. 9, a clear correlation between flat regions (low C) and high alignment of $\nabla\phi$ and $\boldsymbol{\gamma}$ is observed on the surface renderings (fig. 9a-c) and the conditioned joint

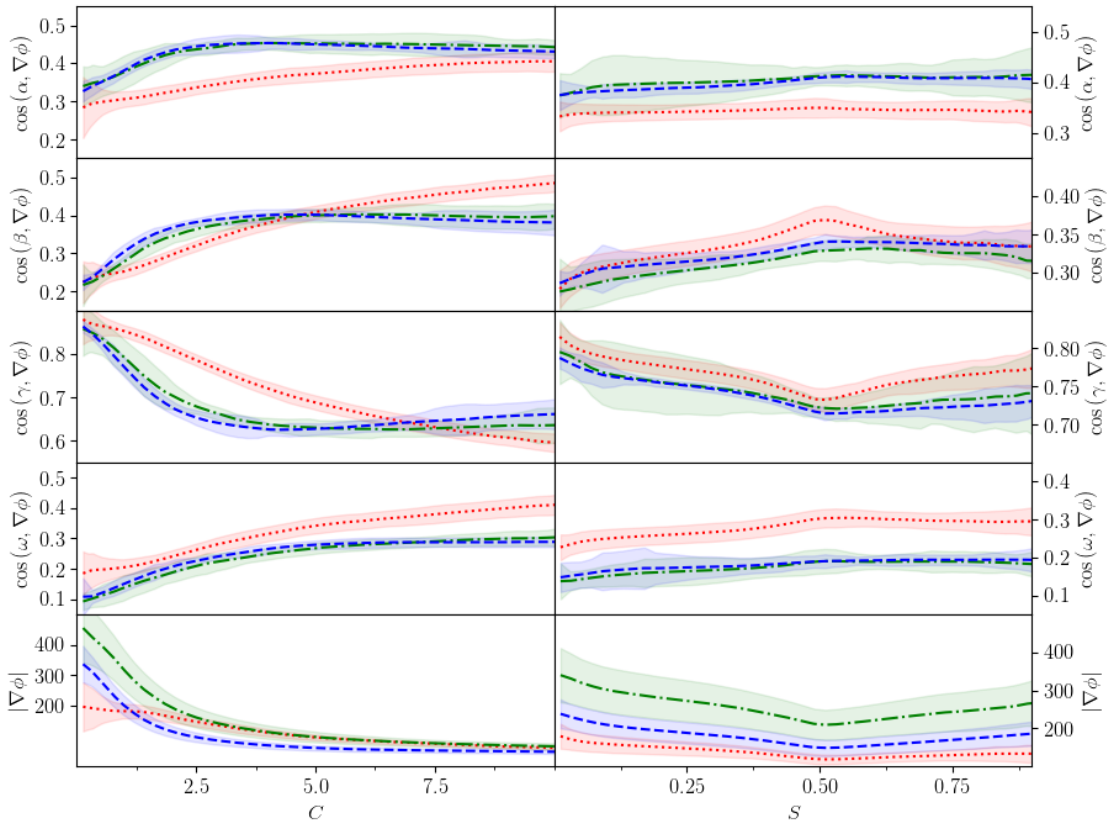

Figure 10: Surface distributions of the alignment between the scalar gradient and the eigenvectors $(\boldsymbol{\alpha}, \boldsymbol{\beta}, \boldsymbol{\gamma})$ of the strain-rate tensor and the vorticity $\boldsymbol{\omega}$ and the magnitude of the scalar gradient conditioned on local curvedness (left) and shape index (right) of $\phi_{4\lambda}$ in STI-M1.5 at different streamwise locations: $k_0x \in [-2.2, -1.8]$ (···), $k_0x \in [4.0, 4.4]$ (-··) $k_0x \in [8.0, 8.4]$(- -). Lines represent ensemble mean of the conditional PDF, while colored region enclose two standard deviations.

PDF (fig. 9d).

Figure 10 shows surface distributions, conditioned on S and C, of alignments between $\nabla\phi$, the strain-rate eigenvectors and vorticity, and the scalar gradient magnitude obtained from $\phi_{4\lambda}$ isosurfaces centered around four different streamwise intervals in the STI-M1.5 simulation. Positive correlations with $C < 5.0$ are observed for the alignment of $\nabla\phi$ (which is normal to the isosurface at every point) with $\boldsymbol{\alpha}$ and $\boldsymbol{\beta}$, indicating that regions of higher curvature present better alignment between the scalar gradient and the most extensional and intermediate strain-rate eigenvectors. The opposite trend is observed for the alignment with the most compressive strain-rate eigenvector, $\boldsymbol{\gamma}$, indicating that flatter regions of the isosurfaces present larger alignment between $\nabla\phi$ and $\boldsymbol{\gamma}$. For $C < 5.0$ these correlations are strengthened as the isosurfaces are transported downstream. For highly-curved regions ($C > 5.0$) of structures in the post-shock domain, alignment with $\boldsymbol{\alpha}$ and $\boldsymbol{\beta}$ slightly decreases, whereas alignment with $\boldsymbol{\gamma}$ increases. Across the shock, the scalar gradient alignment with $\boldsymbol{\alpha}$ ($\boldsymbol{\gamma}$) increases (decreases) for the entire range of the shape index, S. A decreased alignment with $\boldsymbol{\beta}$ downstream of the shock is more pronounced at parabolic points ($S = 0.5$) of the isosurfaces.

For the alignment of scalar gradient with the most extensive strain-rate eigendirection, $\boldsymbol{\alpha}$, the correlation with S is less pronounced than with C: at the farther downstream locations, there is

a slightly positive correlation with the shape index in its hyperbolic range ($S < 0.5$). The same correlation is found for the alignment with the intermediate eigendirection, $\boldsymbol{\beta}$, farther downstream. Contrary to $\boldsymbol{\alpha}$ and $\boldsymbol{\beta}$, alignment of $\nabla\phi$ with the most compressive strain-rate eigendirection, $\boldsymbol{\gamma}$, shows a negative correlation with the shape index for hyperbolic points. In the elliptical range of shape index ($S > 0.5$), however, the correlation is positive, but becomes less pronounced farther downstream. The alignment between scalar gradient and vorticity, $\boldsymbol{\omega}$, shows a positive correlation when conditioned on C and with S in its hyperbolic range. Hence, the anti-correlation between $\nabla\phi$ and $\boldsymbol{\omega}$ is more pronounced on flatter surface regions.

3.5 Trajectories of primary structures in the feature space (graph query and state-space trajectories)

The deformation of passive scalar structures is analyzed by means of their trajectories in the geometrical feature space $\{\hat{S}, \hat{C}, \hat{\lambda}\}$. To focus on the temporal evolution of primary structures, we consider only graph branches whose start vertex results from a creation event and end vertex is a disappearing structure.

Initially, all $\phi_{4\lambda}$ structures in the DHIT are spheres and thus their trajectories have a common starting point in the feature space at $(\hat{S}, \hat{C}, \hat{\lambda}) = (1, 1, 1)$, as shown in fig. 12. These $\phi_{4\lambda}$ isosurfaces become highly convoluted with time (see also fig. 13), causing a rapid increase in the curvedness, $\hat{C}$, and a decrease in the shape index, $\hat{S}$, due to the occurrence of hyperbolic surface points ($S < 0.5$). The deviation from the spherical shape also lowers the compactness, $\hat{\lambda}$, of the structures as they are stretched. After reaching the maximum curvedness, all structures follow a nearly linear trajectory in the $\hat{C}$-$\hat{\lambda}$ plane towards the approximate $(0.7, 0.25)$ location, lowering both their curvedness and compactness. The shape index, $\hat{S}$, follows a rapid initial transition from 1 (spherical shape) to 0.5, reached as the maximum $\hat{C}$ is attained. The subsequent decrease of $\hat{C}$ and $\hat{\lambda}$ has a lesser effect on $\hat{S}$, indicating a balance between the surface area coverage of hyperbolic and elliptic local geometries on the convoluted surfaces.

Until the occurrence of the first non-continuation events, the change in shape from one frame to the next (given by the distance between consecutive trajectory points in fig. 12) monotonically decreases due to the viscous decay of the underlying turbulent background field. As the stretching increases (for $\hat{\lambda} < 0.5$), the first splits occur in the evolution of the structures. Highly stretched structures tend to split over a sequence of frames. However, despite this cascade of split events, the change in shape of the primary structure itself is comparable to that of a continuation event. Splits occurring in this early stage of the evolution tend to be dominated by one target structure (similar in shape to the splitting source structure) and other, much smaller targets. As the dominant target continues the branch of the primary structure, its geometrical signature is only moderately altered by the split. This geometric similarity between the source and dominant target structure is also observed in the joint PDFs of geometrical attributes (fig. 8).

After these split cascades the structures have reached their minimum compactness and subsequent split events tend to increase the compactness and the shape index of the primary structure while preserving its curvedness, consistent with the joint PDF of splits in the geometrical feature space discussed in §3.3. These later splits do not form a cascade, even though the branch section between splits characterized by a decreasing curvedness and compactness remains short in some cases. The final stage of primary structure lifetime is characterized by continuation events with increasing amount of elliptical surface points and increasing compactness, making further splitting of the structure less likely. This trend is in accordance with the streamwise distribution of splits compared to disappearance events, discussed in §3.2.

From the collection of individual geometrical trajectories, ensemble statistics are calculated to

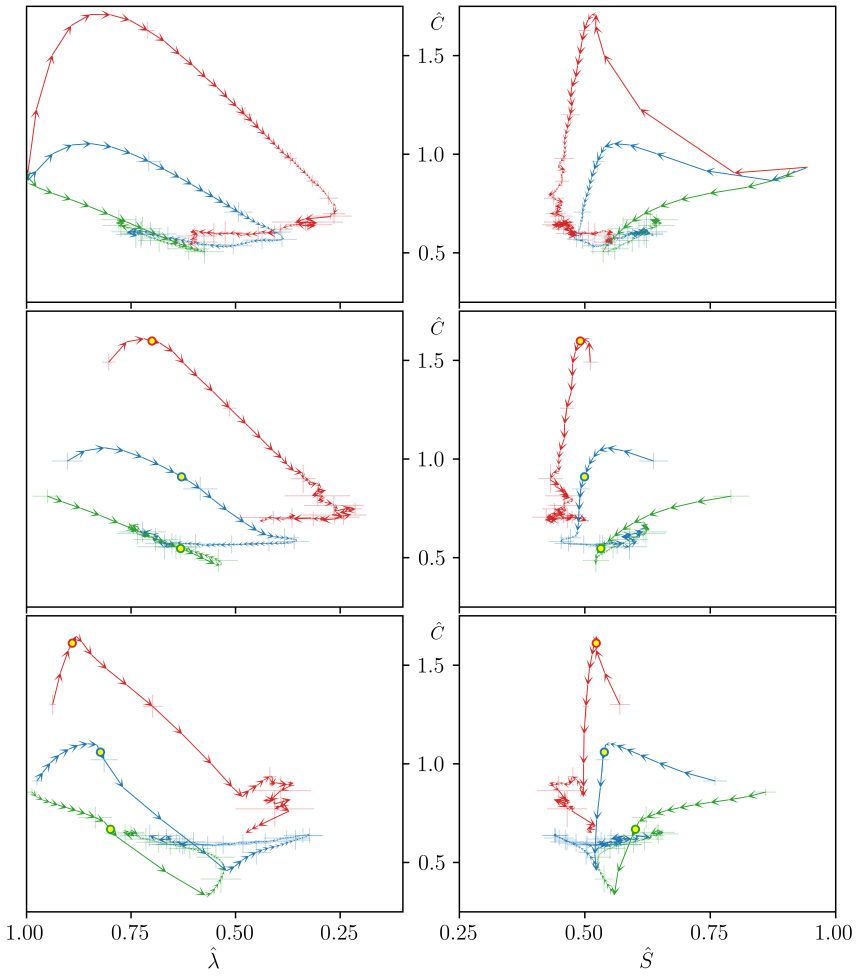

Figure 11: Ensemble mean trajectories of primary structures of ϕ_λ (green), $\phi_{2\lambda}$ (blue), and $\phi_{4\lambda}$ (red), in the $(\hat{S}, \hat{C}, \hat{\lambda})$ geometric space, for DHIT (top), STI with $M = 1.5$ (center), and STI with $M = 3.0$ (bottom) cases. Arrows at each tracking time step indicate the direction of time. Error bars indicate one standard deviation of ensemble trajectories in each geometric parameter, plotted every eighth tracking step for clarity. The yellow circle marks the mean shock-crossing tracking step for the STI cases. Each trajectory considers tracking steps relative to its own creation event.

	STI with $M = 1.5$					STI with $M = 3.0$				
	DHIT			STI		DHIT			STI	
	ϕ_λ	$\phi_{2\lambda}$	$\phi_{4\lambda}$	ϕ_λ	$\phi_{2\lambda}$	ϕ_λ	$\phi_{2\lambda}$	$\phi_{4\lambda}$	ϕ_λ	$\phi_{2\lambda}$
$(\bar{x}_d - x_s)/\lambda$	10.17	28.99	54.2	7.78	15.33	12.9	31.5	64.6	5.9	11.94
$(\bar{x}_{c,s} - x_s)/\lambda$	3.61	9.93	15.71	3.64	7.34	6.5	12.9	23.9	3.11	5.5
$(\bar{x}_{c,e} - \bar{x}_{c,s})/\lambda$	1.09	2.63	7.40	0.81	3.07	0.51	0.94	2.1	0.39	1.6

Table 2: Normalized mean disappearance location (top row), mean start location of split cascade (center row) and mean spatial length of split cascade (bottom row) for primary structures of type $\phi_\lambda, \phi_{2\lambda}$ and $\phi_{4\lambda}$ in STI for $M = 1.5$ and $M = 3.0$ and corresponding DHIT flow configurations.

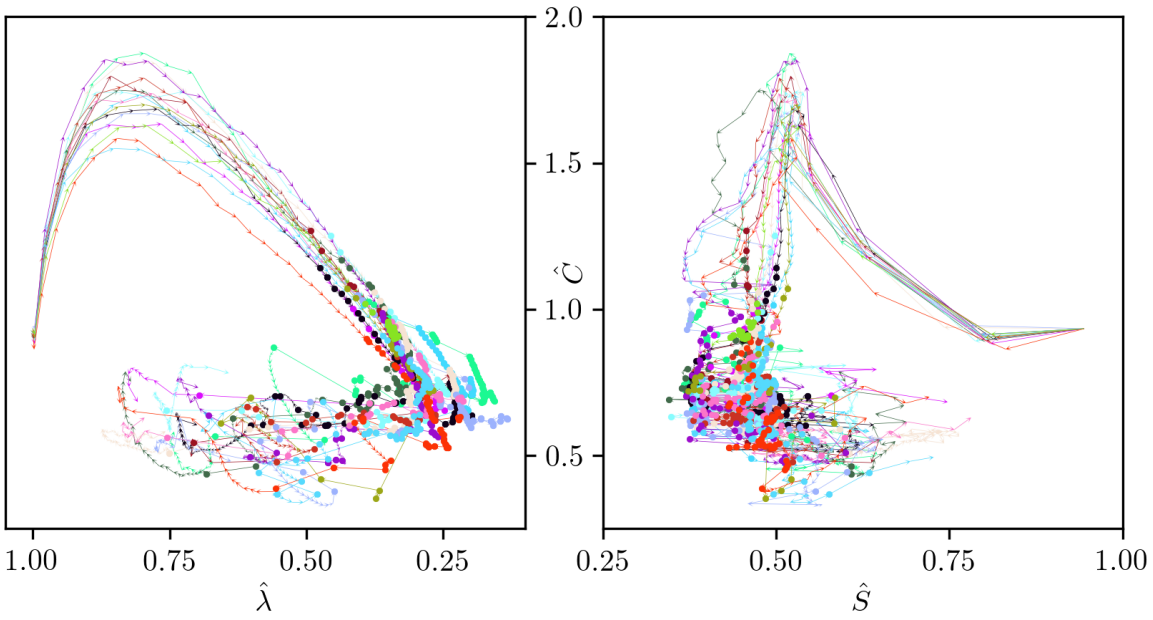

Figure 12: Trajectories in the geometrical feature space of individually tracked, primary $\phi_{4\lambda}$ structures in DHIT. Arrowheads signal temporal direction from frame to frame. Circle markers indicate start and end points of sections of a branch within which only continuation events occur.

obtain the mean trajectory and its standard deviation for primary structures of each scalar field (ϕ_λ, $\phi_{2\lambda}$, and $\phi_{4\lambda}$) in DHIT and STI ($M = 1.5$, and 3.0). Ensemble trajectories, shown in fig. 11, enable a characterization of the effects of the initial size and the shock compression on the geometric evolution of the structures.

While all three mean trajectories have the spherical starting point $(\hat{\lambda}, \hat{S}, \hat{C}) = (1, 1, 1)$, the initial evolution of the curvedness varies with initial size. Whereas the ensemble curvedness $\hat{C}$ initially increases for medium ($\phi_{2\lambda}$) and, especially, large ($\phi_{4\lambda}$) structures, it decreases for smaller (ϕ_λ) structures, as they are less convoluted by the background turbulence eddies. With increasing initial structure size, the ensemble mean trajectory reaches lower values of the shape index, $\hat{S}$, favoring hyperbolic points, and also lower compactness, $\hat{\lambda}$, indicative of an increased convolution and stretching. At the end of their lifetime, structures of all the scalar fields considered tend towards the same geometrical attributes: moderate compactness and curvedness with predominantly elliptical points.

The dependence of surface convolution and stretching on initial structure size is reflected in the mean area evolution of primary structures in DHIT (fig. 14), suggesting a degree of self-similarity. Exponential area growth has been reported for the evolution of Lagrangian structures in statistically stationary turbulence [23, 24, 25, 26, 27]. In the present study, despite the temporally decaying turbulence and diffusion acting on the (non-Lagrangian) passive scalar structures, an exponential time dependence of the form $A(t/\tau_0)/A_0 = a \exp(b\, t/\tau_0)$ accurately models the early, stretching-dominated surface area evolution, with a and b constant. A larger initial area growth is observed for initially larger structures and Taylor-Reynolds number ($Re_\lambda = 46$ compared with 42, corresponding to the inflow turbulence used for STI cases with $M = 1.5$ and 3.0, respectively). After the exponential growth, the area growth rate decreases as the dissipation takes over the surface stretching and the surface area reaches its maximum. In the following diffusion-dominated

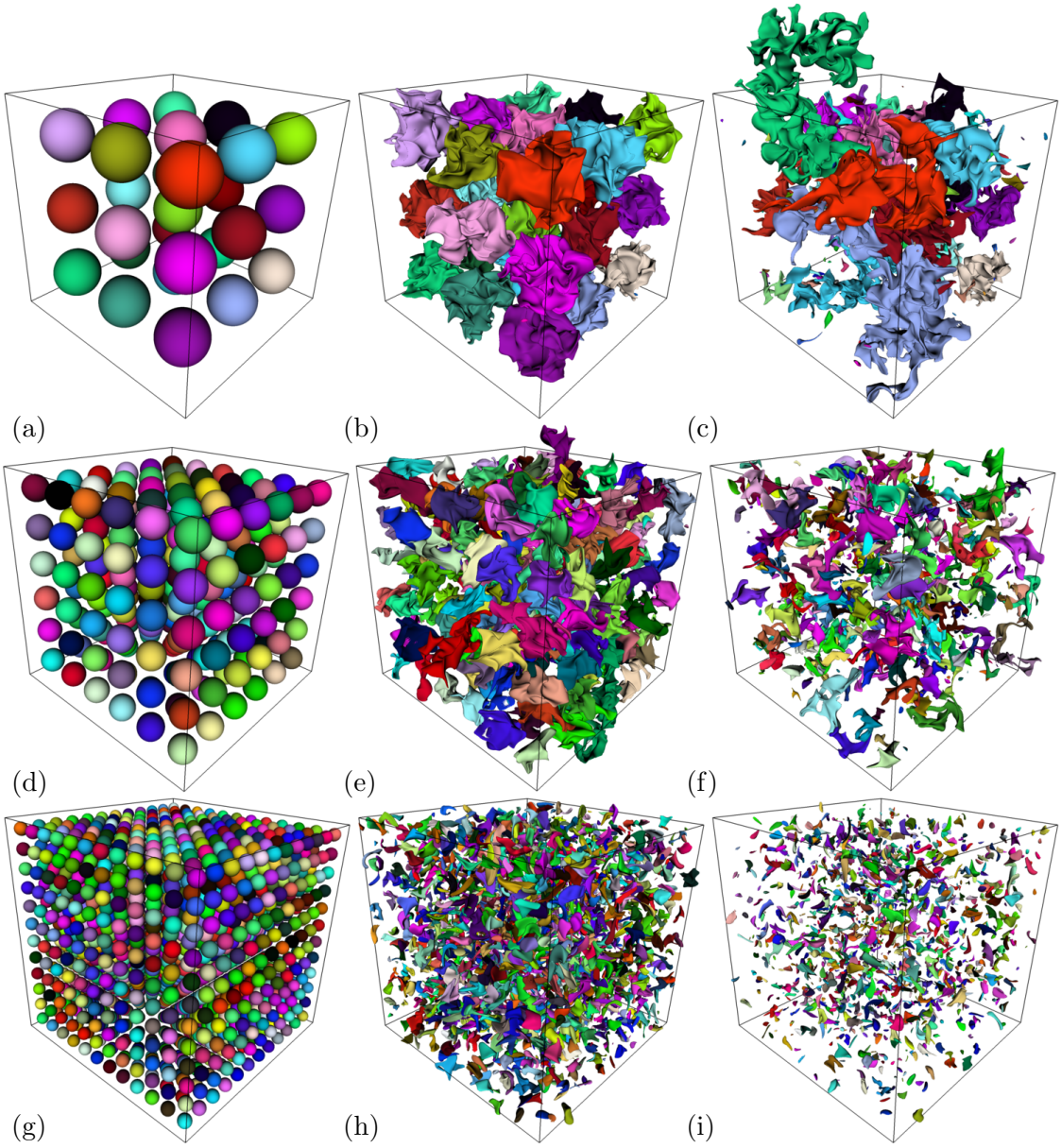

Figure 13: Evolution of structures educed from $\phi_{4\lambda}$ (a-c), $\phi_{2\lambda}$ (d-f) and ϕ_{λ} (g-i) scalars in DHIT captured in different frames from left to right: $t/\tau_0 = 0.0$ (a,d,g), $t/\tau_0 \approx 1.65$ (b,e,h), $t/\tau_0 = 4.5$ (c), $t/\tau_0 = 3.5$ (f), $t/\tau_0 = 2.4$ (i). Coloring indicates the identification of the individually tracked structures. Thus, color changes are associated with split and merge events. Periodic reconnection has been applied to structures crossing boundaries. For instance, in (c) the top part of the green structure is located outside the computational domain as it has been periodically reconnected to its lower part continuation inside the domain, leaving the void region on the opposite side. The rendering shows the periodically reconnected structure at one of its possible locations, all of which are considered in the correspondence search.

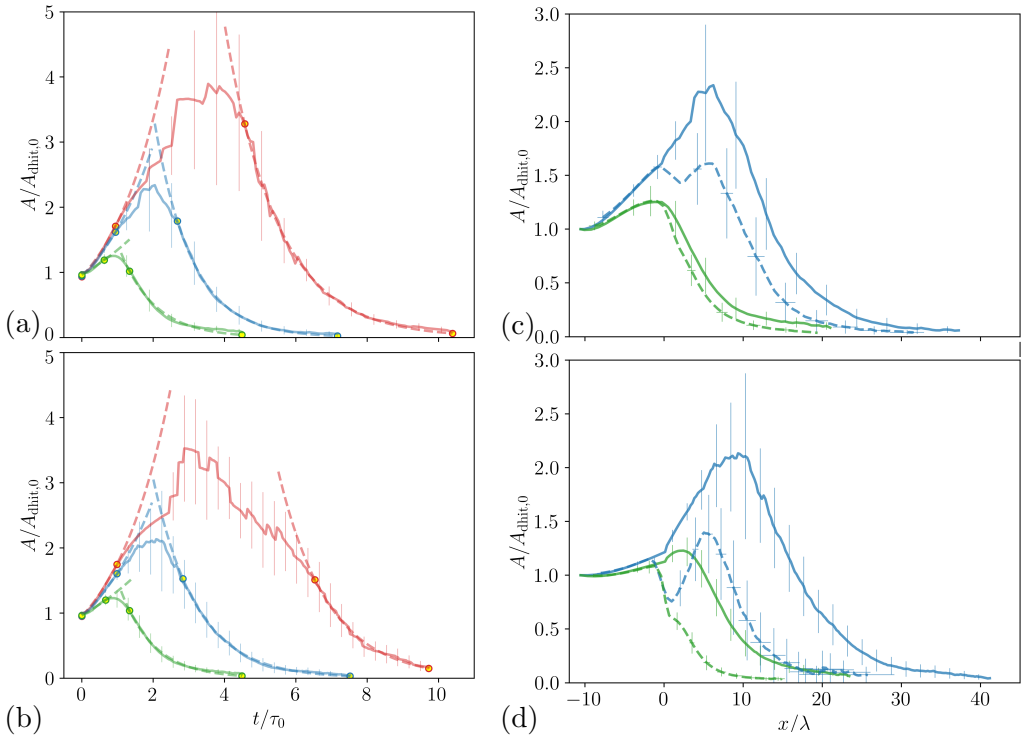

Figure 14: Temporal evolution of the normalized surface area (solid) of primary ϕ_λ (green), $\phi_{2\lambda}$ (blue) and $\phi_{4\lambda}$ (red) structures in DHIT with (a) $Re_\lambda = 46$ (corresponding to STI-M1.5) and (b) $Re_\lambda = 42$ (corresponding to STI-M3), where dashed lines represent best-fit curves of exponential growth and decay within the range indicated by the yellow markers. Streamwise evolution of the surface area of primary ϕ_λ (green) and $\phi_{2\lambda}$ (blue) structures in DHIT (solid) and STI (dashed), normalized by its initial DHIT value, for (c) DHIT/STI-M1.5 and (d) DHIT/STI-M3. Vertical bars represent one standard deviation, plotted every 8-th data point. Time coordinate in DHIT is transformed into spatial coordinate using equation 10.

regime, the area decrease also follows an exponential decay. The area decay rate is faster for more stretched surfaces with a larger surface area (i.e., $\phi_{4\lambda}$ structures). Cascade splits, which potentially shrink the surface area significantly, occur in this period of exponential surface area decay.

In the STI configurations, the structures are already deformed when they become closed surfaces upon entering the computational domain. Therefore, their mean trajectories in the geometrical feature space do not have a common spherical starting point and differ based on initial structure size (see center and bottom rows of fig. 11). In the $M = 3.0$ case, consecutive $\phi_{4\lambda}$ structures in the streamwise direction, decelerated by the shock, merge with each other and pile up within a distance from the shock below the initial structure radius, generating structures of large streamwise extent downstream of the shock. The number of primary $\phi_{4\lambda}$ structures with very long lifetimes in the STI configurations ($M = 1.5$ and 3.0) is too small to be statistically significant, so the final steps of their lifetime are excluded from the mean ensemble trajectory. Therefore, the final values of the geometrical properties attained at the end of the mean trajectories of $\phi_{4\lambda}$ structures differ from those of the smaller ϕ_λ and $\phi_{2\lambda}$ structures.

Shock-enhanced scalar dissipation lowers the lifetime of the primary structures in comparison to the corresponding DHIT as the structures are diffused faster below the threshold used for iso-surfacing (table 2). Compared to the DHIT, structure compression induced by the shock in the STI cases lowers the curvedness $\hat{C}$ (flattening the surface in directions normal to the compression) and the compactness $\hat{\lambda}$ (resulting in higher stretching, thus favoring splits). The deformation induced across the shock, particularly for the higher $M = 3$, is more pronounced for the smaller ϕ_λ structures, as a larger portion of the structure is compressed by the shock at once. For the STI-M3 case, the curvedness of the ϕ_λ and $\phi_{2\lambda}$ structures reaches a minimum after the structures are completely processed by the shock, and increases afterwards due to shock-induced turbulence amplification.

The lifetime reduction indicates that the mixing of larger structures benefits more from the shock-interaction: for the STI-M1.5 case, the mean disappearance location of ϕ_λ structures is reduced by 24%, while for $\phi_{2\lambda}$ structures the reduction is 47%. For the higher Mach number case, STI-M3, the lifetime reductions are 54% and 62%, respectively.

Turbulence amplification across the shock causes a surface area re-growth of $\phi_{2\lambda}$ structures in the post-shock region that is stronger for higher Mach number (fig. 14). This period of area re-growth correlates with the decreasing compactness parameter, $\hat{\lambda}$, in the feature-space trajectories (fig. 11), after the structures have been processed by the shock. While the amplification of the surface-averaged vorticity magnitude is similar for all initial structure sizes, the area re-growth is larger for intermediate ($\phi_{2\lambda}$) than for small (ϕ_λ) structures. At this post-shock location, the size of the ϕ_λ structures is smaller than the Taylor microscale and, therefore, those structures are mainly advected by the (shock-amplified) eddies. In contrast, $\phi_{2\lambda}$ structures are still large enough to be also stretched by the (smaller) turbulence eddies. Prior to the surface area re-growth in the post-shock region, the higher Mach number compression decreases the surface area more significantly.

Ensemble trajectory statistics are extended to include the evolution of two physical quantities averaged on each surface: the magnitude of the scalar gradient (indicative of the scalar dissipation on the surface) and the vorticity magnitude. These ensemble trajectories in the parameter space that combines geometrical features and averaged physical quantities are shown in fig. 15 for the DHIT case. For $\phi_{4\lambda}$ structures, the scalar gradient magnitude exhibits a rapid initial increase, due to stretching of the initial scalar transitional region. The peak in curvedness is reached significantly earlier than the peak in the scalar gradient magnitude. The geometry of $\phi_{4\lambda}$ structures, especially their curvedness and shape index, develops faster than both the scalar gradient and the vorticity magnitude at early stages of the trajectory. In contrast, for the smaller ϕ_λ structures, the decrease in scalar gradient magnitude is initially more pronounced than the geometric changes. During the

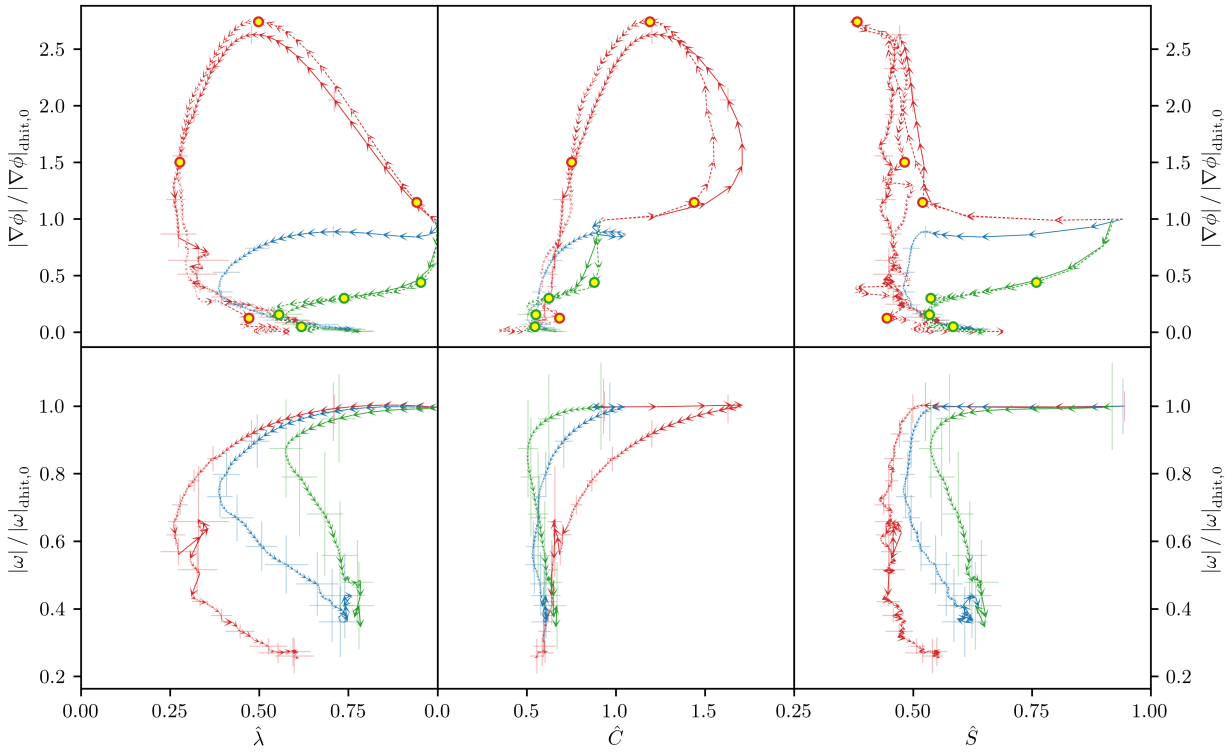

Figure 15: Ensemble mean trajectories (solid) of primary structures of ϕ_λ (green), $\phi_{2\lambda}$ (blue), and $\phi_{4\lambda}$ (red) for DHIT in the $(\hat{S}, \hat{C}, \hat{\lambda})$ geometric space with scalar gradient (top) and vorticity magnitude (bottom). Physical quantities normalized by their initial value in DHIT. Error bars include one standard deviation of ensemble trajectories in each geometric and physical parameter, plotted every eighth tracking step for clarity. For ϕ_λ and $\phi_{4\lambda}$ structures the individual closest-to-mean trajectory (dotted) is plotted with highlighted steps (yellow markers) corresponding to the structures rendered in figure 17.

cascade splits, not only is the geometrical signature of the primary structure marginally affected, as previously explained, but also both surface-averaged physical quantities. Since the turbulence is already fully developed at structure initialization, the surface-averaged vorticity magnitude exhibits a monotonic decay in DHIT, reaching lower values on the larger $\phi_{4\lambda}$ structures due to their longer lifetime.

The individual trajectory closest to the ensemble mean in terms of geometry and scalar gradient magnitude (and thus, scalar dissipation) is also shown in fig. 15 for $\phi_{4\lambda}$ and ϕ_{λ} structures. Figure 17 shows the structures corresponding to four highlighted steps of the closest-to-mean trajectory rendered with the alignment between the scalar gradient and the $\boldsymbol{\gamma}$ eigenvector of the strain-rate mapped onto the surface. The area-based joint and marginal probability density functions of S and C for the structures at the last highlighted step are also shown, indicating that for both structure sizes the largest curvedness on the surfaces is found at parabolic points ($S = 0.5$) that occur on the ridges of the convoluted surfaces. Previous studies have reported highly curved surface elements of propagating surfaces in isotropic turbulence to be of cylindrical shape [25], consistent with such parabolic points found presently. The correlation, found in §3.4, between flatter surface regions and close alignment between the scalar gradient and the most compressive strain-rate eigenvector, $\boldsymbol{\gamma}$, emerges shortly after the ad-hoc spherical initialization, weakening later in the structure lifetime. This correlation can be observed in the joint and marginal distribution of averaged alignment conditioned on C shown in fig. 17.

Mean trajectories of primary structures in STI with $M = 1.5$ differ from those in DHIT due to the open structure evolution close to the inlet and the impact of the shock on the geometrical and physical surface properties (fig. 16a). The exclusion of the final steps of the lifetime for lack of statistical significance prevents the mean $\phi_{4\lambda}$ trajectory from reaching values of the scalar gradient and vorticity magnitudes as low as in the trajectories of ϕ_{λ} and $\phi_{2\lambda}$ structures. Whereas the increase in scalar gradient magnitude depends on the size of the primary structures, the increase of the vorticity magnitude is the same for all structure sizes.

The stronger compression and quicker closure of incoming structures in the STI-M3 configuration change the ensemble mean trajectories in terms of geometrical and physical structure properties compared to the lower Mach number case (fig. 16b). The smaller the initial size of the structures, the lower their curvedness is at the point of highest scalar dissipation. Compared to the DHIT (fig. 15), $\phi_{4\lambda}$ structures reach significantly higher average scalar dissipation, and at lower curvedness resulting from the flattening of the surfaces normal to the shock. Considering the evolution after the peak in scalar gradient magnitude, the curvedness of the ϕ_{λ} and $\phi_{2\lambda}$ structures decays in DHIT, is nearly constant for STI with $M = 1.5$, and has a period of increase for the STI with $M = 3.0$. Since the pile-up process of $\phi_{4\lambda}$ structures farther downstream of the shock generates structures of large streamwise extent, the scalar gradient and vorticity magnitude do not evolve toward the low values observed for smaller (ϕ_{λ}, $\phi_{2\lambda}$) structures in the final stage of their ensemble mean trajectories.

The average alignment between scalar gradient and the most compressive strain-rate eigenvector conditioned on S and C at highlighted steps of the closest-to-mean trajectories (fig. 17) emphasizes again the found correlation between flatter surface regions and high $\nabla\phi$-$\boldsymbol{\gamma}$ alignment for both initial structure sizes.

4 Application to compressible turbulent mixing layers

The second half of the project focused on the study of compressible turbulent mixing layers. See figure 18a for a schematic of the simulations setup and and figure 18b for a representative snapshot

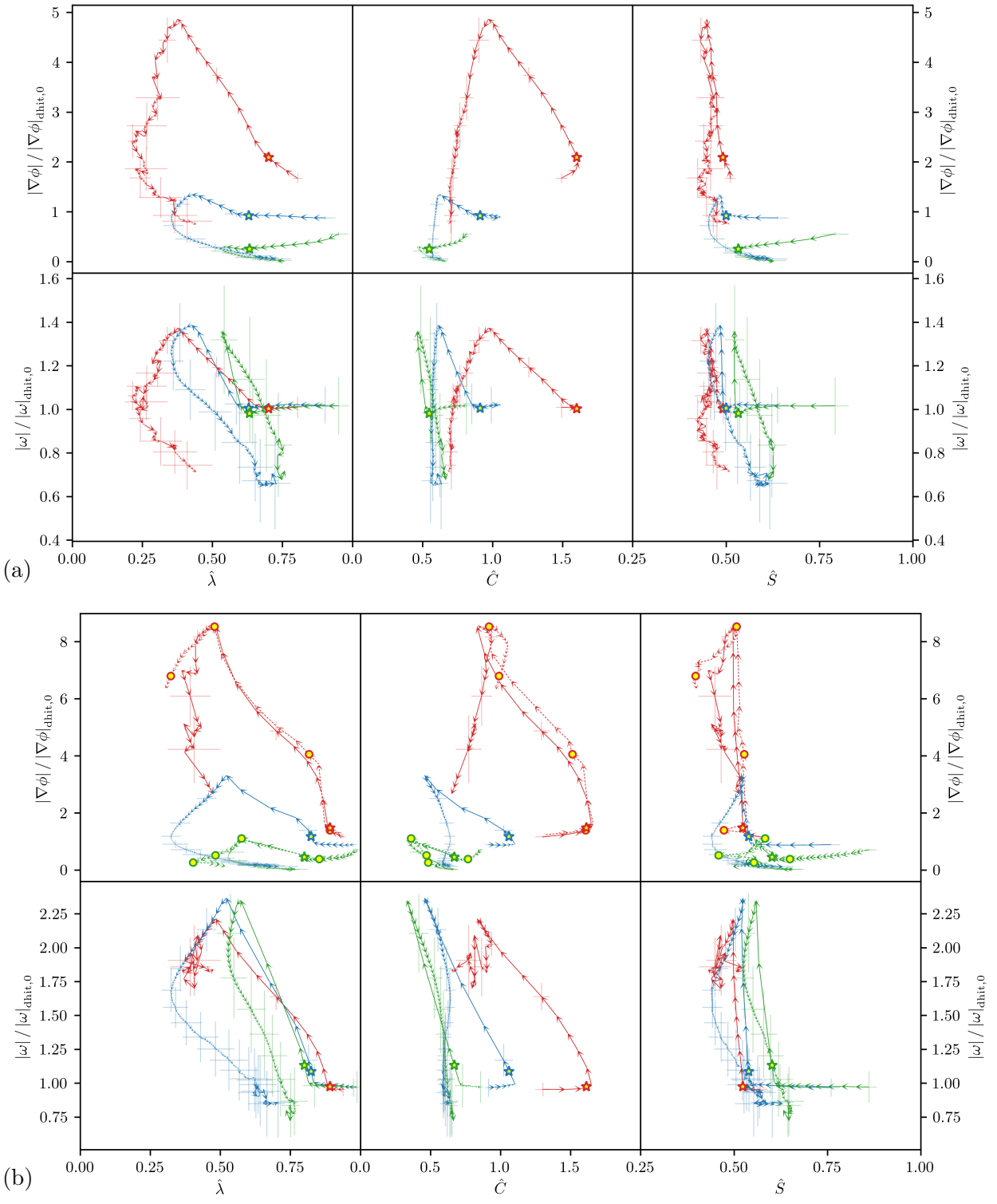

Figure 16: Ensemble mean trajectories of primary structures of ϕ_λ (green), $\phi_{2\lambda}$ (blue), and $\phi_{4\lambda}$ (red) for STI with $M = 1.5$ (a) and $M = 3.0$ (b) in the $(\hat{S}, \hat{C}, \hat{\lambda})$ geometric space with normalized scalar gradient and vorticity magnitude (top and bottom rows in a and b). The yellow star marks the mean shock-crossing tracking step. For ϕ_λ and $\phi_{4\lambda}$ structures in STI-M3, the individual closest-to-mean trajectory (dotted) is plotted with highlighted steps (yellow circles) corresponding to the structures rendered in fig. 17. Other plot elements are the same as in fig. 15.

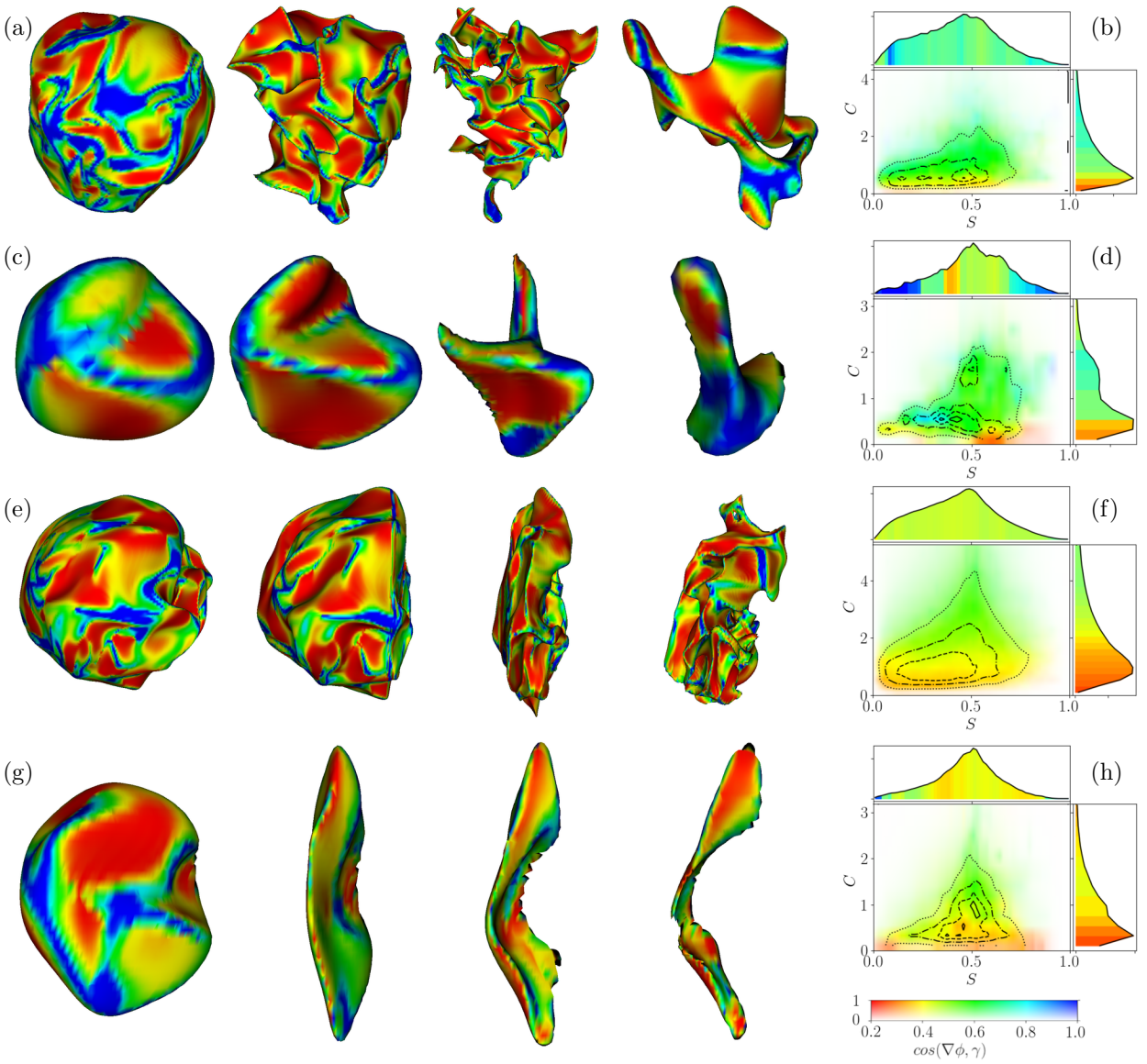

Figure 17: Renderings of primary $\phi_{4\lambda}$ (a) and ϕ_{λ} (c) structures in DHIT, and STI-M3 (e and g, respectively, for $\phi_{4\lambda}$ and ϕ_{λ}) with the alignment between scalar gradient and the $\boldsymbol{\gamma}$ eigenvector of the strain-rate tensor mapped onto each surface. Each horizontal sequence corresponds to the highlighted steps of the closest-to-mean trajectories shown in fig. 15 (time increasing from left to right, with scale varying between frames). The corresponding distribution of average alignment of scalar gradient and $\boldsymbol{\gamma}$ conditioned on S and C (hue), accounting for the area-based joint PDF (saturation) is shown for the last rendered structure of each sequence in (b,d,f,h). See also fig. 9 for a detailed explanation of these plots.

Table 3: Grid properties of the mixing layer configuration for different convective Mach number M_c simulation cases. The domain extent is normalized by the initial momentum layer thickness.

M_c	$\tilde{L}_x \times \tilde{L}_y \times \tilde{L}_z$	$N_x \times N_y \times N_z$	$\tilde{L}_{y,\text{core}}$	$N_{y,\text{core}}$
0.3	$345 \times 560 \times 86$	$1024 \times 1127 \times 256$	299.7	908
0.7	$345 \times 480 \times 86$	$1024 \times 973 \times 256$	253.5	768
1.1	$345 \times 400 \times 86$	$1024 \times 931 \times 256$	253.5	768

of the simulations. The specifications for these simulations are provided in table 3.

Prior experiments and simulations have shown that compressibility significantly inhibits the growth rate of mixing layers [28, 29, 30]. Temporally- and spatially-developing canonical mixing layers have previously been studied, focusing on the dynamics of large, organized flow structures [31], the process of transition to turbulence and the self-similar state of the shear layer [32, 33]. From perturbed laminar initial (or inlet) conditions the flow develops to a turbulent, self-similar state via a Kelvin-Helmholtz instability [34, 35]. During the transition to turbulence the occurrence of different structures, such as rollers and rib vortices [36, 37] and Λ-vortices, harpin-vortices and "flower" structures [38] has been observed. The dynamics of these structures are sensitive to initial/inlet conditions. Statistical features of the turbulence in its self-similar state, such as the longitudinal velocity structure functions and scaling exponents, follow the observations for homogeneous isotropic turbulence for small scales, but differ from those for the larger scales [39].

The main objective of our study of compressible mixing layers initiated in Y2 was to elucidate how the phenomenology of a decreased growth rate of mixing layers with increased compressibilty can be explained from the standpoint of turbulence structures. To gain insight into these structural mechanisms, our previously developed geometrical analysis and flow-feature tracking methods are applied to the vortical structures extracted as isosurfaces of the Q-criterion field from the numerical datasets of different mixing layers, varying the convective Mach number (M_c). Despite the introduction of the hairpin vortex concept by Theodorsen in the 1950s, the occurrence, persistence and significance of such vortices in shear flow configurations is still subject of debate. Therefore, our analysis places additional interest on the evolution of hairpin-like vortices in the mixing layers, by developing targeted identification methods for such flow features and their temporal evolution (see, figure 19).

4.1 Findings of application of structure tracking

Following the configuration setup of a temporally developing mixing layer by [40] and [41], we conducted direct numerical simulations for convective Mach numbers $M_c = 0.3$, 0.7, and 1.1 at higher spatial resolution than in previous studies, followed by a geometric characterization and temporal tracking of the resulting turbulent structures. The flow is initialized such that the mean streamwise velocity component is prescribed by a hyperbolic tangent profile, while the cross-stream and spanwise mean velocity components are set to zero.

$$\bar{u}_1 = \frac{\Delta U}{2} \tanh\left(-\frac{y}{2\delta_{\theta,0}}\right), \qquad \bar{u}_2 = 0, \qquad \bar{u}_3 = 0 \tag{11}$$

Pressure and density are initially uniform across the domain. The vorticity and momentum thickness Reynolds number have initial values of $Re_{\omega,0} = 640$ and $Re_{\theta,0} = 160$. The initial vorticity

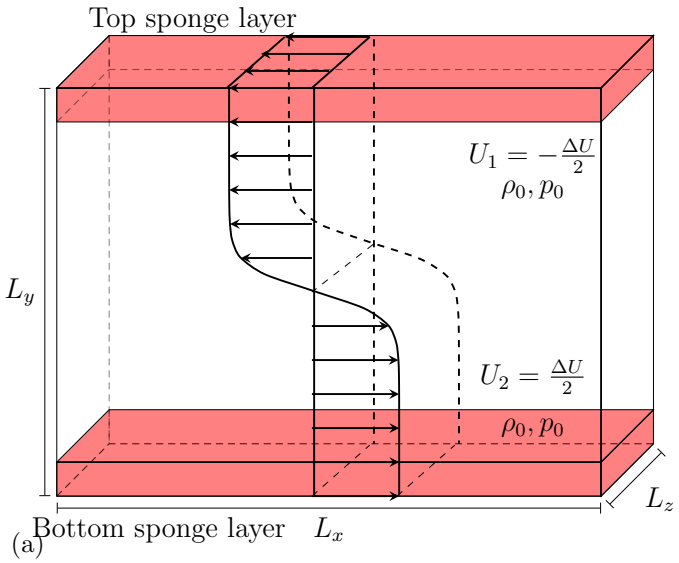

(a)

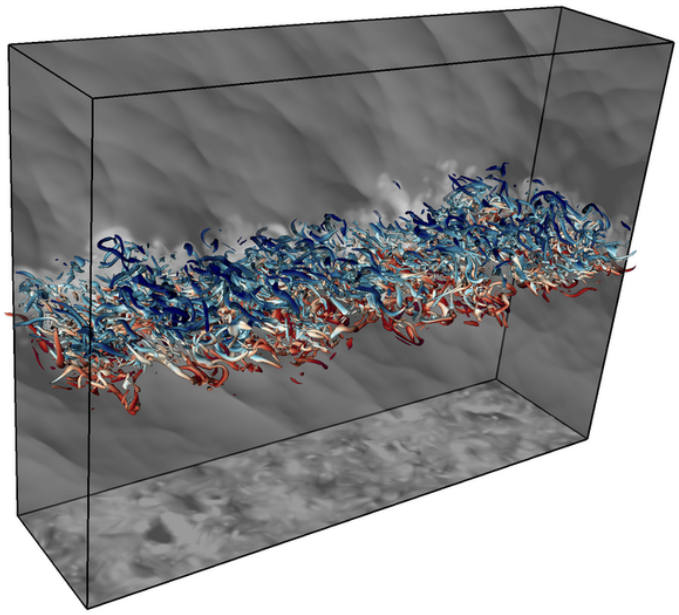

(b)

Figure 18: (a)Illustration of the initial condition of the temporally developing mixing layer. Mean streamwise velocity profile and sponge boundary damping indicated in red.(b) The $M_c = 1.1$ mixing layer at the beginning of its self-similar regime ($\tau = 650$). Planes with reduced opacity show the density field (white: $\rho = 0.7$, black: $\rho = 1.1$) where the center plane is artificially displaced to the bottom for visibility.Vortical structures are identified as iso-surfaces of the Q-criterion and colored by the streamwise velocity component (blue: $u_1 = -1.0$,red: $u_1 = 1.0$).

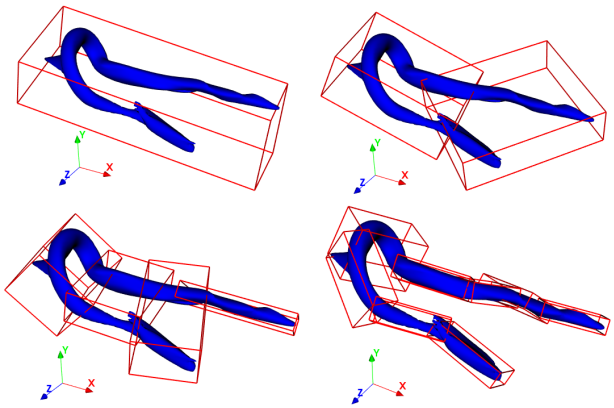

Figure 19: A hairpin vortex (blue) extracted from the $M_c = 1.1$ mixing layer at $\tau = 196$ and its oriented bounding box (OBB) tree representation (red) of increasing depth from left to right. To capture the bent shape of the structure, the level of the tree needs to be sufficiently high.

thickness is specified to be $\delta_{\omega,0} = 1$, while the momentum thickness is $\delta_{\theta,0} = 0.25$ initially. To trigger the transition to turbulence broadband fluctuations are added to the mean velocity components. Those fluctuations are obtained from a random field on which a isotropic turbulence spectrum [42] is imposed as

$$E(k) \propto k^4 e^{-2k^2/k_0^2} \tag{12}$$

with $k_0 = 48$. Applying this initialization technique leads to a nonzero compressible velocity component derived based on a small turbulence Mach number expansion of the Navier–Stokes equations. Additionally, (incompressible) fluctuations of the pressure field and linearly-related density and temperature fluctuations are also present initially. To limit the velocity fluctuation to the center region of the domain a damping cross-stream function is applied in the form of a hyperbolic secant shape following [43].

$$f(y) = C \operatorname{sech}^2\left(\frac{y}{2\delta_{\theta,0}}\right) \tag{13}$$

with $C = 0.25$. The velocity components are initialized as $u_i = \bar{u}_i + f(y)u_i'$.

A validation effort of the conducted DNS was first pursued in Y2. The temporal development of the mixing layer configuration of $M_c = 0.7$ is visualized in figure 20 by means of the density distribution on the $z = 0$ plane spanning in streamwise (x) and cross-stream (y) direction. Due to friction between the two streams the temperature rises in the mixing layer, which results in a decrease of density as the overall pressure is nearly constant. Local pressure minima associated with vortices and acoustic waves emanating from the mixing layer are hinted in the density visualization. Self-similar solutions can be derived for the equations and boundary conditions governing a turbulent mixing layer of sufficiently high Reynolds number [44]. The time necessary to reach the self-similar state is influenced by the choice of method and its perturbation strength used to generate initial random fluctuation in the flow field. The requirements for the mixing layer to be in the self-similar state are 1) a linear thickness growth and the independence of the shapes of the mean velocity, and 2) Reynolds stress profiles of time (or downstream distance in spatial developing layers) when scaled by the velocity difference and local mixing layer thickness [45]. These three indications of a self-similar period in the mixing layer evolution are validated in this study for the three considered simulation cases.

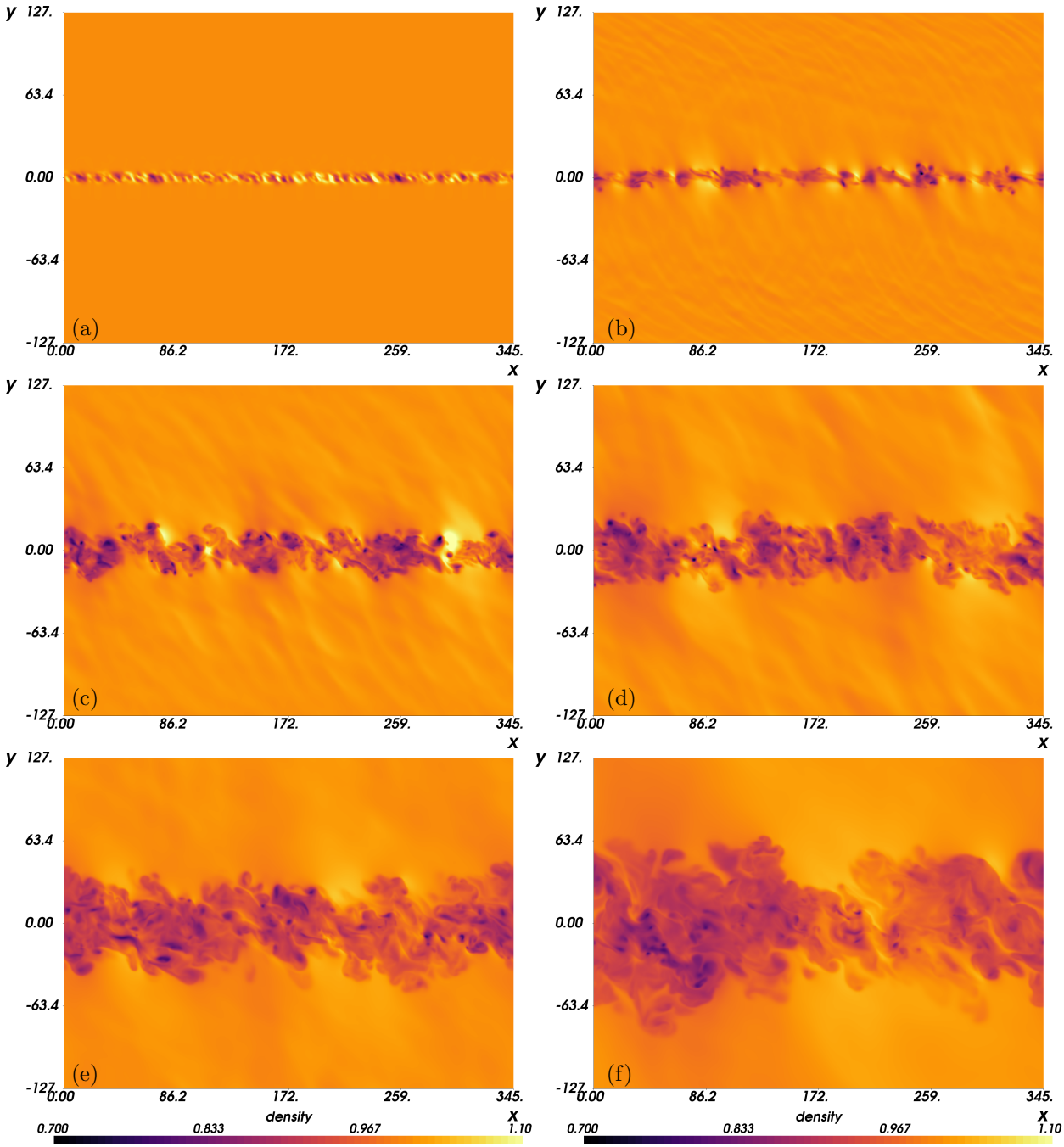

Figure 20: Density xy-planes of the $M_c = 0.7$ mixing layer configuration at different times: (a) $\tau = 4$, (b) $\tau = 200$, (c) $\tau = 400$, (d) $\tau = 600$, (e) $\tau = 1000$, (f) $\tau = 1800$. Frames (c)-(e) roughly fall within the self-similar regime of the mixing layer $\tau = 500 - 960$. The figure is limited to the transversal core region of the domain, see table 3.

Table 4: Start $\tau_{ss,s}$ and end $\tau_{ss,e}$ time of the self-similar regime for different convective Mach number M_c. $\dot{\delta}_{\theta,ss}$ denotes the slope of the linear regression conducted in the self-similar regime.

M_c	$\tau_{ss,s}$	$\tau_{ss,e}$	$\dot{\delta}_{\theta,ss}$
0.3	350	700	0.01308
0.7	500	950	0.009572
1.1	650	1050	0.008739

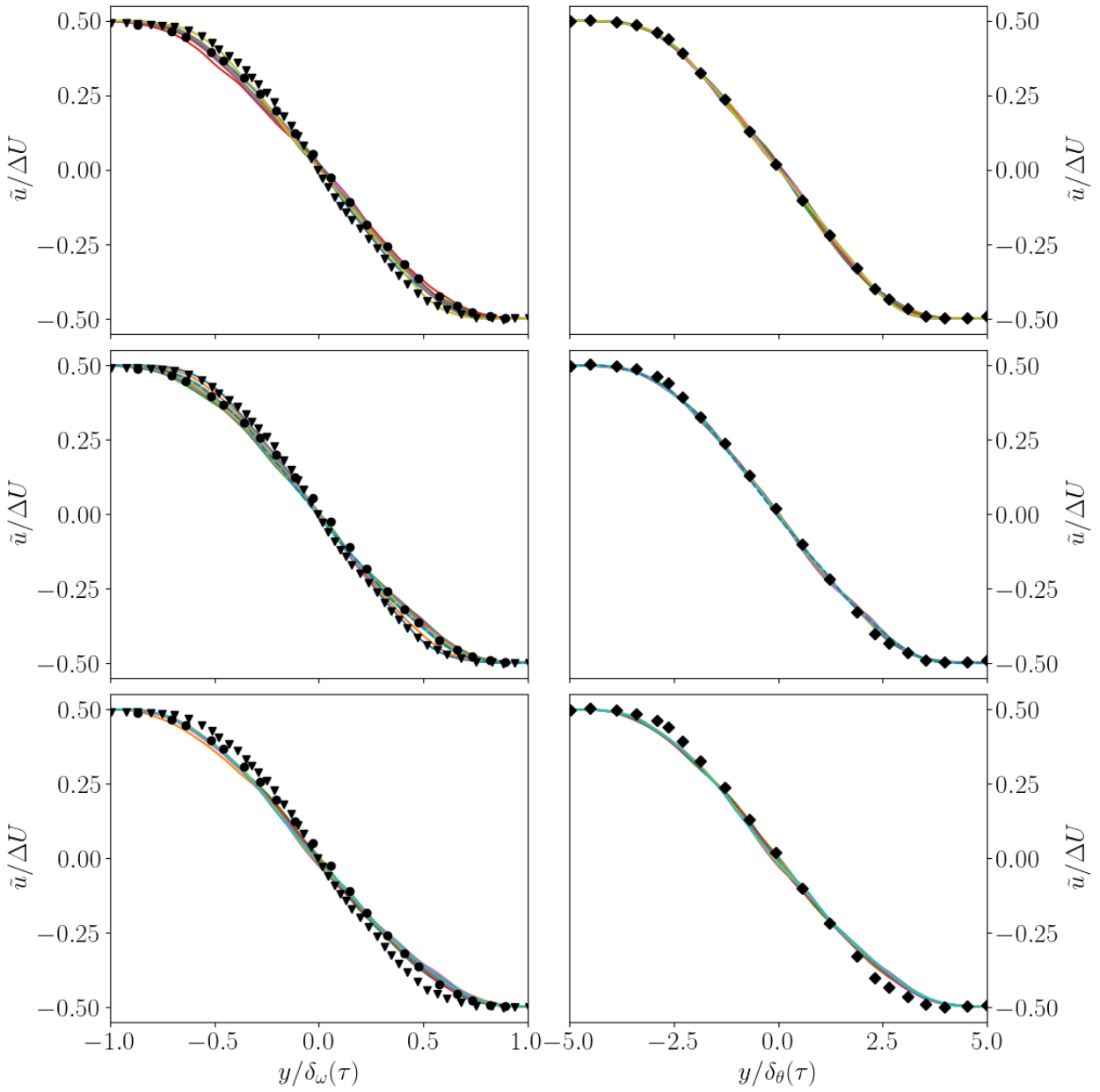

Figure 21: Self-similar streamwise velocity profiles for $M_c = 0.3$ (top),$M_c = 0.7$ (center) and $M_c = 1.1$ (bottom). Time interval between profiles $\Delta\tau \approx 40$ in order: —,—, —, —, —, —,—, —, —, —, - -, - -. Reference data by [46] (●), [40] (▼) and [35] (◆) for the (quasi-)incompressible mixing layer.

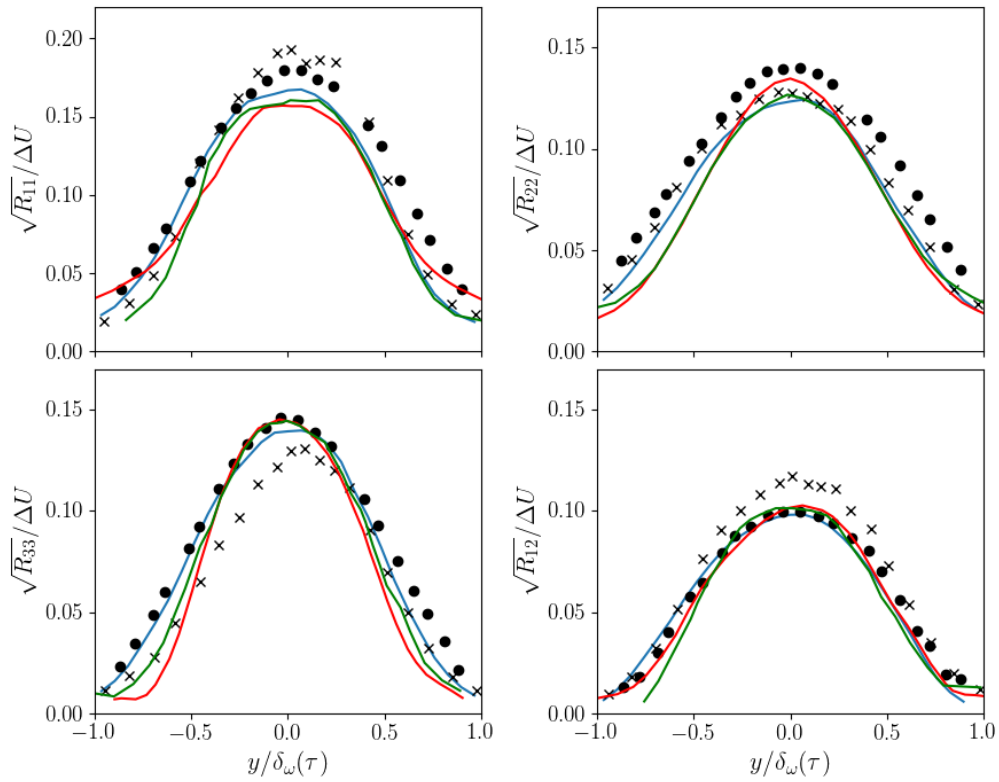

Figure 22: Ensemble mean profile of streamwise, cross-stream and spanwise turbulence intensities and Reynolds shear stress for $M_c = 0.3$: Present DNS (—), Pantano & Sarkar (2002, —), Rogers & Moser (1994, —), Bell & Mehta (1990, ●) and Spencer & Jones (1971, ×).

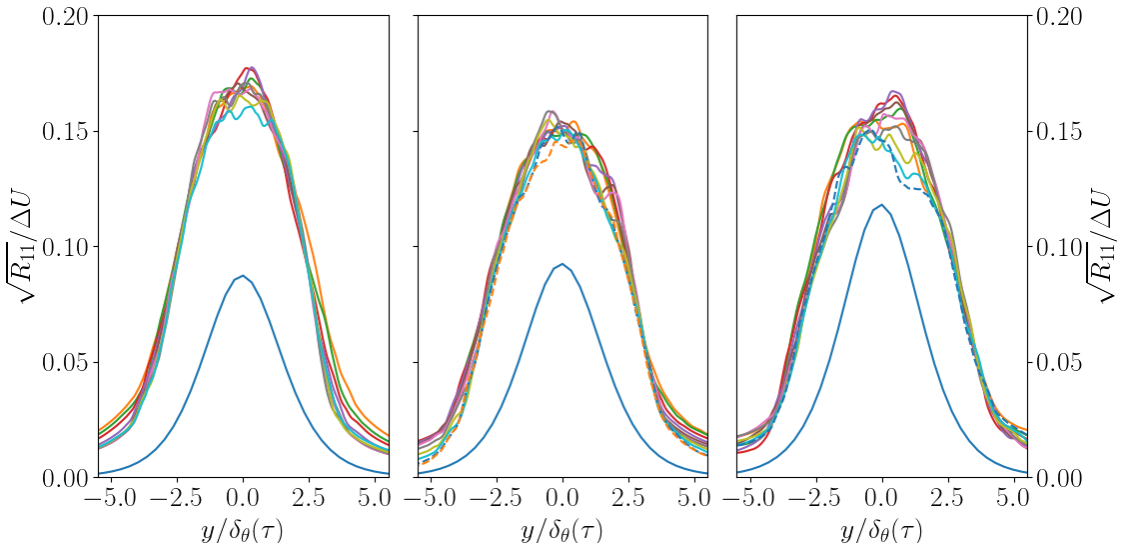

Figure 23: Instantaneous cross-stream (y) profiles of streamwise turbulence intensity for the $M_c = 0.3$ (right), $M_c = 0.7$ (center), and $M_c = 1.1$ (left) cases just after initialization (—) and in the self-similar periods: $\tau = 360 - 680, \tau = 521 - 922, \tau - = 680 - 1040$ for $M_c = 0.3, 0.7, 1.1$. Time interval between profiles $\Delta\tau \approx 40$ in order: —, —, —, —, —, —, —, —, —, - -, - -. Each profile is spatially averaged in the homogenous directions (x and z).

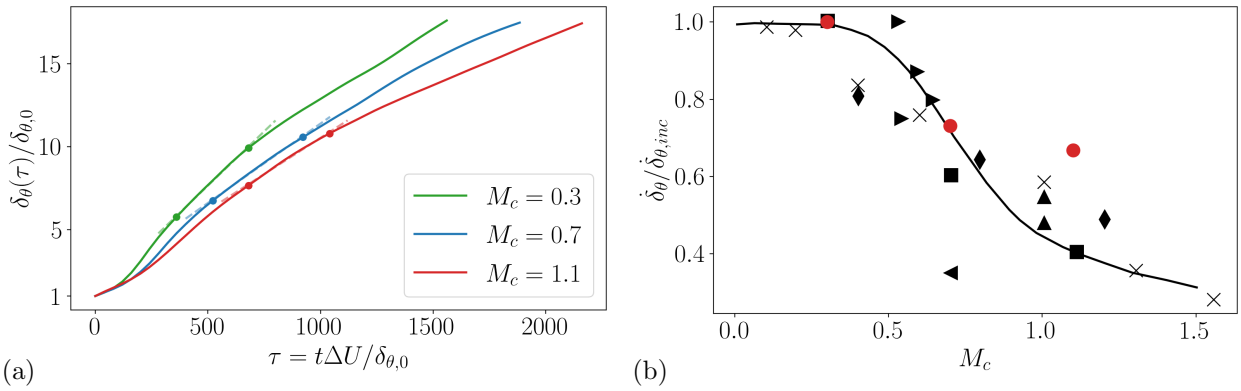

Figure 24: (a) Temporal evolution of the momentum thickness for different convective Mach numbers M_c. Markers indicate evolution interval used for the linear regression in the self-similar period. (b) Mixing layer growth rate in self-similar period for present simulations (●) and references: 'Langley curve' by [47] (—), [48] (▲), [49] (×), [50] (▶) [51] (◆), [40] (■), [38](◀).

The growth of the mixing layer, expressed in terms of momentum thickness, is shown in figure 24a. A period of linear growth can be found in all three momentum thickness evolutions as indicated by the linear regression of high correlation coefficient in this period. With increasing convective Mach number a longer time of transition is observed until the mixing layer reaches its period of linear growth. Again indicative of turbulence inhibitions by higher M_c, the momentum thickness growth rate

$$\dot{\delta}_\theta = \frac{1}{\Delta U}\frac{\mathrm{d}\delta_\theta}{\mathrm{d}t} = \frac{1}{\delta_{\theta,0}}\frac{\mathrm{d}\delta_\theta}{\mathrm{d}\tau} \tag{14}$$

in the self-similar period, $\dot{\delta}_{\theta,ss}$, is lower for higher M_c (see table 4).

To investigate the temporal mixing layer configuration, described earlier in this report, from a structural viewpoint, the present analysis focuses on the inhibiting effect of compressibility, expressed as a set of convective Mach numbers $M_c = \{0.3, 0.7, 1.1\}$, on the evolution and geometrical properties of vortical structures in the mixing layer. As the vortex identification method, the compressible version of the Q-criterion originally introduced by [52] is utilized. Like the Δ-criterion by [53, 54, 55], λ_2-criterion by [56] or the λ_{ci}-swirl-strength criterion by [57, 58], the Q-criterion identifies vortices based on the velocity gradient tensor $\mathbf{A}_{ij} = \partial V_i/\partial x_j$. Comprehensive reviews of vortex identification methods can be found in [59] and [60]. To summarize the motivation of the Q-criterion, the characteristic polynomial of the velocity gradient tensor $\det\left(\mathbf{A}_{ij} - \lambda\mathbf{I}\right) = 0$, which can be formulated as

$$\lambda^3 + \mathbf{P}\lambda^2 + \mathbf{Q}\lambda + \mathbf{R} = 0 \tag{15}$$

is considered. Here $\mathbf{I}$ is the identity matrix and λ are the eigenvalues of the velocity gradient tensor. The tensor's invariants P, Q and R can be expressed as [61, 59]

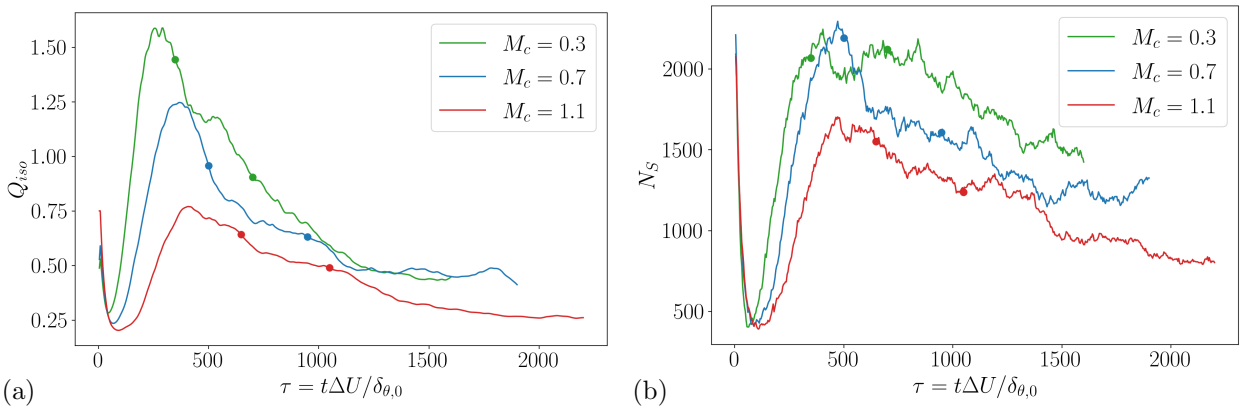

Figure 25: (a) Evolution of the iso-contour value Q_{iso} used to extract individual Q structures from the mixing layers of varying convective Mach number M_c. (b) Number of extracted structures based on the iso-value evolution. The yellow marker indicate the begin and end of the self-similar regimes of the mixing layers.

$$\mathbf{P} = -tr[\mathbf{A}] = -\mathbf{S}_{ii} \tag{16}$$

$$\mathbf{Q} = \frac{1}{2}\left(\mathbf{P}^2 - tr[\mathbf{A}^2]\right) = \frac{1}{2}\left(\mathbf{P}^2 - \mathbf{S}_{ij}\mathbf{S}_{ji} - \mathbf{\Omega}_{ij}\mathbf{\Omega}_{ji}\right) \tag{17}$$

$$\mathbf{R} = \frac{1}{3}\left(-\mathbf{P}^3 + 3\mathbf{PQ} - tr[\mathbf{A}^3]\right) \tag{18}$$

$$= \frac{1}{3}\left(-\mathbf{P}^3 + 3\mathbf{PQ} - \mathbf{S}_{ij}\mathbf{S}_{jk}\mathbf{S}_{ki} - 3\mathbf{\Omega}_{ij}\mathbf{\Omega}_{jk}\mathbf{S}_{ki}\right) \tag{19}$$

where $\mathbf{\Omega}_{ij} = 1/2(\mathbf{A}_{ij} - \mathbf{A}_{ji})$ is the rotation-rate tensor and $\mathbf{S}_{ij} = 1/2(\mathbf{A}_{ij} + \mathbf{A}_{ji})$ is the strain-rate tensor. These two tensorial quantities are defined as the antisymmetric and symmetric part of the velocity gradient tensor $\mathbf{A}_{ij}$. The Q-criterion defines a vortex as a region where $Q > Q_{\text{iso}}$, where nominally $Q_{\text{iso}} > 0$. In incompressible flow, this condition is satisfied where the vorticity magnitude is larger than magnitude of rate of strain.

The Q-structures of interest are obtained by iso-contouring the Q scalar field. Due to the threshold-based character of the Q-criterion, the choice of the iso-contour value Q_{iso} is crucial for the shape, spatial extent and number of Q-structures extracted from the flow field at an instant. A low iso-value generates large, widely ramified structures not suitable for the tracking of individual structures, while a high iso-value shrinks the extracted Q-structures reducing their complexity and lifetime. To account for the temporally evolving character of the flow field, a time-dependent iso-value is chosen: From the mean, $\langle Q \rangle$, and standard deviation, $\sqrt{\langle Q^2 \rangle - \langle Q \rangle^2}$, of the scalar Q field of each frame the iso-value used for extraction is formed as $Q_{\text{iso}} = \langle Q \rangle + n\sqrt{\langle Q^2 \rangle - \langle Q \rangle^2}$. Here, the standard deviation is found to be the dominant contribution to Q_{iso}. For the lower convective Mach number case ($M_c = 0.3$), a choice of $n = 6.0$ was found to extract a satisfactory number of individual Q structures throughout the simulation and mainly structures of tube-like shape in the self-similar regime and later stages of the simulation. Due to the inhibiting effect of compressibility on the turbulence intensities in the mixing layer, the lower Mach number case is the most prone to formation of large, ramified Q structures. Therefore, a lower choice for n would still avoid largely connected structures for the higher Mach number cases. However, for the sake of consistency and to limit the number of parameter influencing the study, the same choice of $n = 6.0$

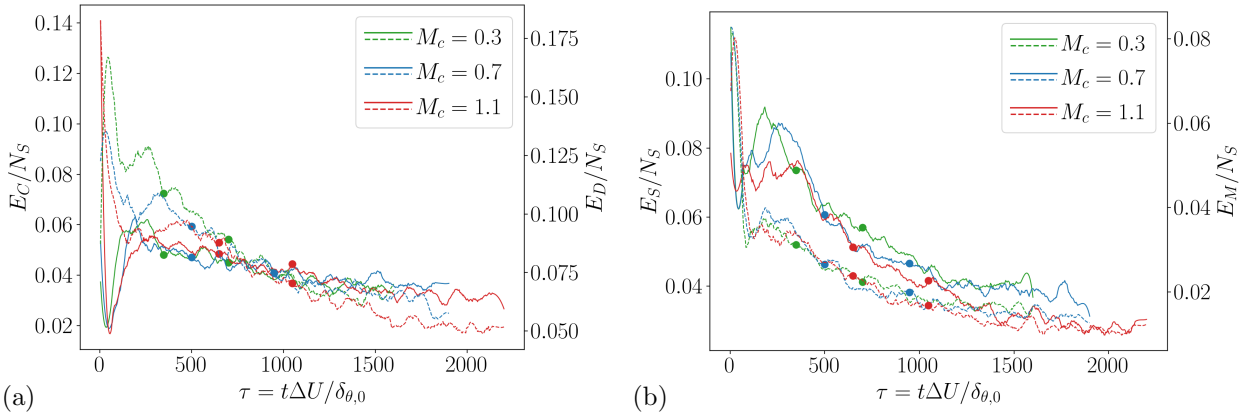

Figure 26: Smoothed number of detected events of different types over time: (a) Creations (solid), disappearances (dashed), (b) splits (solid) and merger (dashed) of any order.

is made for $M_c = 0.7, 1.1$. Note that, despite the same choice of n, at a given time instant the iso-value Q_{iso} tends to be lower for the higher Mach number, as the standard deviation of the Q field is lower, see figure 25a. After an initial transient, which is longer for larger M_c, the iso-value reaches its maximum before the beginning of the self-similar regime for all considered Mach number M_c and decays afterwards. Indicative of the expression of turbulence inhibition on the structural level, a larger number of structures is extracted throughout the simulation for lower Mach number, figure 25b. Similar to the iso-value evolution, a transient is present in the number of extracted structures and the temporal distribution of detected event types, figure 26. Based on the applied iso-contouring and extraction method, the number of structures decays in the self-similar regime for $M_c = \{0.7, 1.1\}$ and only in the $M_c = 0.3$ case the number of extracted structures remains constant throughout the self-similar regime of the mixing layer. The peak event activity coincides with the peak in extracted structures (and iso-value) and is ordered by Mach number. The number of merger exceeds the number of split events only in the very early stage of the simulation.

The extracted vortical structures in the mixing layer are then individually tracked by applying the flow feature tracking methodology described earlier in this project report (and also published in [62]). To increase the performance of the tracking algorithm, in the *oriented bounding box (OBB) distance constraint*, an OBB-tree representation of varying depth, figure 19, is used rather than always using the root node of the tree to represent the structures in the GJK-distance calculation. Benefiting from an improved surface representation, the distances between the leaf nodes of a source-target correspondence pair are calculated and more false correspondences are rejected in the *OBB distance constraint*, which otherwise would be rejected by the computationally more expansive *surface proximity constraint*. If a distance between leaf nodes satisfies the constraint, computation of all other (not yet determined) distances is skipped. The level of the OBB tree used to represent a structure is based on the compactness parameter $\hat{\lambda}$ and the absolute shape index $\hat{S}$: Larger stretching and an increased number of hyperbolic surface points are used as indicators that a higher level of the tree is needed to capture the bent surface shape correctly.

The initialized velocity fluctuations generate small, rather compact ($\hat{\lambda} > 0.6$) Q-structures in the very first frames of the simulations. While these structures grow and merge with others, they become more stretched shortly after initialization ($\tau < 40$ for $M_c = 0.3$), see figure 27. The continued merging process ($\tau = 40$-120 for $M_c = 0.3$) leads to the formation of large structures characterized by a low value of compactness and more elliptical than hyperbolical surface points

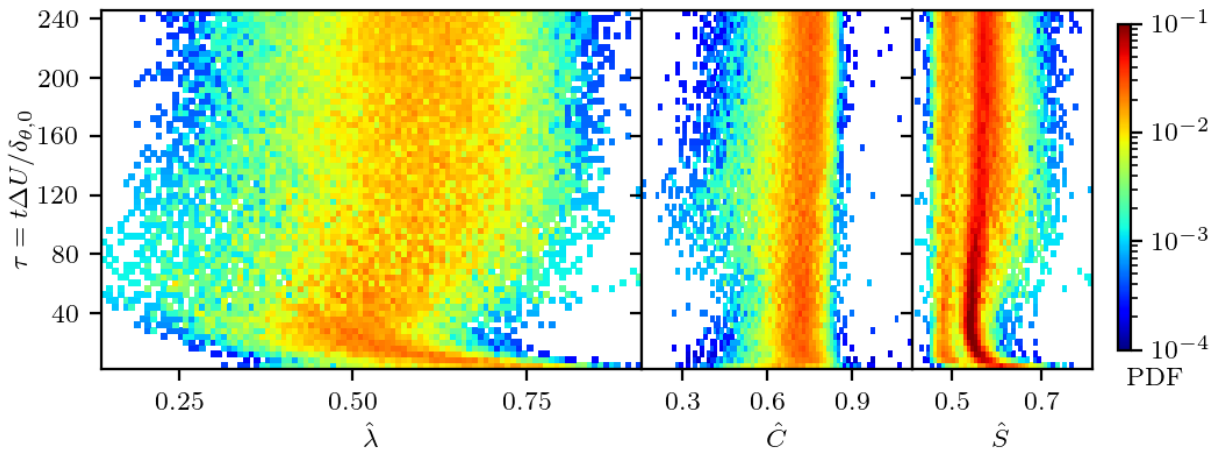

Figure 27: Temporal evolution of the geometrical signature of all structures extracted during the early, pre-self-similar stage ($\tau = 0$ - 240) of the $M_c = 0.3$ mixing layer configuration. Each sample is weighted by the inverse of the total number of structures of the frame from which the sample is extracted.

($\hat{S} > 0.5$). These largely connected (ramified) structures are reminiscent of Λ-vortices observed near the inlet of spatially developing mixing layers [38]. As the structures span across the center plane of the mixing layer, they split into smaller, less ramified structures shortly after, when parts of the structures are pulled into the oppositely directed free streams.

Another indicator of the inhibiting effect of compressibilty on the turbulent dynamics of the mixing layer can be seen in the statistics of the (anti-)alignment between the normal vector of the Q-isosurfaces and the vorticity vector, figure 28(a), as it takes longer for the vorticity to become approximately tangential to the surfaces after initialization.

Consistent with the Reynolds stress profiles, see figure 23 and 22, the majority of new vortices is created near the center plane of the mixing layer, figure 28(b), where the cross-stream location of a structure is defined as the mean of the maximal and minimal cross-stream coordinate of the structure's surface points. Less new vortices are created per frame of the self-similar regime with increasing convective Mach number M_c.

The geometrical variety of the Q-structures extracted during the self-similar regimes of the mixing layers is shown in figure 29. The majority of the structures is characterized by a tube-like shape of decreasing curvedness with increasing convective Mach number M_c. The tube-like structures show a large variation in stretching, which decreases with decreasing curvedness.

Newly created Q-structures in the self-similar regime of the $M_c = 0.3$ mixing layer are geometrically characterized as generally of tube-like shape with a relatively higher compactness $\hat{\lambda}$, figure 30. A large portion of the newly created structures disappears below the iso-value Q_{iso} used for surface extraction in the particular frame within a few tracking time steps and without any interaction with other structures. Contrary to these short-lived, isolated structures, other structures participate in structure interactions shortly after their creations. Therefore, this section focuses on the first event (other than continuation and disappearance) in the lifetime of newly created structures. Compound events rarely occur as such (at least in the self-similar regime) and created structures mainly have merge or split events as their first structure interaction. Presented in figure 30, created structures that are the source of a split in their first event typically live longer than merging newly created structures and become more stretched tube-like before the split occurs.

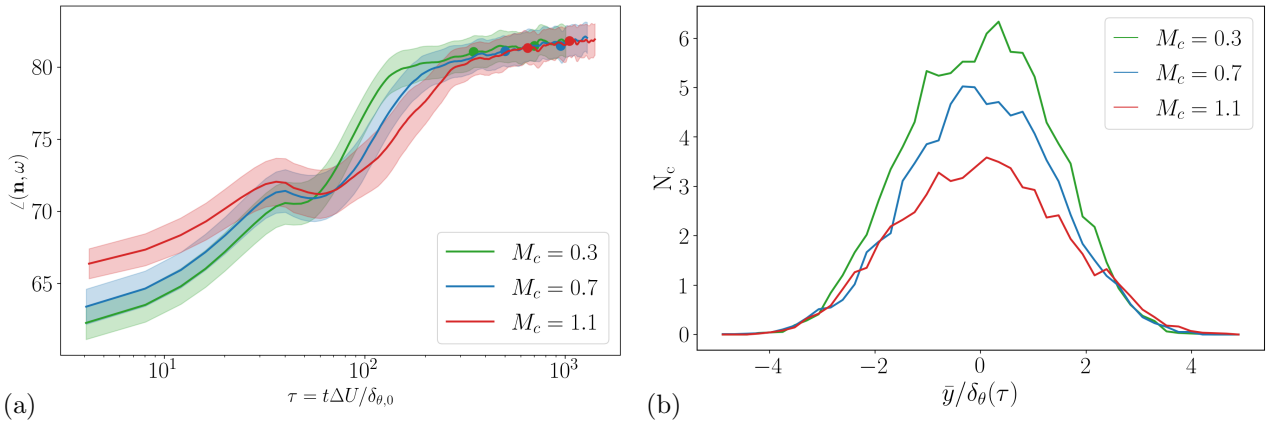

Figure 28: (a) Temporal evolution of the ensemble mean of of the surface-averaged angle between the surface normal and the vorticity on the surface. Filled area encloses two standard deviations. After an initial transient, which takes longer for increasing M_c, the vorticity becomes approximately tangential to the Q-isosurfaces. (b) Distribution of cross-stream locations of creation events during the self-similar periods of the mixing layers. Counts normalized by number of frames in the self-similar regime.

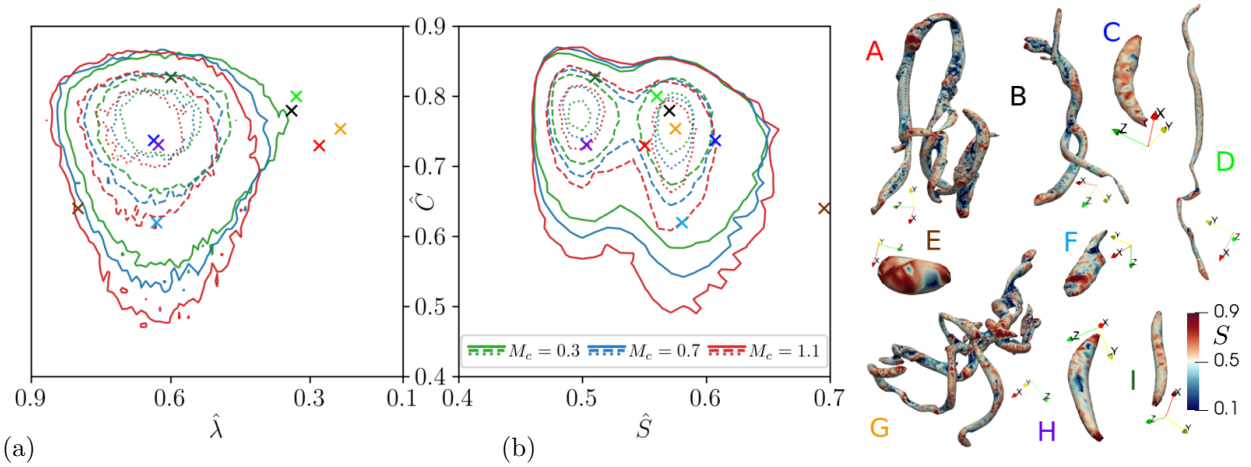

Figure 29: (a) Geometrical variety of all extracted Q-structures with more than 100 surface points in the self-similar regimes of the mixing layers for different convective Mach numbers. Contour lines of the PDF indicate 0.1 (solid), 0.4 (dashed) and 0.7 (dotted) of the maximum count. (b) Exemplary structures extracted from the $M_c = 0.3$ at $\tau = 344$ case corresponding to the letters in the feature space plot. Structures colored by absolute shape index S. Structure renderings are not to scale.

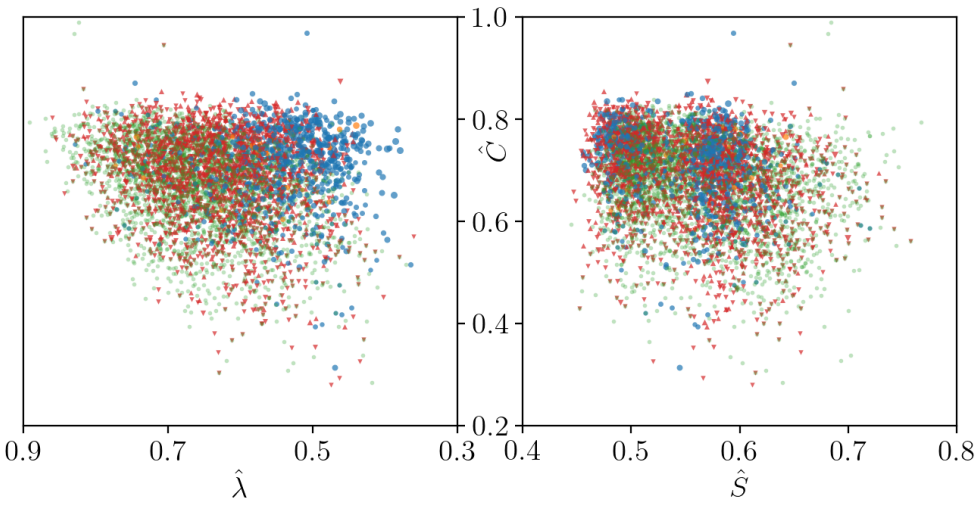

Figure 30: Newly created structures during the self-similar regime of the $M_c = 0.3$ mixing layer and their geometric signature while participating as a source in the first merge (red), split (blue) or compound(orange) event after their creation. Newly created structures which do not have any structure interaction during their (short-lived) existence are excluded from the figure. The size of the event source marker is indicative of the lifespan from the creation to the first event. For merge events, the ▼ shows a merge into another existing structure, while a ▲ marker is used if another structure merges into the newly created structure.

If the first event in the lifetime of a newly created structure is a merge, the structure either merges into another structure (i.e., the newly created structure is a non-dominant source of the merge) or the new structure continues its life after another structure merged into it. While both scenarios occur, the first one is found to be (much) more frequent. In this case, the structure is created in close proximity to an existing structure and merges into such shortly after its creation.

4.2 Detection of hairpin-like vortical structures

Considering the geometrial variety of the extracted vortical structures, see fig. 29, the conceptual model of a hairpin vortex [63, 64, 65] proposes a vortical structure of distinctive shape. While observed in other shear flow configurations, such as homogeneous shear turbulence [66, 67, 68] and mixing layers [31, 37, 34, 69, 38], hairpin vortices are frequently reported in wall-bounded turbulence [70, 71, 58, 72, 73, 74, 75, 76]. The characteristic elements of a hairpin vortex are the spanwise oriented head connecting a pair of quasi-streamwise, counterrotating vortices referred to as the legs of the hairpin [77]. The growth of hairpin vortices is related to Townsend's attached eddy hypothesis [44], which states that the size of eddies are proportional to their distance from the wall. In wall turbulence the hairpin concept offers a mechanism to generate Reynolds shear stress, low-speed streaks and to transport vorticity of the mean shear at the wall outward [73]. Conceptually, the hairpin head undergoes a (small) upward (wall-normal) motion and lies further away from the wall as the leg pair. In agreement with observations of hairpins in boundary layers, the velocity field (perturbed by smaller-scale turbulence) surrounding an individual hairpin extracted from the $M_c = 0.3$ mixing layer displays an ejection in between the legs of the hairpin, see fig. 31. The inner part of the head of such individual hairpin is dominated by hyperbolic surface points, while the outer head part and the tips of the legs are elliptical in shape.

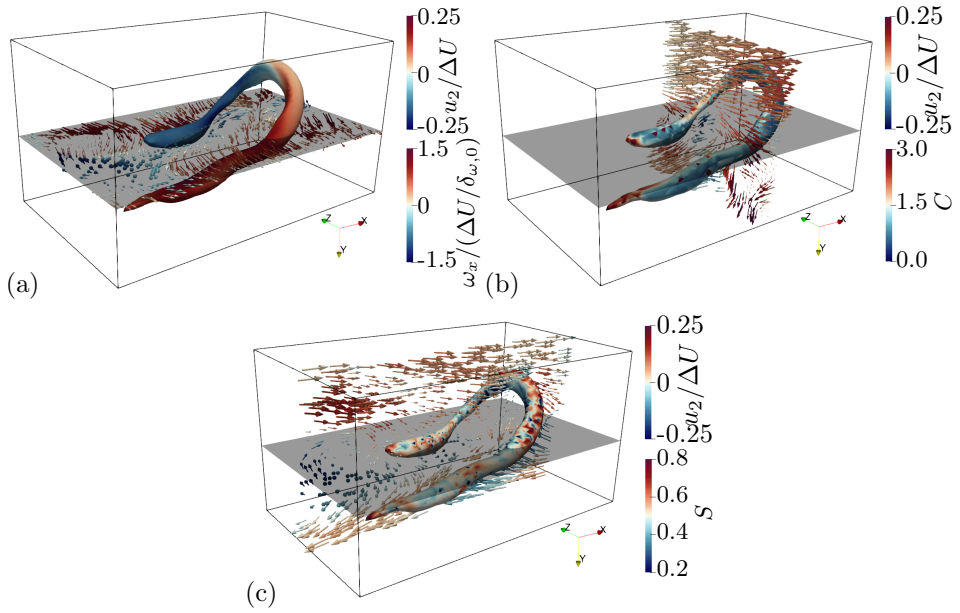

Figure 31: Plane cuts of the velocity field surrounding an individual hairpin extracted at $\tau = 144$ from the $M_c = 0.3$ mixing layer crossing its center plane indicated in grey. The velocity vector is colored by the cross-stream velocity component. Quantities mapped on the surface: Streamwise component of the vorticity (a), curvedness (b) and shape index (c).

To investigate the temporal evolution of hairpin-like vortical structures in mixing layers, an algorithm to filter hairpin-like structures from all vortical structures extracted from a turbulent flow field is proposed in the following. The goal of the algorithm is to filter individual hairpin-like structures, whereas (depending on the iso-value used for iso-surfacing) largely connected hairpins, fig. 32, are extracted from the flow field but rejected by the filter. While there is no exact mathematical definition of a hairpin vortex in the literature, hairpin-like structures are filtered by imposing a sequence of geometrical and physical constraints on each extracted vortical structure. A set of input parameters required by the algorithm is listed in table 5 with parameter values used for all applications in this work. Processing one structure at a time, the algorithm starts with an application of spectral clustering to the surface points of the structure. To identify candidates for the head and leg pair of the potentially hairpin-like structure, this spatial clustering is conducted with a prescribed number of three clusters. No scaling operation is performed prior to the spectral clustering. Structures having a spatial clustering where any of the three clusters has less than a user-defined minimum size $s_{\min}$ are rejected.

The three spatial clusters are assigned as a head candidate and two leg candidates based on the number of openings each surface cluster has: The head candidate has two openings, whereas each leg has one opening. If the clustering leads to any other combination of openings, the structure is rejected. Next, the OBB tree of each surface cluster is obtained, where the tree depth is one for a leg and two for the head to better capture its bent shape, see fig. 33. The two OBB leaf nodes of each leg are used to define the direction of the leg as the line connecting the centers of the leaf nodes and pointing away from the root node of the head candidate. The angle between the leg directions is computed and compared against a user-provided maximum angle α_{leg}. It is observed that a local coordinate system $\{\hat{x}_1^{OBB}, \hat{x}_2^{OBB}, \hat{x}_3^{OBB}\}$ based on the major, medium and minor direction of the OBB of the entire surface may lead to a poor capturing of the direction of

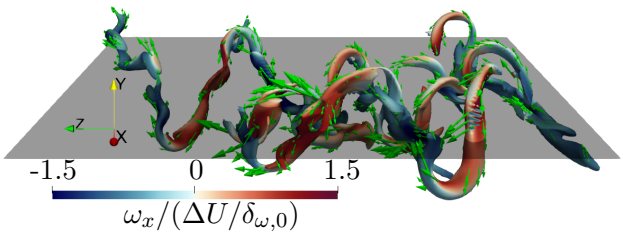

Figure 32: Large, connected hairpin vortices extracted at $\tau = 128$ from the $M_c = 0.3$ case. Streamwise vorticity component mapped on surface, while green arrows represent the vorticity at sampled surface points. Mixing layer center plane represented in grey.

Table 5: Input parameter of the hairpin filter algorithm: s_{min} minimum size of spatial clusters, α_{leg} maximum angle between the leg pair,ε maximum distance between two samples to be considered in the neighborhood of each other in the leg vorticity - cross coordinate clustering, σ minimum cluster size in the leg vorticity - cross coordinate clustering. Parameter used for the optional bimodality test of the leg cross coordinate distribution: α_{dip} significance threshold and d_{dip} interval merge distance of the UniDip algorithm.

Required				Optional	
$s_{\min}$	α_{leg}	ε	σ	α_{dip}	d_{dip}
250	$\pi/4$	0.5	150	0.05	10

the legs if the structure is rather asymmetric due to unevenly long legs for example, see fig. 33. To correct this tilt a local coordinate system is constructed as follows: From the two leg directions a mean leg direction $\vec{l}$ is obtained and projected onto the major-medium plane of the structure OBB as $\vec{l}_{\text{proj}} = \vec{l} - (\vec{l} \cdot \hat{x}_3^{OBB})\hat{x}_3^{OBB}$. A orthnormal basis $\{\tilde{x}_1, \tilde{x}_2, \tilde{x}_3\}$ is formed using the unit projected mean leg direction $\tilde{x}_1 = \hat{l}_{\text{proj}}$, the minor direction $\hat{x}_3^{OBB}$ of the structure OBB and their cross product $\tilde{x}_3$. Using this local coordinate system it is required for the head candidate to have at least one leaf node in between the legs in terms of the $\tilde{x}_3$ coordinate.

A number of extracted structures approximate a hairpin-like shape, but their leg pairs do not exhibit counter-rotating character which is essential for hairpin vortices, fig. 34a. Therefore, simple statistical constraints are imposed on the distribution of the $\tilde{x}_1$ component of the vorticity on the candidate surface: (i) The mean of the distribution on the surface cluster is required to have opposite signs for the two legs due to the counter-rotation. (ii) The absolute value the mean is expected larger than the standard deviation. To include tolerance, the coefficient of variation is required to be smaller than two. (iii) Since the vorticity changes orientation along the head, the absolute value of the mean on the head cluster is expected smaller than on both legs.

A hairpin with straight, approximately parallel legs exhibits a bimodal distribution of $\tilde{x}_3$ surface point coordinates of the leg pair, i.e., the distribution excludes the head cluster, fig. 33. To detect such bimodality the probability density function is obtained from the $\tilde{x}_3$ coordinates of the legs using a kernel density estimation (KDE) where the bandwidth is optimized by utilizing a cross-validation approach. After adding noise to this estimated PDF, random samples are obtained from the distribution and fed into the UniDip algorithm [78] to determine the modality of the distribution.

However, hairpins are often distorted by surrounding eddies. For example, if a leg is bent inwards, the distribution of the $\tilde{x}_3$ coordinates of the legs may not be bimodal. To detect those more asymmetric hairpins the bimodality is neither a necessary nor a sufficient criterion. It is kept

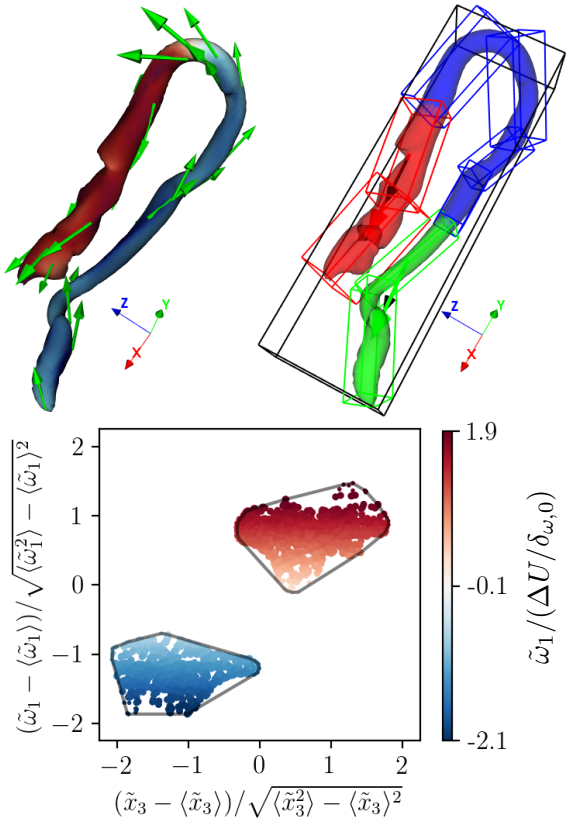

Figure 33: Elements of the hairpin detection method from left to right: Leg component of the vorticity mapped on the extracted surface. Green arrows represent the vorticity at sampled surface points. The three clusters resulting from the spatial clustering of the surface are indicated in red, green and blue. The OBB trees of each surface cluster are colored according to the cluster they enclose. A tree depth of one is used for the legs, while the depth is two for the head cluster. Red and green arrows show the direction of each leg, while black arrows are the mean leg direction projected onto the major-medium plane of the global OBB of the surface (black cuboid). Modes in the distribution of the cross coordinates of the legs are highlighted as density intervals. Probability density function obtained from the KDE of the leg cross coordinates shown in black. Histogram obtained from the samples fed into the UniDip algorithm with added noise. Convex hulls enclose the clusters obtained from the clustering of the leg component vorticity - cross coordinate clustering of the legs. Cluster core points plotted with increased point size. Scatter points colored by the leg component of the vorticity. Range of color bar based on leg vorticity component of entire surface to also apply to the surface mapping (left). Structures extracted from the $M_c = 0.3$ case at $\tau = 148$ and $\tau = 232$, respectively.

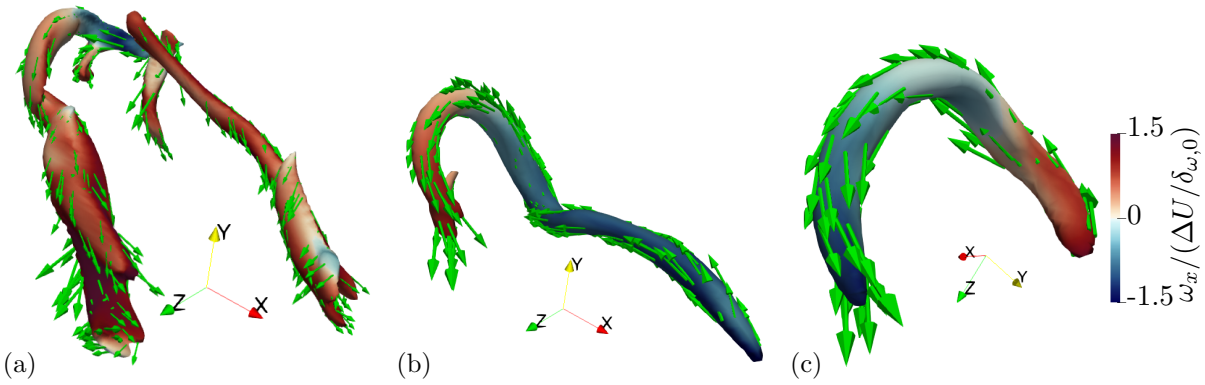

Figure 34: (a) Representative structure approximating a hairpin-like structure in shape, while differing in vorticity distribution on their surface from a hairpin vortex. Examples of hooks (b) and arches (c) detected as hairpin-like in the pre-self-similar stage of the $M_c = 0.3$ mixing layer case. The structures are detected as non-hairpin-like based on their physical dissimilarity to a hairpin vortex. Streamwise vorticity component mapped on the surfaces, while green arrows indicate the vorticity vector.

in the algorithm to optionally filter the subset of hairpins that satisfy this criterion, but not applied to obtain the results in the present work. Complementing the $\tilde{x}_3$ coordinates, the $\tilde{x}_1$ component of vorticity, $\tilde{\omega}_1$, is considered as another feature of the leg pair. The z-scores of those two features of the leg pair are obtained independently and the standardized features are clustered by applying the DBSCAN algorithm [79, 80]. In contrast to the earlier used spectral clustering, the number of clusters is not prescribed but estimated by the DBSCAN algorithm. Requiring a certain amount of compactness in $\tilde{x}_3$ and $\tilde{\omega}_1$, it is expected that each leg contributes one cluster to the data, i.e., the DBSCAN algorithm estimates two clusters in total. This approach is robust against smaller eddies which merged into the hairpin impairing not only its shape ($\tilde{x}_3$) but also its vorticity distribution due to the noise detection of the DBSCAN algorithm.

As mentioned earlier, hairpins are often lopsided and the (quasi-streamwise) legs are only rarely counter-rotating pairs of equal strength leading to asymmetry [65]. The proposed hairpin filter detects those imperfect candidates, referred to as hooks and arches in fig. 35, as hairpin-like. The number of detections of these imperfect hairpins can be greatly reduced by requiring the candidate head surface cluster to have an OBB root node center which has the utmost (smallest or largest) major coordinate $\hat{x}_1$ of the entire surface OBB compared to the OBB root node centers of the other two surface clusters.

4.3 Hairpins in the geometrical feature space

The proposed detection method, §4.2, is applied to filter hairpin-like structures from all extracted structures of the compressible mixing layers considering all frames from initialization until the end of the simulations in the post-self-similar regime. The filter settings are listed in table 5. The detected hairpin-like structures are mapped into the geometrical feature space in fig. 36a. The hairpin vortices are characterized as stretched tube-like structures. While there is a number of detections showing a balance of hyperbolic and elliptic surface points ($\hat{S} \approx 0.5$), elliptic surface points slightly dominate for most cases due to the shape of the outer head region and the tips of the legs.For the lower convective Mach number ($M_c = 0.3$) the range in geometric signature is in agreement with hairpins recently reported in stably stratified atmospheric boundary layers

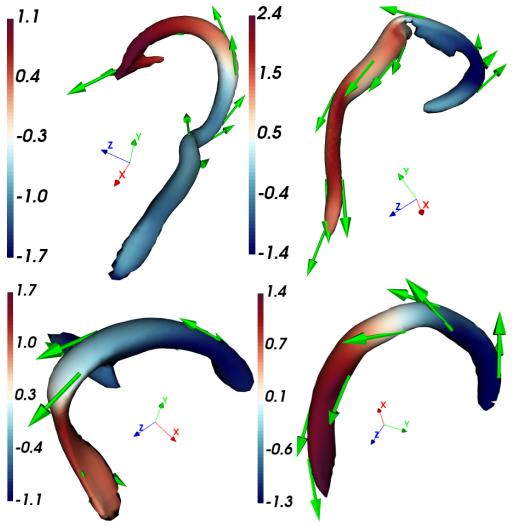

Figure 35: Examples of hooks (top row) and arches (bottom row) detected as hairpin-like in the pre-self-similar stage of the $M_c = 0.3$ mixing layer case. Other plot elements as in fig. 34a.

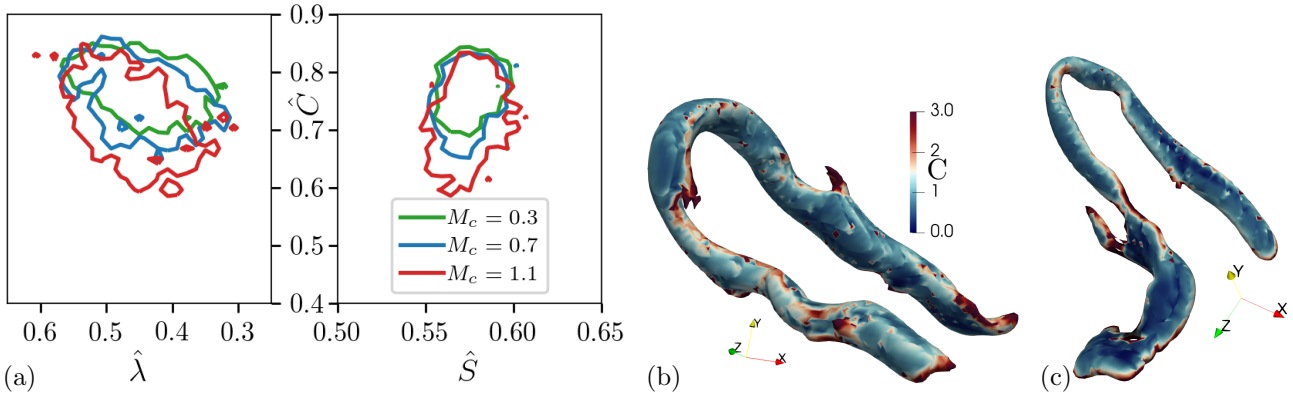

Figure 36: (a) PDF of the geometric signatures of hairpin vortices extracted from the mixing layers of varying convective Mach number M_c. Lines represent 0.3 contour level. Dimensionless curvedness mapped on hairpins extracted from the $M_c = 0.3$ ((b),$\tau = 232, \hat{C} = 0.78$) and $M_c = 1.1$ ((c),$\tau = 464, \hat{C} = 0.63$) mixing layer. For the higher convective Mach number flatter regions are found on the legs of the hairpin.

[81]. Similar to the observations regarding structures of all shapes in the self-similar regimes, see fig. 29, the curvedness of the detected hairpins decreases with increasing convective Mach number. The decrease in curvedness is mainly localized on the hairpin legs rather than on the head of the structure. Highly stretched hairpin detections are typically characterized by a medium curvedness compared to other detections of the same convective Mach number. Similar geometrical signatures are obtained for hairpins detected at different stages of the mixing layer evolution (pre-/post-/ self-similar).

4.4 Temporal distribution and formation of hairpin-like vortices

The temporal distribution of hairpin-like structure detections during the mixing layer evolution is presented in fig. 37. If an individual structure is detected to be of hairpin-like shape in multiple frames within the its lifetime, each detection contributes to the distribution. Throughout their lifetime Q-structures can develop and lose hairpin-like shape multiple times with or without interacting with other structures. Therefore the lifetime of a structure temporarily in hairpin-like shape can be split into sequences of detections in consecutive frames of the simulation. The sequences of consecutive detections vary in temporal length, however, the majority is found to be rather short-lived ($\Delta\tau < 20$, or even shorter).

For all considered convective Mach numbers, the number of hairpin detections peaks in the pre-self-similar stage and decays afterwards. This concentrated occurrence is related to the breakup process of the large, connected structures, see fig. 38 and fig. 32, which were formed through (sub-)merge events in the very early stage of the mixing layer development. Consequently, split and compound event, i.e., sub-split events, contribute the most to the peak occurrence of individual, disconnected hairpins. Examples of this structural breakup process are rendered in fig. 39 for the $M_c = 0.7$ mixing layer. The breakup process is observed for connected structures within which the hairpin heads are located in the same free stream side as well as in opposite sides. The breakup of large, connected hairpins is influenced by the choice of the iso-value used for extracting the Q-structures, i.e., a structure which is observed to breakup for the used iso-value of the frame, may stay connected for a lower iso-value.

The $M_c = 0.3$ case exhibits the most restrictive requirement for the choice of n in $Q_{\text{iso}} = \langle Q \rangle + n\sqrt{\langle Q^2 \rangle - \langle Q \rangle^2}$ to prevent the formation of very large connected structures in the early mixing layer development. While a choice of $n = 6$ indeed prevents the formation of domain-spanning structures, a significant portion of hairpin-like structure may still be connected for this choice of n and is therefore not detected as individual hairpin-like structures, which decreases the count of detections in fig. 39(a). The number of connected hairpins (not accounted for in this analysis) need to be kept in mind when evaluating the peak count of detections for the different convective Mach numbers. For the given choice of $n = 6$ the normalized peak count decreases with increasing convective Mach number from $M_c = 0.7$ to $M_c = 1.1$. With increasing convective Mach number the occurrence of the peak in the temporal distribution of the hairpin-like detections is delayed in time, but occurs approximately at the same momentum thickness Reynolds number of $Re_\theta \approx 400$. In the self-similar regimes of the mixing layers, which are less prone to the formation of largely connected structures compared to the early stage of the mixing layer development, the normalized number of detections may slightly decrease with increasing convective Mach number. The reduced detection of hairpin-like structures for increasing momentum thickness Reynolds number Re_θ supports observations of hairpins in turbulent boundary layers for which the hairpin regeneration process was reported to be not sustained once the turbulent background is developed [76]. The same authors find no evidence of hairpin vortices reaching into the wall region for $Re_\theta > 400$, which matches with the momentum thickness Reynolds number of the peaks in the temporal distribution of the hairpin-like

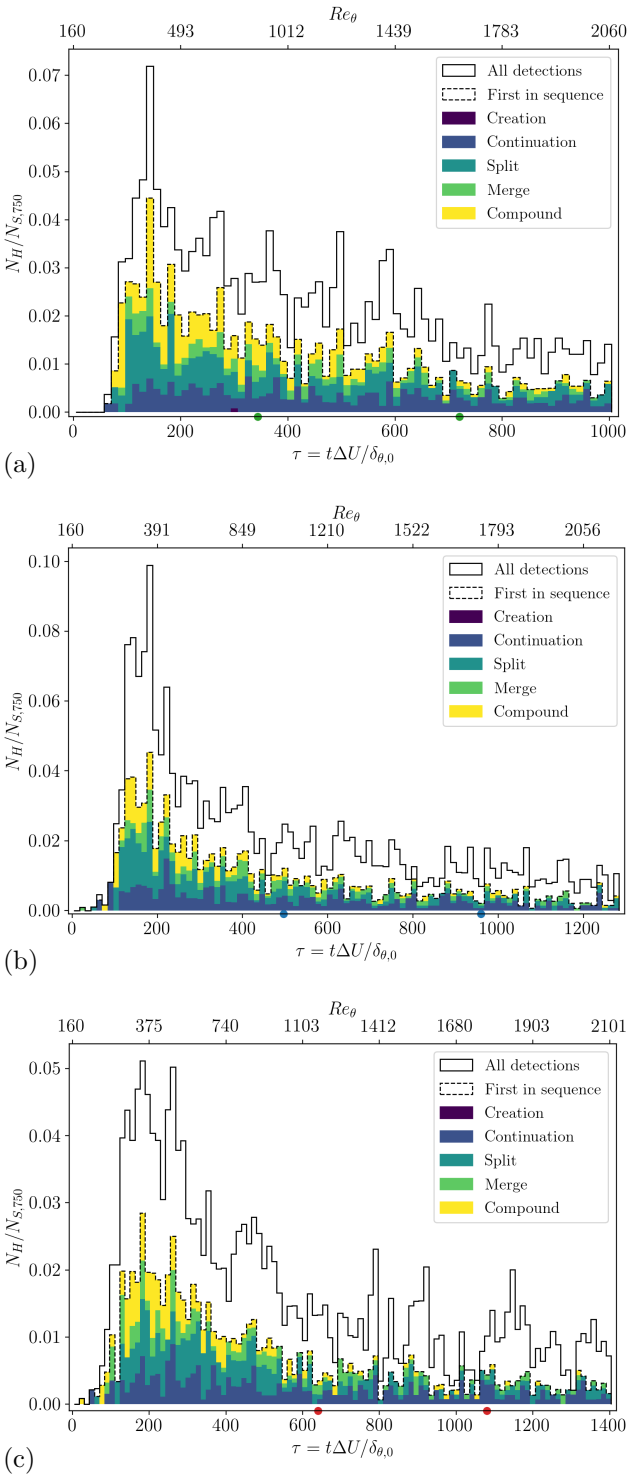

Figure 37: Temporal distribution of hairpin detections in mixing layers of convective Mach number $M_c = 0.3$ (top),$M_c = 0.7$ (center) and $M_c = 1.1$ (bottom). Number of detections normalized by the total number of extracted structures with at least 750 surface points of the time step. While the solid distributions include all detections, the dashed distributions are based on the first in sequence detections. Markers on the temporal axis show self-similar periods. The event types forming the hairpin-like structures are included as stacked contributions to the first in sequence distribution.

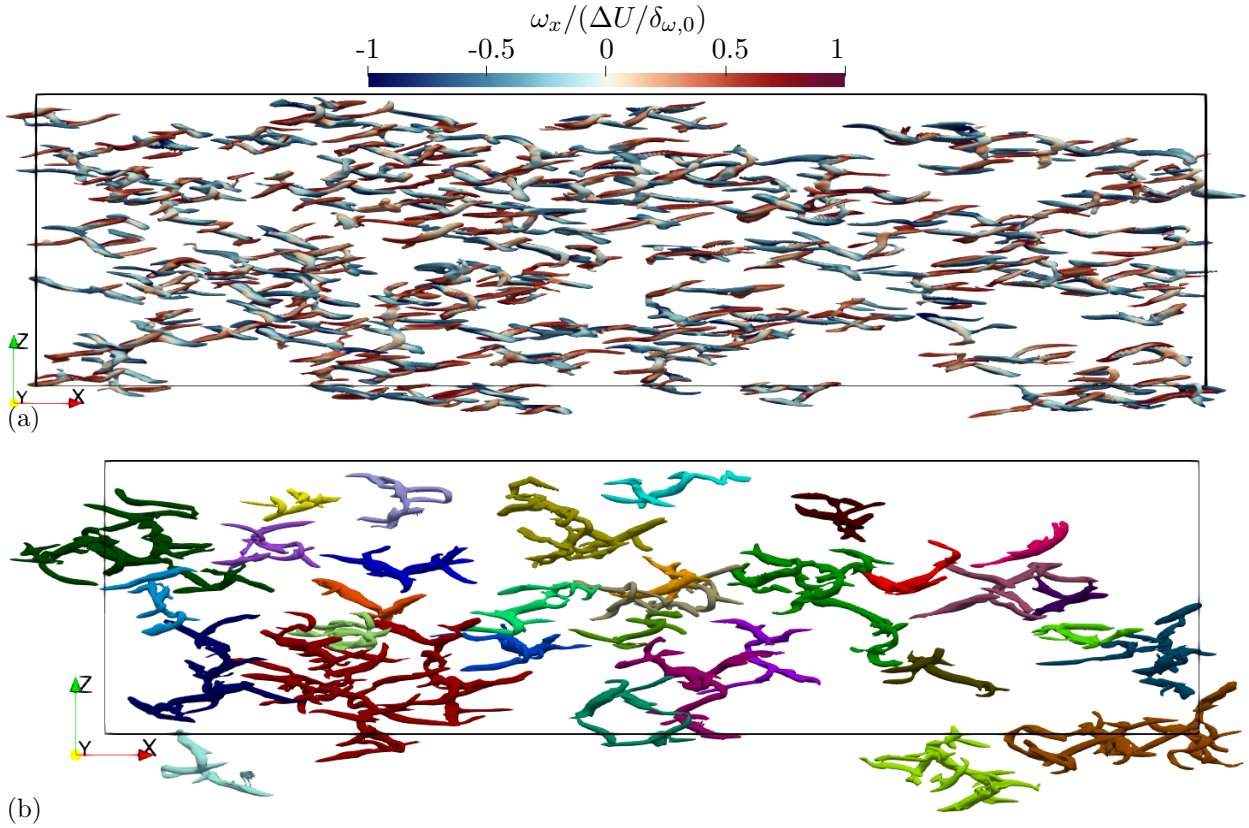

Figure 38: Selection of largely connected vortical structures extracted at $\tau = 40$ (a) and $\tau = 80$ (b) from the $M_c = 0.3$ mixing layer configuration colored by streamwise vorticity and individual structure color, respectively. Periodic reconnection of domain boundary intersecting structures is applied in streamwise and spanwise direction. The highly stretched structures span across the center plane of the mixing layer. The shape of the vortices is reminiscent of Λ-vortices observed near the inlet of spatially developing mixing layers [38].

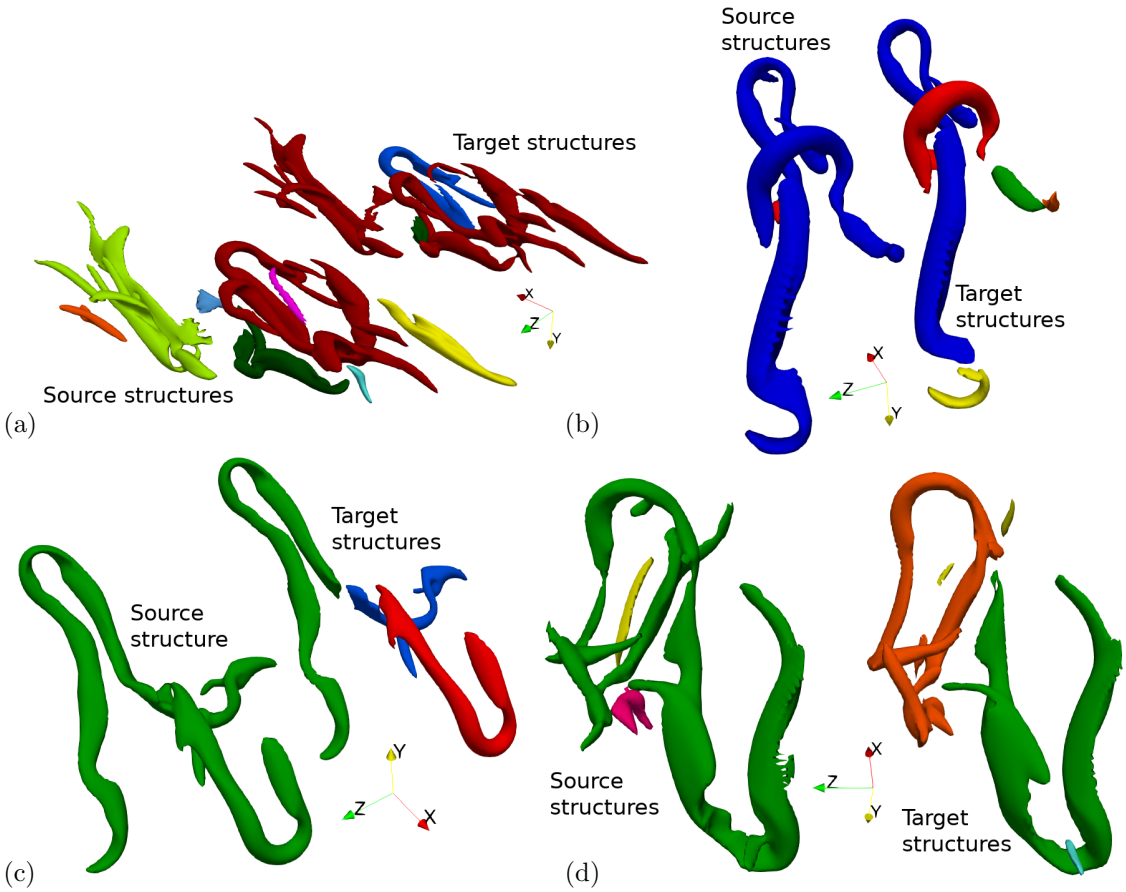

Figure 39: Connected, partially hairpin-like structures, see also fig. 38b and fig. 32, breaking into individual hairpins during the pre-self-similar stage of the $M_c = 0.7$ mixing layer. The breakup process is observed for connected structures within which the hairpin heads are located in the same free stream side (b,$\tau = 164$), opposite sides (c,$\tau = 172$) and (d,$\tau = 192$) as well as often in mixed cases (a,$\tau = 104$). Target structures artificially displaced for visibility, renderings are not to scale.

detections in fig. 37. In the subsequent stages of the mixing layer evolution the detected, individual hairpin-like structures contribute less than 5% to the total number of structures with more than 750 surface points of the frame and are therefore not considered as a dominant flow feature. However, a number of hairpins connected to other (not necessarily hairpin-like) structures may still exist, but is not accounted for.

Fig. 40 demonstrates how hook-like structures with quite unevenly pronounced legs can develop arch- or hairpin-like shape by either splitting the dominated leg or merging with another tube-like structure which serves as the second leg of the hairpin. Note, however, that hook-like structures can also develop more hairpin-like shape in a sequence of continuation events without structure interactions by gradually growing or losing a leg.

The formation of a hairpin vortex in a series of merge events is shown in fig. 41. First, the merging of two tube-like structures generates a hook which develops a bent shape and eventually merges with another structure to form a hairpin. Note, that both, the hook and the more tube-like structure, grow towards each other in this merging process. Interestingly, the hairpin has a tilted orientation with respect to the center plane of the mixing layer. The resulting hairpin is short-lived as it loses its first leg only one frame after its formation.

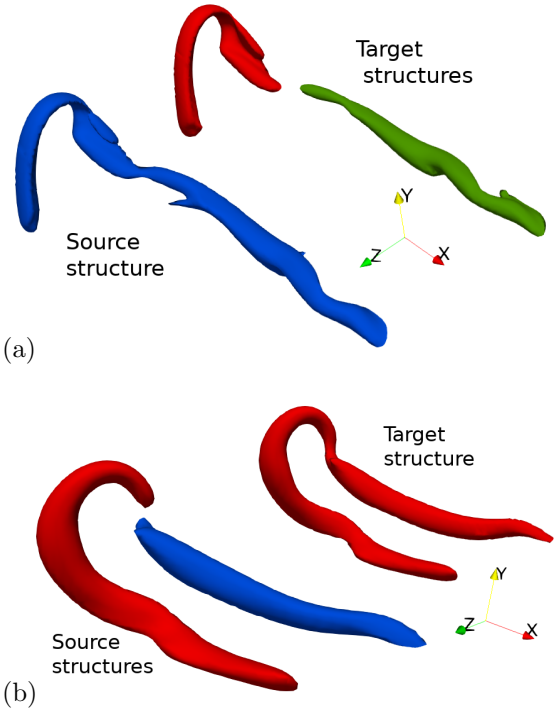

Figure 40: Hook-like structures developing in arch-like and hairpin-like shape by splitting the dominant leg (a) ($\tau = 156$) and merging with a tube-like vortex (b) ($\tau = 252$) in the $M_c = 0.7$ mixing layer, not to scale.

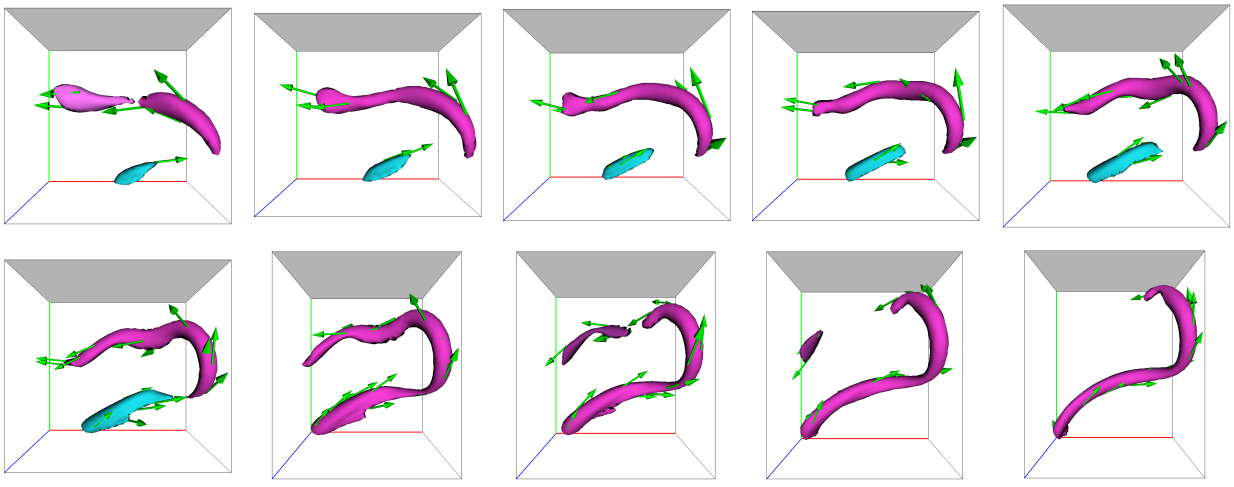

Figure 41: Side view (xy) of a series of merge events generating a short-lived hairpin vortex in the $M_c = 0.3$ mixing layer and subsequent breakup from $\tau = 304$ (top,left) to $\tau = 340$ (bottom,right). Structure color represents structure ID, while green arrows are the down sampled vorticity on the structures. Note the tilted orientation of the hairpin with respect to the center plane of the layer indicated in gray.

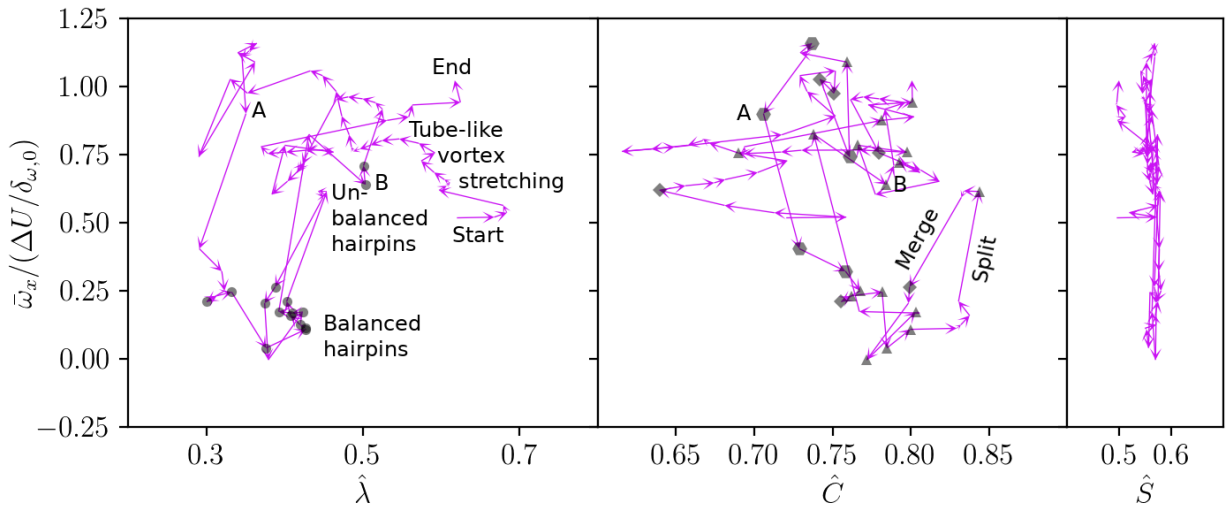

Figure 42: Trajectory of a vortical structure temporarily developing hairpin-like shape in geometrical feature space enhanced with surface-averaged streamwise vorticity component. The trajectory section between points A and B corresponds to the renderings in fig. 43. Detected haipin-like structures are highlighted as ● in the left subplot. In the center subplot markers ▲, ◆and ⬢ indicate if a step of the trajectory is the target of a split, merge or compound event respectively.

Fig. 42 presents the full trajectory of a structure which preserves its hairpin shape for a longer sequence of frames in the geometrical feature space enhanced with the surface-averaged streamwise vorticity component. The temporal evolution of the structure is rendered for a subsection of its trajectory in the corresponding fig. 43. The structure originates from a creation event at $\tau = 80$ and develops tube-like shape, while being orientated mainly in streamwise direction and intersecting with the center plane of the mixing layer. As the tube-like structure becomes more stretched, its streamwise vorticity component intensifies. The structure develops hook-like shape as a result of a complex compound event and eventually becomes hairpin-like over a series of frames within which one leg intensifies while the other leg is shortened in splits. At the time the structure is first detected as a hairpin the streamwise vorticity component is almost balanced on the structure. The geometric signature of the hairpin detections is in agreement with those presented in fig. 36a. The sequence of consecutive hairpin detection ends in a split of a leg, which leads to an imbalance in the surface-averaged streamwise vorticity. However, the structure retrieves its hairpin shape in a merge with another structure serving as the new leg.

4.5 Cross-stream and spanwise growth of hairpin vortices

The entire lifespan of two structures which temporarily develop hairpin-like shape in the $M_c = 0.3$ mixing layer are shown in fig. 44 and fig. 47. Both structures remain close to the center plane of the mixing layer throughout their lifetime, often intersecting with it. Therefore, the streamwise component of the surface-averaged velocity changes its sign multiple times during the structure evolution. Resulting from a split, the structure shown in fig. 47 has a hairpin-like shape with the head located in the upper free stream. However, multiple structure interactions later, the structure has developed into a larger hairpin with the head located in the lower free stream.

The distribution of the cross-stream location of all detected hairpin-like structures and the first-in-sequence subset is presented in fig. 45 for the three considered convective Mach numbers. Here,

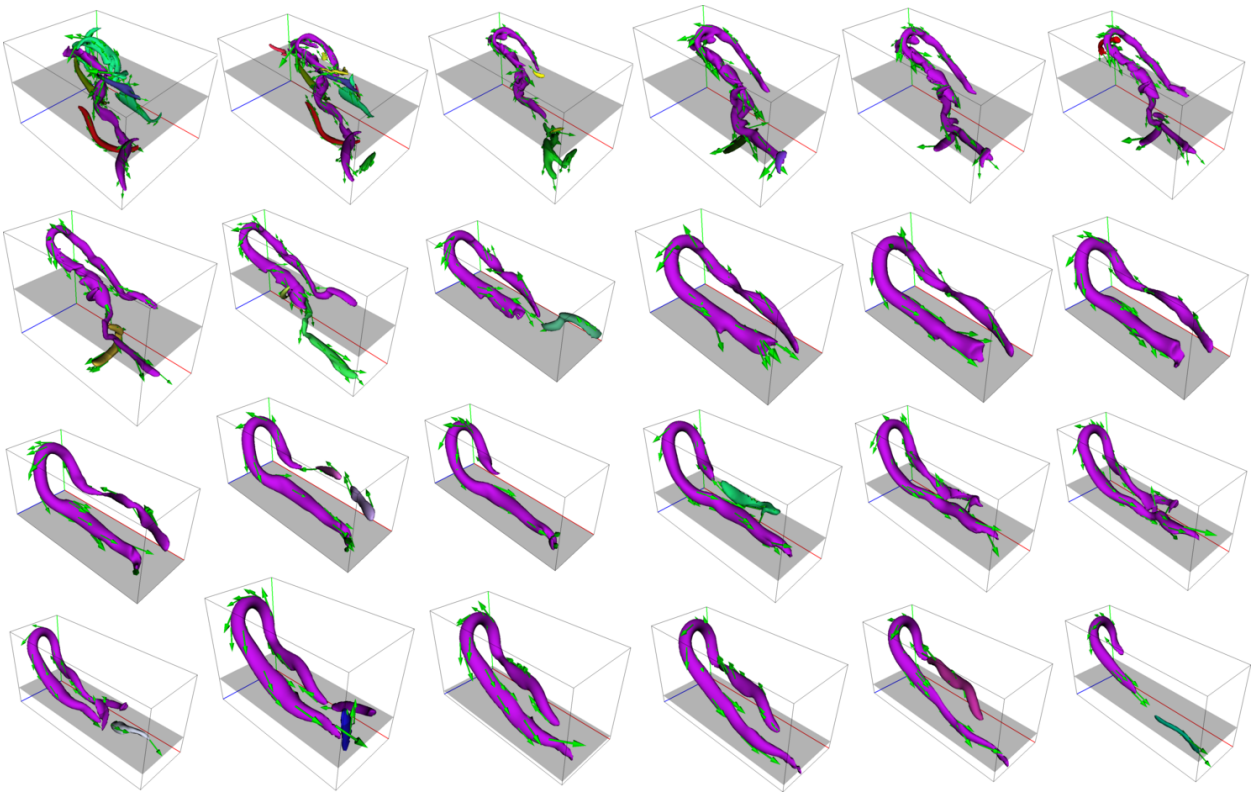

Figure 43: Section (τ = 204 - 296) of a lifespan of a vortical structure developing hairpin-like shape in the $M_c = 0.3$ mixing layer, from left to right and top to bottom. Interacting structures included as source or target structures of the respective event. The structure is mostly located above the center plane of the mixing layer indicated in translucent black. Several structure interactions contribute to the persistence of the hairpin in the rendered section and subsequent frames (not shown).

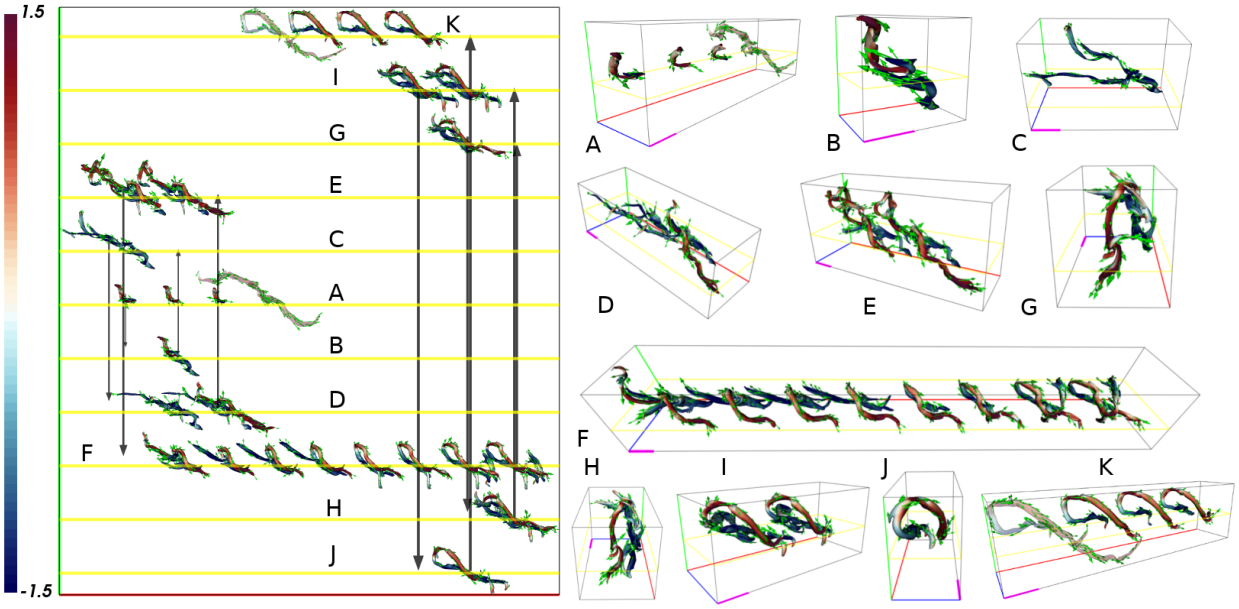

Figure 44: Lifetime ($\tau = 280$ - 376) of a structure temporarily developing hairpin-like shape in the $M_c = 0.3$ mixing layer. Streamwise vorticity mapped on the structure and vorticity sampled as green arrows. Due to the proximity to the center plane of the mixing layer, the surface-averaged streamwise velocity of the surface often changes its sign. Artificial structure displacement added for visibility based on the sign of this surface-averaged velocity: Starting from level A a transition upwards indicates a change towards an (on average) left moving structure, while a downwards transition indicates a shift toward a right moving structure. Size of the black arrow indicates the temporal order of these transitions. The yellow plane indicates the center plane of the mixing layer at each level of the figure. The 3D renderings on the right show the structures of each level of the left side of the figure (parallel projection). While the rendering are not to scale, the pink line serves as a reference scale (10 times the initial momentum layer thickness). The structures from which the hairpin-like structure originally split (source of (sub-)split) and eventually merges (target of (sub-)merge) are added with reduced opacity. Note that the head of the hairpin becomes quite tilted at the end of the lifetime.

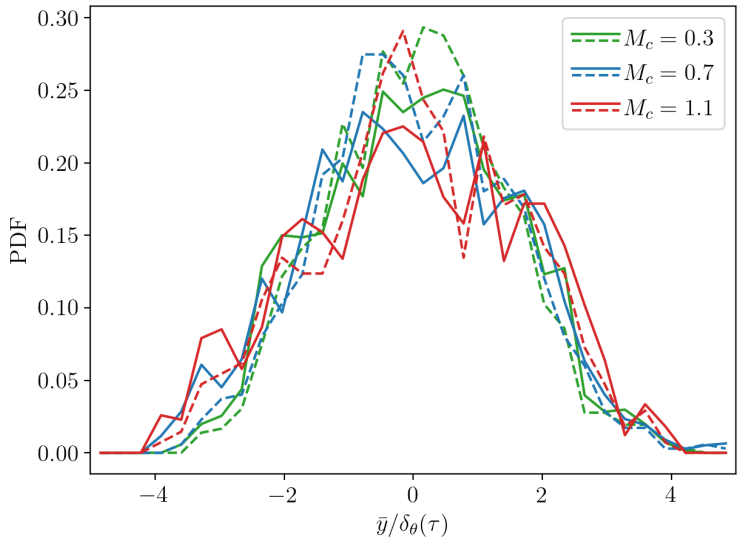

Figure 45: Distribution of the cross-stream location of all detected hairpins (solid) and the first-in-sequence subset of hairpins (dashed) normalized by the momentum thickness. Compare to the Reynolds stress profiles in fig. 23 and fig. 22 as well as the cross-stream distributions of newly created structures of all shapes in the self-similar regimes in fig. 28 (b).

the cross-stream location of a structure is defined as the mean of its minimal and maximal cross-stream position. Following the Reynolds stress profiles, fig. 23 and fig. 22, the distributions peak at the center plane and are about symmetrical. The distribution including only the first-in-sequence detections shows slightly less variance and more detections occur closer to the center plane.

Fig. 46 investigates the subset of the center plane crossing detected structures and their extent on each free stream side of the mixing layer relative to the momentum layer thickness at the time. The majority of the structures shows an uneven top and bottom cross stream extent, which is also supported by the previous renderings of detected structures. For hairpins whose legs are oriented in the streamwise direction and the head in spanwise direction, the dominant cross-stream side is the side on which the head is located. Fig. 46 includes structures which have a tilted orientation with respect to the center plane of the mixing layer.

In turbulent boundary layers the cross-stream and spanwise growth rate are reported to be similar to each other and is associated with Townsend's attached eddy hypothesis [73]. Therefore, the hairpin growth behavior is investigated in the context of the mixing layer configuration, in fig. 48. The minimal and maximal surface point coordinate in the cross-stream and spanwise direction is used to define the extent of a hairpin structure in the particular direction, Δy and Δz. The evolution of each structure temporarily in hairpin shape is inspected visually to exclude structures that show a significant tilted orientation and hairpins that are distorted by connecting to other structures at any point in their evolution. While no exact measure is used to exclude those structures, it is ensured that the spanwise extent is representative for distance of the outsides of the legs and the cross-stream extent is an indication of the distance between the head and the legs. Due to these requirements mainly hairpins occurring in the pre-self-similar regime are included in the analysis. While the growth behavior differs between individual hairpins, the overall trend for the $M_c = 0.3$ case is in rough agreement with the findings reported for hairpins in wall-bounded turbulence. The cross-stream and spanwise structure extents are similar to each other. The results are less clear for the $M_c = 1.1$ mixing layer as a number of hairpins is found to grow in cross-stream

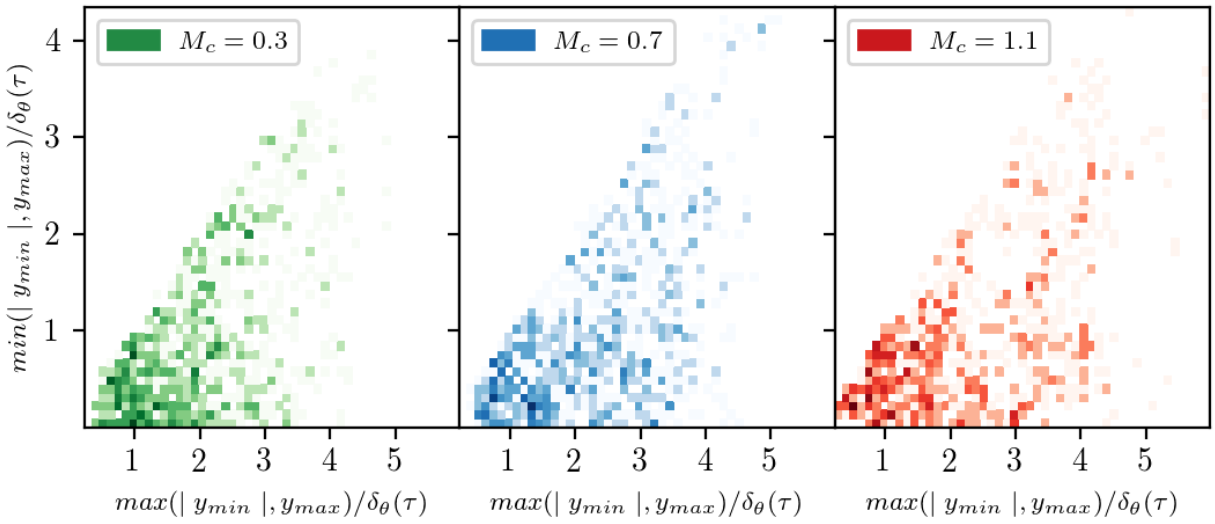

Figure 46: The cross-stream extent of center plane crossing hairpins. Most hairpin-like structures emerge unevenly into the top and bottom free stream. On the basis of prior renderings, the dominant cross-stream side is the side where the head is located.

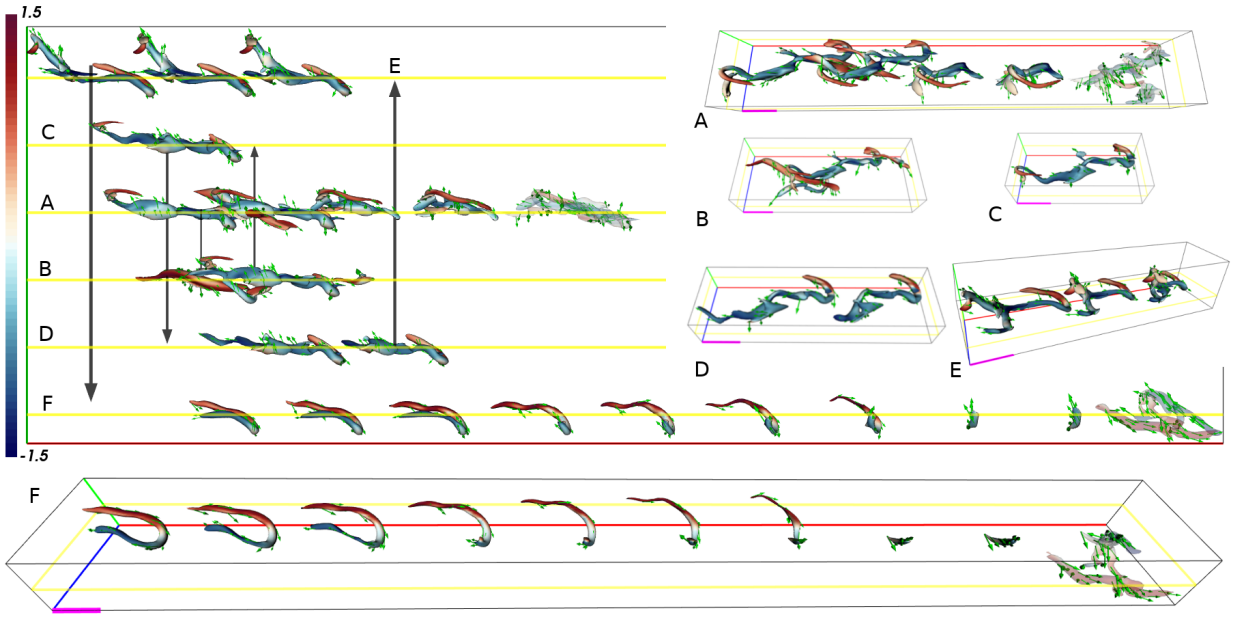

Figure 47: Lifetime (τ = 96 - 172) of a structure developing temporarily hairpin-like shape while crossing the center plane of the mixing layer. As frequently observed, the hairpin loses one leg over time and becomes a hook-like structure. Other plot elements as in fig. 44.

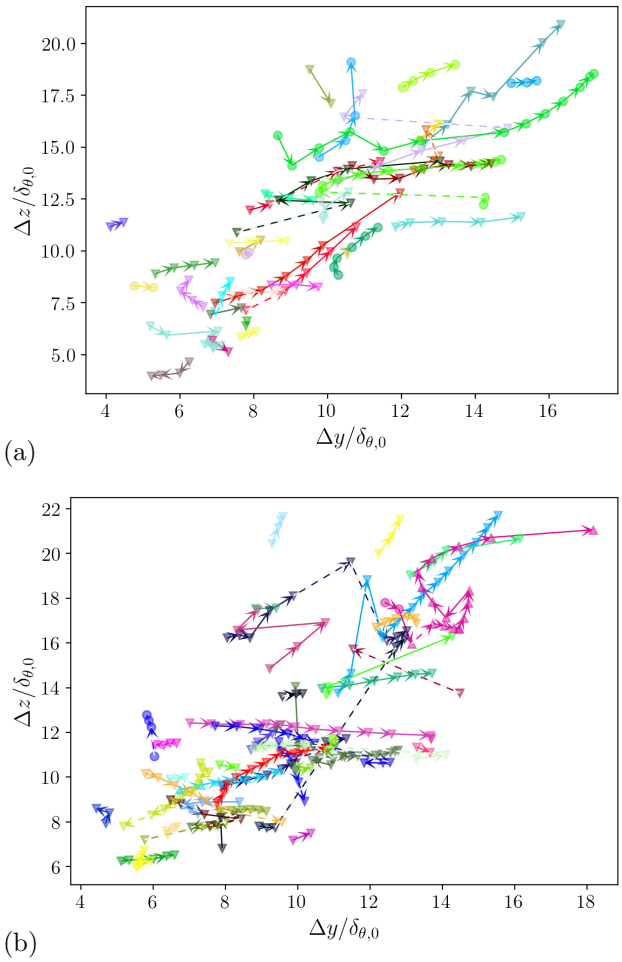

Figure 48: Growth of the cross-stream Δy and spanwise Δz extent of selected hairpin-like vortices in the $M_c = 0.3$ (a) and $M_c = 1.1$ (b) mixing layers. Colors indicate individual tracking structure ID, while temporal order is shown with arrows. For hairpin detections in non-consecutive frames dashed arrows are used. Note that the hairpins may be affected by structure interactions at any time, which influence the extent of the structure. Hairpin detection in the pre-self-similar self-similar and post-self-similar stage plotted as ▼, ● and ▲, respectively.

direction while approximately preserving their spanwise extent. However, the overall ranges of cross-stream and spanwise extents are similar for both convective Mach numbers.

References

[1] Guangfeng Ji and Han-Wei Shen. Feature tracking using earth mover's distance and global optimization. In *Pacific graphics*, volume 2, 2006.

[2] Jesus Caban, Alark Joshi, and Penny Rheingans. Texture-based feature tracking for effective time-varying data visualization. *IEEE Trans Vis Comput Graph*, 13(6):1472–1479, 2007.

[3] Maxime Soler, Mélanie Plainchault, Bruno Conche, and Julien Tierny. Lifted wasserstein matcher for fast and robust topology tracking. *arXiv preprint arXiv:1808.05870*, 2018.

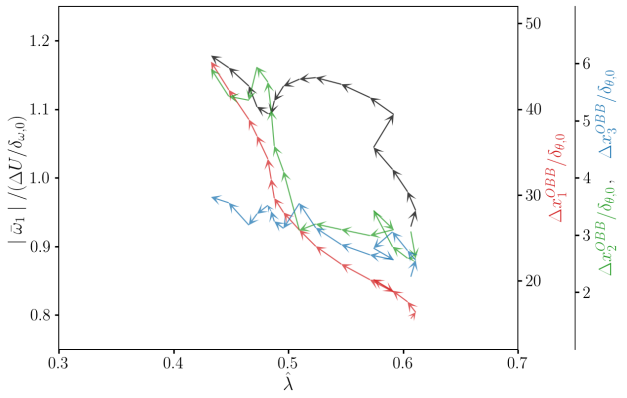

Figure 49: Decrease of the compactness parameter $\hat{\lambda}$ during stretching of a straight tube-like Q-structure, rendered in fig. 50. The temporal evolution of the size of the major, medium and minor direction of the structure's OBB is shown in red, green and blue, respectively. The amplification of the vorticity component in the stretching direction is quantified by means of the surface-averaged component of the vorticity in direction of the OBB major direction $\bar{\omega}_1$ (black trajectory).

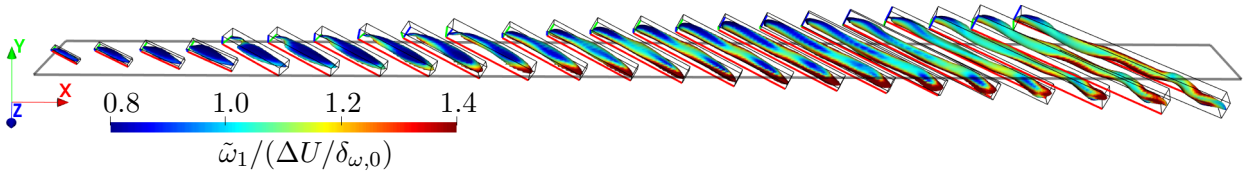

Figure 50: Stretching of a straight tube-like Q-structure from $\tau = 80$ to $\tau = 168$ in the $M_c = 0.3$ mixing layer (left to right). Artificial displacement in streamwise direction is applied to the structure for visibility. Major, medium and minor direction of the OBB of the structure at each step are indicated in red, green and blue, respectively. The vorticity component in the direction of the major OBB direction $\tilde{\omega}_1$ is mapped on the surface. The mixing layer center plane is represented in yellow. The structure stretching and vorticity component intensification is quantified in fig. 49.

[4] Deborah Silver and Xin Wang. Volume tracking. In *Proceedings of Seventh Annual IEEE Visualization'96*, pages 157–164. IEEE, 1996.

[5] Deborah Silver and Xin Wang. Tracking and visualizing turbulent 3d features. *IEEE Trans Vis Comput Graph*, 3(2):129–141, 1997.

[6] Deborah Silver and Xin Wang. Tracking scalar features in unstructured data sets. In *Proceedings Visualization'98 (Cat. No. 98CB36276)*, pages 79–86. IEEE, 1998.

[7] Jian Chen, Deborah Silver, and Lian Jiang. The feature tree: Visualizing feature tracking in distributed amr datasets. In *IEEE Symposium on Parallel and Large-Data Visualization and Graphics, 2003. PVG 2003.*, pages 103–110. IEEE, 2003.

[8] Ravi Samtaney, Deborah Silver, Norman Zabusky, and Jim Cao. Visualizing features and tracking their evolution. *Computer*, 27(7):20–27, 1994.

[9] Freek Reinders, Frits H Post, and Hans JW Spoelder. Attribute-based feature tracking. In *Data visualization'99*, pages 63–72. Springer, 1999.

[10] Koob FJ Reinders, Koob Frederik, and Jan Reinders. Feature-based visualization of time-dependent data. 2001.

[11] John Clyne, Pablo Mininni, and Alan Norton. Physically-based feature tracking for cfd data. *IEEE Trans Vis Comput Graph*, 19(6):1020–1033, 2012.

[12] Hanqi Guo, Carolyn L Phillips, Tom Peterka, Dmitry Karpeyev, and Andreas Glatz. Extracting, tracking, and visualizing magnetic flux vortices in 3d complex-valued superconductor simulation data. *IEEE Trans Vis Comput Graph*, 22(1):827–836, 2015.

[13] Ivan Bermejo-Moreno and DI Pullin. On the non-local geometry of turbulence. *J. Fluid Mech.*, 603:101–135, 2008.

[14] Jan J Koenderink and Andrea J Van Doorn. Surface shape and curvature scales. *Image Vis Comput*, 10(8):557–564, 1992.

[15] Jon Louis Bentley. Multidimensional binary search trees used for associative searching. *Commun. ACM*, 18(9):509–517, 1975.

[16] Jerome H Friedman, Jon Louis Bentley, and Raphael Ari Finkel. An algorithm for finding best matches in logarithmic expected time. *ACM Trans Math Softw (TOMS)*, 3(3):209–226, 1977.

[17] Elmer G Gilbert, Daniel W Johnson, and S Sathiya Keerthi. A fast procedure for computing the distance between complex objects in three-dimensional space. *IEEE Robot Autom Mag*, 4(2):193–203, 1988.

[18] Mattia Montanari, Nik Petrinic, and Ettore Barbieri. Improving the gjk algorithm for faster and more reliable distance queries between convex objects. *ACM Trans. Graph. (TOG)*, 36(3):1–17, 2017.

[19] Stefan Gottschalk, Ming C Lin, and Dinesh Manocha. Obbtree: A hierarchical structure for rapid interference detection. In *Proceedings of the 23rd annual conference on Computer graphics and interactive techniques*, pages 171–180, 1996.

[20] Jose Luis Blanco and Pranjal Kumar Rai. nanoflann: a C++ header-only fork of FLANN, a library for nearest neighbor (NN) with kd-trees. https://github.com/jlblancoc/nanoflann, 2014.

[21] Adrián Lozano-Durán and Javier Jiménez. Time-resolved evolution of coherent structures in turbulent channels: characterization of eddies and cascades. *J. Fluid Mech.*, 759:432–471, 2014.

[22] Xiangyu Gao, Ivan Bermejo-Moreno, and Johan Larsson. Parametric numerical study of passive scalar mixing in shock turbulence interaction. *J. Fluid Mech.*, 895, 2020.

[23] N Etemadi. On curve and surface stretching in isotropic turbulent flow. *J. Fluid Mech.*, 221:685–692, 1990.

[24] SS Girimaji and SB Pope. Material-element deformation in isotropic turbulence. *J. Fluid Mech.*, 220:427–458, 1990.

[25] SS Girimaji and SB Pope. Propagating surfaces in isotropic turbulence. *J. Fluid Mech.*, 234:247–277, 1992.

[26] Susumu Goto and Shigeo Kida. Reynolds-number dependence of line and surface stretching in turbulence: folding effects. *J. Fluid Mech.*, 586:59, 2007.

[27] Yue Yang, DI Pullin, and Ivan Bermejo-Moreno. Multi-scale geometric analysis of lagrangian structures in isotropic turbulence. *J. Fluid Mech.*, 654:233–270, 2010.

[28] Dimitri Papamoschou and Sanjiva K Lele. Vortex-induced disturbance field in a compressible shear layer. *Phys Fluid Fluid Dynam*, 5(6):1412–1419, 1993.

[29] C Cambon, GN Coleman, and NN Mansour. Rapid distortion analysis and direct simulation of compressible homogeneous turbulence at finite mach number. 1992.

[30] R Friedrich and FP Bertolotti. Compressibility effects due to turbulent fluctuations. *Applied scientific research*, 57(3-4):165–194, 1996.

[31] Garry L Brown and Anatol Roshko. On density effects and large structure in turbulent mixing layers. *J. Fluid Mech.*, 64(4):775–816, 1974.

[32] NT Clemens and MG Mungal. Large-scale structure and entrainment in the supersonic mixing layer. *J. Fluid Mech.*, 284:171–216, 1995.

[33] PS Karasso and MG Mungal. Scalar mixing and reaction in plane liquid shear layers. *J. Fluid Mech.*, 323:23–63, 1996.

[34] Robert D Moser and Michael M Rogers. The three-dimensional evolution of a plane mixing layer: pairing and transition to turbulence. *J. Fluid Mech.*, 247:275–320, 1993.

[35] Michael M Rogers and Robert D Moser. Direct simulation of a self-similar turbulent mixing layer. *Phys. Fluids*, 6(2):903–923, 1994.

[36] RD Moser and MM Rogers. Mixing transition and the cascade to small scales in a plane mixing layer. *Phys Fluid Fluid Dynam*, 3(5):1128–1134, 1991.

[37] Michael M Rogers and Robert D Moser. The three-dimensional evolution of a plane mixing layer: the kelvin–helmholtz rollup. *J. Fluid Mech.*, 243:183–226, 1992.

[38] Qiang Zhou, Feng He, and MY Shen. Direct numerical simulation of a spatially developing compressible plane mixing layer: flow structures and mean flow properties. *J. Fluid Mech.*, 711:437, 2012.

[39] Antonio Attili and Fabrizio Bisetti. Statistics and scaling of turbulence in a spatially developing mixing layer at reλ= 250. *Phys. Fluids*, 24(3):035109, 2012.

[40] C Pantano and S Sarkar. A study of compressibility effects in the high-speed turbulent shear layer using direct simulation. *J. Fluid Mech.*, 451:329, 2002.

[41] H Foysi and S Sarkar. The compressible mixing layer: an les study. *Theor Comput Fluid Dyn*, 24(6):565–588, 2010.

[42] J Raymond Ristorcelli and Gregory A Blaisdell. Consistent initial conditions for the dns of compressible turbulence. *Phys. Fluids*, 9(1):4–6, 1997.

[43] Qibing Li and Song Fu. Numerical simulation of high-speed planar mixing layer. *Comput. Fluids*, 32(10):1357–1377, 2003.

[44] AAR Townsend. *The structure of turbulent shear flow*. Cambridge university press, 1980.

[45] RD Mehta. Effect of velocity ratio on plane mixing layer development: Influence of the splitter plate wake. *Exp. Fluids.*, 10(4):194–204, 1991.

[46] James H Bell and Rabindra D Mehta. Development of a two-stream mixing layer from tripped and untripped boundary layers. *AIAA J.*, 28(12):2034–2042, 1990.

[47] Stanley F Birch and JamesM Eggers. A critical reviewof the experimental data for developedfree turbulent shear layers. *Free Turbulent Shear Flows, VolumeI-ConferenceProceedings, NASASP-321*, pages 11–40, 1972.

[48] S Barre, D Alem, and JP Bonnet. Experimental study of a normal shock/homogeneous turbulence interaction. *AIAA J.*, 34(5):968–974, 1996.

[49] Jonathan B Freund, Sanjiva K Lele, and Parviz Moin. Compressibility effects in a turbulent annular mixing layer. part 1. turbulence and growth rate. *J. Fluid Mech.*, 421:229–267, 2000.

[50] J Bonnet, J Debisschop, and O Chambres. Experimental studies of the turbulent structure of supersonic mixinglayers. In *31st Aerospace Sciences Meeting*, page 217, 1993.

[51] Song Fu and Qibing Li. Numerical simulation of compressible mixing layers. *Int. J. Heat Fluid Flow*, 27(5):895–901, 2006.

[52] J.C.R. Hunt, A. Wray, and P. Moin. Eddies, stream, and convergence zones in turbulent flows. *Proceedings of the Summer Program (Center for Turbulence Research)*, pages 193–208, 1988.

[53] Uve Dallmann. Topological structures of three-dimensional vortex flow separation. In *16th Fluid and Plasmadynamics Conference*, page 1735, 1983.

[54] H Vollmers, HP Kreplin, and HU Meier. Separation and vortical-type flow around a prolate spheroid-evaluation of relevant parameters. Technical report, DEUTSCHE FORSCHUNGS-UND VERSUCHSANSTALT FUER LUFT-UND RAUMFAHRT EV ..., 1983.

[55] Min S Chong, Anthony E Perry, and Brian J Cantwell. A general classification of three-dimensional flow fields. *Phys Fluid Fluid Dynam*, 2(5):765–777, 1990.

[56] Jinhee Jeong and Fazle Hussain. On the identification of a vortex. *J. Fluid Mech.*, 285(-1):69, feb 1995.

[57] CH Berdahl and DS Thompson. Eduction of swirling structure using the velocity gradient tensor. *AIAA J.*, 31(1):97–103, 1993.

[58] Jigen Zhou, Ronald J Adrian, S Balachandar, and TM Kendall. Mechanisms for generating coherent packets of hairpin vortices in channel flow. *J. Fluid Mech.*, 387:353–396, 1999.

[59] Brenden Epps. Review of vortex identification methods. In *55th AIAA aerospace sciences meeting*, page 0989, 2017.

[60] Yuning Zhang, Kaihua Liu, Haizhen Xian, and Xiaoze Du. A review of methods for vortex identification in hydroturbines. *Renew. Sust. Energ. Rev.*, 81:1269–1285, 2018.

[61] Sawan Suman and Sharath S Girimaji. Velocity gradient invariants and local flow-field topology in compressible turbulence. *J. Turbul.*, (11):N2, 2010.

[62] Jonas Buchmeier, Alexander Bußmann, Xiangyu Gao, and Iván Bermejo-Moreno. Geometry and dynamics of passive scalar structures in compressible turbulent mixing. *Physics of Fluids*, 33(10):105126, 2021.

[63] Theodore Theodorsen. Mechanisms of turbulence. In *Proceedings of the 2ˆ¡ nd¿ Midwestern Conference on Fluid Mechanics, 1952*, 1952.

[64] Theodore Theodorsen. The structure of turbulence. In *50 Jahre Grenzschichtforschung*, pages 55–62. Springer, 1955.

[65] Stephen K Robinson. Coherent motions in the turbulent boundary layer. *Annu. Rev. Fluid Mech.*, 23(1):601–639, 1991.

[66] Michael M Rogers and Parviz Moin. The structure of the vorticity field in homogeneous turbulent flows. *J. Fluid Mech*, 176:33–66, 1987.

[67] Christina Vanderwel and Stavros Tavoularis. Coherent structures in uniformly sheared turbulent flow. *J. Fluid Mech.*, 689:434–464, 2011.

[68] Siwei Dong, Adrián Lozano-Durán, Atsushi Sekimoto, and Javier Jiménez. Coherent structures in statistically stationary homogeneous shear turbulence. *J. Fluid Mech.*, 816:167–208, 2017.

[69] Dongdong Zhang, Jianguo Tan, and Xiao Yao. Direct numerical simulation of spatially developing highly compressible mixing layer: Structural evolution and turbulent statistics. *Phys. Fluids*, 31(3):036102, 2019.

[70] M S Acarlar and C R Smith. A study of hairpin vortices in a laminar boundary layer. Part 1. hairpin vortices generated by a hemisphere protuberance. *J. Fluid Mech.*, 175:1–41, 1987.

[71] Juan M Chacín, Brian J Cantwell, and Stephen J Kline. Study of turbulent boundary layer structure using the invariants of the velocity gradient tensor. *Exp. Therm. Fluid Sci.*, 13(4):308–317, 1996.

[72] Christopher D Tomkins and Ronald J Adrian. Spanwise structure and scale growth in turbulent boundary layers. *J. Fluid Mech.*, 490:37–74, 2003.

[73] Ronald J Adrian. Hairpin vortex organization in wall turbulence. *Phys. Fluids*, 19(4):041301, 2007.

[74] Xiaohua Wu and Parviz Moin. Direct numerical simulation of turbulence in a nominally zero-pressure-gradient flat-plate boundary layer. *J. Fluid Mech.*, 630:5–41, 2009.

[75] Philipp Schlatter, Q Li, Ramis Örlü, Fazle Hussain, and Dan S Henningson. On the near-wall vortical structures at moderate Reynolds numbers. *Eur. J. Mech.-B/Fluids*, 48:75–93, 2014.

[76] Georg Eitel-Amor, Ramis Örlü, Philipp Schlatter, and O Flores. Hairpin vortices in turbulent boundary layers. *Phys. Fluids*, 27(2):025108, 2015.

[77] Ronald J Adrian, Carl D Meinhart, and Christopher D Tomkins. Vortex organization in the outer region of the turbulent boundary layer. *J. Fluid Mech.*, 422:1–54, 2000.

[78] Samuel Maurus and Claudia Plant. Skinny-dip: clustering in a sea of noise. In *Proceedings of the 22nd ACM SIGKDD international conference on Knowledge discovery and data mining*, pages 1055–1064, 2016.

[79] Martin Ester, Hans-Peter Kriegel, Jörg Sander, Xiaowei Xu, et al. A density-based algorithm for discovering clusters in large spatial databases with noise. In *kdd*, volume 96, pages 226–231, 1996.

[80] Erich Schubert, Jörg Sander, Martin Ester, Hans Peter Kriegel, and Xiaowei Xu. Dbscan revisited, revisited: why and how you should (still) use dbscan. *ACM Trans. Database Syst. (TODS)*, 42(3):1–21, 2017.

[81] Abhishek Harikrishnan, Cedrick Ansorge, Rupert Klein, and Nikki Vercauteren. Geometry and organization of coherent structures in stably stratified atmospheric boundary layers. *arXiv preprint arXiv:2110.02253*, 2021.